

Front page

Exam information

NFYK10020E - Physics Thesis 60 ECTS, Niels Bohr
Institute - Contract:127734 (Marie Cornelius Hansen)


Handed in by

Marie Cornelius Hansen
lnr457@alumni.ku.dk

Exam administrators

Eksamensteam, tel 35 33 64 57
eksamen@science.ku.dk

Assessors

Mauricio Bustamante
Examiner
Mbustamante@nbi.ku.dk
 +4535334778

Hand-in information

Title: Searching for axion-like dark matter with IceCube high-energy astrophysical neutrinos

Title, english: Searching for axion-like dark matter with IceCube high-energy astrophysical neutrinos

The sworn statement: Yes

Does the hand-in contain confidential material: No



SEARCHING FOR AXION-LIKE DARK MATTER WITH ICECUBE HIGH-ENERGY ASTROPHYSICAL NEUTRINOS

M.Sc. PROJECT

Written by *Marie Cornelius Hansen*

September 5, 2022

Supervised by

Mauricio Bustamante

NIELS BOHR INSTITUTE

UNIVERSITY OF COPENHAGEN

An abstract geometric design in the bottom right corner, consisting of several overlapping circles and intersecting lines, creating a complex, organic shape.

Abstract

Neutrinos are elementary particles with unique properties that make them ideal probes of new physics beyond the Standard Model. The highest-energy neutrinos known, produced in astrophysical phenomena, offer us an opportunity to look for new fundamental particles at energies not reached by particle accelerators on Earth. One possible new particle is the axion, originally postulated as a solution to the strong CP problem of the Standard Model, and, also, a dark matter candidate. We investigate the potential existence of the more general axion-like dark matter indirectly via high-energy astrophysical neutrinos: as they travel billions of light-years from their sources towards the Earth, they might encounter a cosmic background of axion-like dark matter. If a neutrino-axion interaction happens in the s -channel via a heavy neutral lepton mediator, it will leave characteristic features like bumps and dips in the shape of the neutrino energy spectrum. We compute the flux of high-energy neutrinos that reaches Earth varying the axion mass, mediator mass, and axion-neutrino coupling strength over wide ranges of values. Our method allows us to look for tiny coupling strengths down to 10^{-10} , and axion masses down to 10^{-11} eV, currently not constrained in the literature. We search for the characteristic features of the axion-neutrino interaction in astrophysical high-energy neutrino events detected by the IceCube Neutrino Telescope, using the latest publicly available sample of 7.5 years of High Energy Starting Events (HESE). Our computation of event rates are based on detailed HESE Monte Carlo simulations and analysis made available by the IceCube Collaboration. We find no statistically significant evidence for the existence of axion-neutrino interactions in the HESE data. Thus, we place leading constraints on the mass of the axion-like dark matter particle, the mass of the heavy neutral lepton mediator, and the coupling strength of the axion-neutrino interaction.

Acknowledgments

This past year has truly been a great experience. I want to thank my supervisor Mauricio Bustamante for giving me an opportunity to do proper research. You have encouraged me and believed in my abilities even when I doubted them myself. Without your guidance I definitely would not be where I am now.

I am grateful to the rest of our group for many useful discussions. To Victor, Damiano, and our newest addition to the group, Bernanda, thank you for always offering your help.

To all the other people in the AstroNu group at NBIA, thank you for many enjoyable times at lunch and for all the trips to the ice cream shop. Without your warm welcome, it would have been a much more lonely time at the institute. I also want to thank my office mate Roberto for keeping me company especially these last couple of weeks.

Lastly, thank you to Martin for your endless patience and encouragement, and your contagious excitement for physics. There is no way I would have been able to do this without you.

Contents

1	Introduction	1
2	Dark matter	3
2.1	Motivation for dark matter	3
2.2	Dark matter candidates	5
2.2.1	A quick view on the Standard Model	5
2.2.2	Properties of a dark matter particle	6
2.3	Axions and axion-like particles	8
2.3.1	The strong CP problem	8
2.3.2	Axion-like dark matter	9
2.3.3	Searches and constraints	10
3	Neutrinos	13
3.1	In the Standard Model and beyond	13
3.1.1	Neutrino oscillations	13
3.1.2	Neutrino mass	14
3.1.3	Sterile neutrinos	14
3.2	Astrophysical neutrinos	16
3.2.1	High-energy astrophysical neutrino production	16
3.3	IceCube telescope and neutrino detection	18
3.3.1	Neutrino-nucleon interactions	18
3.3.2	Status in IceCube high-energy astrophysical neutrino observations . .	20
3.4	Neutrinos interacting with axion-like dark matter	21
3.4.1	Current axion-neutrino landscape	22
4	The high-energy neutrino flux at Earth	24
4.1	Derivation of the propagation equation	24
4.2	Solution of the propagation equation	25
4.3	Numerical implementation	29
4.3.1	Constraining the parameter space	31
4.3.2	Extrapolation	36

5	Detecting high-energy neutrinos	39
5.1	Propagation through the Earth	39
5.2	IceCube High Energy Starting Events and background	43
5.3	Event rates	46
5.3.1	Event rate derivation	46
5.3.2	HESE Monte Carlo simulations	46
6	Statistical analysis	49
7	Results	52
8	Conclusion and outlook	55
A	Extrapolation	71
A.1	Extrapolation models	71
A.2	Analytical solution of the propagation equation	72
B	Posterior probability distributions	75

1 | Introduction

High-energy astrophysical neutrinos, discovered by the IceCube neutrino telescope in 2013 [1], are incisive probes of physics beyond the Standard Model (BSM). Because they have the highest neutrino energies known, from tens of TeV to a few PeV, they may reveal new particles and interactions at energy scales otherwise unreachable. The great distances that they travel means that even tiny BSM effects affecting them may accumulate and become detectable. In particular, high-energy astrophysical neutrinos have great potential in the study of dark matter.

The nature of dark matter is one of the greatest unresolved mysteries of modern physics. Dark matter has been proven to exist via observations such as rotational velocities of galaxies [2–4]. Despite many searches, neither its mass or interactions with other particles have been identified. Most dark matter searches have focused on weakly interacting massive particles (WIMPs) of GeV mass scales. If the WIMP was produced in the early Universe, it constitutes an excellent dark matter candidate since its thermal relic density would match the dark matter abundance. This is called the WIMP miracle [5]. However, there has been no compelling experimental evidence of the existence of WIMPs, which motivates the search for lighter candidates below the GeV mass range [6, 7].

One of the lighter dark matter candidates is the axion, a hypothetical particle that appears naturally as a solution to the strong CP problem of the Standard Model; specifically, it is the pseudo-Goldstone boson generated by breaking the Peccei-Quinn symmetry [8, 9].

In astrophysics, the existence of axions has been investigated by their mixing with photons, via the Primakoff effect [10]. We explore the less studied case of axions interacting with neutrinos, aiming to place leading constraints on the axion mass and coupling to neutrinos. Our search considers the more general axion-like particles. Contrary to the axion, the axion-like particle has no link between its mass and its coupling strength. This allows us to broaden the search for a dark matter candidate with many possible combinations of mass and coupling.

We probe the particle nature of axion-like dark matter via its interaction with high-energy astrophysical neutrinos. As astrophysical neutrinos from extragalactic origin propagate on their way to Earth, they travel through a background of dark matter. If dark matter consists of axions, and axions couple to neutrinos, we might detect the result of their interaction in the form of characteristic dips and bumps in the energy spectrum of high-energy neutrinos. We use the 7.5-year public sample of IceCube High Energy Starting Events (HESE) [11] to search for these features, with the goal of placing leading constraints on the landscape of axion-neutrino coupling strength and axion mass.

The structure of the thesis is as follows. In Chapter 2 we introduce the concept of dark matter and provide an overview of the dark matter candidates. We motivate the axion and axion-like particle as dark matter candidates, and go through the current constraints on axion properties and the axion-photon landscape. In Chapter 3 we describe the neutrino within the Standard Model framework, and show the production mechanism of high-energy astrophysical neutrinos. We introduce the IceCube neutrino detector and the neutrino event topologies as well as the current status in high-energy astrophysical neutrino observations. In addition, we show the axion-neutrino interaction and the known constraints on the axion-neutrino landscape. In Chapter 4 we follow high-energy neutrinos on their journey from their source to the surface of the Earth described by the propagation equation. We explore the characteristic features of the axion-neutrino interaction in the neutrino spectra at Earth by solving the propagation equation numerically, choosing broad ranges of the axion mass, mediator mass, and the axion coupling strength. In Chapter 5 we model the neutrino propagation from the surface of the Earth to the detector surface by neutrino-nucleon interactions inside the Earth. We investigate the HESE data detected by IceCube and the background of the observations. Furthermore, we calculate the event rates by re-weighting of the flux. In Chapter 6 we develop a Bayesian statistical analysis to compare the IceCube HESE data set to the event rates including the new physics. In Chapter 7 we present the best-fit values and calculate the Bayes factor that represents the statistical preference for explaining the HESE data with a neutrino flux that includes axion-neutrino interactions.

Throughout this thesis, we use natural units. We thus set the speed of light, c , and the reduced Planck constant, \hbar , equal to one: $c = \hbar = 1$.

2 | Dark matter

2.1 Motivation for dark matter

Dark matter is the most abundant type of matter in the Universe, and yet we know very little about it. Unlike normal matter, dark matter does not interact with photons, making it invisible or “dark”. We know about its existence due to effects such as its gravitational pull on other matter, but the identity of dark matter remains unknown.

The search for what makes up dark matter has been going on for many decades, and is one of the greatest unsolved puzzles of modern physics. The first proposal of its existence was made in 1933 by the Swiss astronomer Fritz Zwicky [2]. He studied the Coma galaxy cluster and came to the conclusion that the mass of the cluster, as inferred from the light emitted by visible matter, is not enough to keep the stars bound, given their high observed velocities. As a solution, he suggested the idea of dark matter. At the time, his discoveries went largely unnoticed. Several decades later, American astronomers Vera Rubin, Kent Ford, and Norbert Thonnard carried out investigations of the rotation curves of spiral galaxies. They found that the observed mass of the galaxies could not explain the rotational velocities of their constituent stars [3,4]. The high velocities of the stars in the galaxy would simply cause the galaxy to be ripped apart but somehow that was not the case. It showed an indication of some invisible matter affecting their motion.

We can estimate the missing mass using Newton’s laws. If we set the gravitational force equal to the centripetal force, we find the velocity v of a an object of mass m orbiting the center of mass in a galaxy of mass distribution $M(r)$ at a distance r to be

$$\frac{GmM(r)}{r^2} = \frac{mv^2}{r} \implies v = \sqrt{\frac{GM}{r}}, \quad (2.1)$$

where G is Newton’s gravitational constant. Measuring the rotational velocity of different objects in the galaxy, we can infer what the mass distribution of the galaxy is.

Figure 2.1 shows the rotation curve of the galaxy NGC6503 as a function of distance from the galactic center. The observed data points do not fit the theoretical rotation curve based on only the visible baryonic matter of the galaxy disk and its gas. However, including dark matter, assumed to be distributed in a halo, in the fit, the curve agrees well with the data points. This is used to estimate the matter contribution of the dark matter halo.

Another method used to observe the gravitational effects of dark matter is gravitational lensing. Here the distortion of photons around heavy astrophysical objects may result in a galaxy or galaxy cluster to appear multiple times in astronomical images. Since the deflection

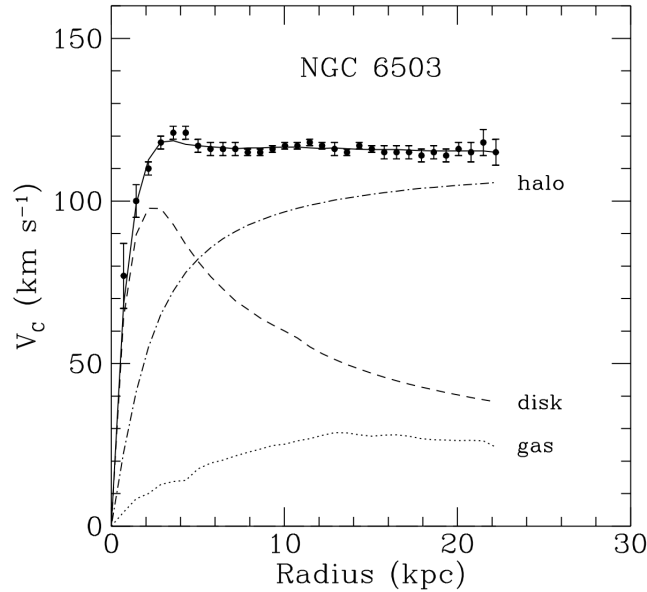


Figure 2.1: Rotation curves of the galaxy NGC6503 from contributions of the visible matter in the disk, the gas and the dark matter halo. The solid line is the sum of the three which is fitted to the data points. Reproduced from [13].

angle of the light depends on the mass distribution of the object of interest, it can be used to estimate the dark matter mass [12].

One way to determine the matter contents of the Universe is by looking at the cosmic microwave background (CMB). The early Universe was not transparent to photons since it was too hot for atoms to form, and so the photons would consistently scatter off of other particles, effectively being trapped. Once the Universe had expanded sufficiently to be cold enough for atoms to form, the photons were able to stream freely through the Universe. This is known as the period of recombination. The relic photon radiation is what we observe today as the CMB. The CMB holds information of the matter anisotropies at the time of recombination: tiny temperature differences of order $\sim 10^{-5}$ K as a result of tiny variations in the density of matter in the early Universe. The anisotropies of the CMB were first discovered by the COBE satellite in 1992 [14]. They reveal that dark matter must have decoupled earlier than regular matter. Dark matter would gather in clumps and form gravitational wells, creating the seed for the galaxy formation structures of the baryonic matter [15].

Today we also see the dark matter is distributed around these large formation structures. Each galaxy is believed to be surrounded by a large halo of dark matter. The dark matter density is concentrated towards the center of the halo, with the density decreasing as a power law further away. Different models describe the density, the most standard including a Navarro-Frenk-White (NFW) profile [16] or a Burkert profile [17]. On the other hand, from the perspective of a larger extragalactic scale, the dark matter is isotropic and homogeneous. When searching for new dark matter candidates forming a cosmological background, this is a good assumption [15].

The concordance model of cosmology is the Λ CDM model, which agrees very well with

current cosmological observations [18]. The model describes the energy density of the Universe. The Λ stands for the dark energy, which is responsible for the acceleration of the expansion of the Universe, while CDM stands for cold dark matter. Cold refers here to the dynamics, meaning that relic dark matter is predominantly non-relativistic. Otherwise it would not have slowed down after the freeze-out and be able to cluster and form the halos we expect to be around galaxies.

The constituents of the Universe are dark energy, matter, and radiation. Matter is further divided into baryonic (visible) matter and dark matter, while radiation is made of photons and neutrinos. However, in the present epoch, the radiation content is several orders of magnitude smaller than the other two. The Planck survey of 2018 has given us the current best estimates of their energy densities [19]:

$$\begin{aligned}\Omega_\Lambda &= 0.685 \\ \Omega_m &= 0.315; \Omega_{\text{DM}} = 0.265, \Omega_b = 0.0496.\end{aligned}\tag{2.2}$$

This means that dark matter makes up 26.5% of the Universe, while the visible matter is only about 5%.

2.2 Dark matter candidates

2.2.1 A quick view on the Standard Model

In order to describe the particle candidates of dark matter, it is necessary first to give a brief overview of the Standard Model physics. Later, in Section 3.1, we elaborate on this, specifically on the role of neutrinos.

The elementary particles and the interactions between them are collectively described by the Standard Model. The particle content of the Standard Model is depicted in Figure 2.2. The particles can be divided into two categories: fermions and bosons. The fermions have half-integer spin and include the leptons, which are either charged, like the electron, or neutral, like the neutrinos. The other section of the fermions is the quarks, which are the building blocks of the composite particles called hadrons. These are either baryons composed of three quarks, such as neutrons and protons which form the nuclei of atoms, or they are mesons which are made up of two quarks, like pions and kaons. Both quarks and leptons have antiparticles with opposite charge.

The bosons have integer spin. The spin-1 gauge bosons describe the fundamental forces: the electromagnetic force mediated by the photon, the strong force mediated by the gluon, and the weak force mediated by the W and Z bosons. They are therefore also called force carriers. The remaining boson is the scalar Higgs boson of spin 0. It gives mass to all the other fundamental particles. The fourth of the fundamental forces is gravity. The boson carrying the gravitational force is yet to be found, although a hypothetical particle called the graviton has been proposed as a candidate [20].

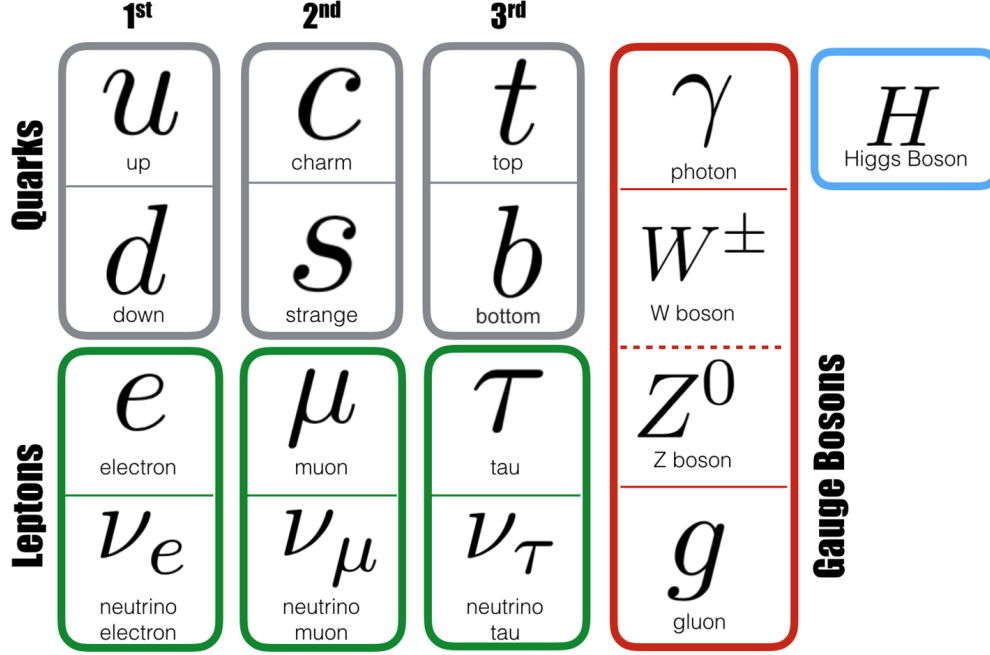


Figure 2.2: The Standard Model describing the elementary particles. From [21].

2.2.2 Properties of a dark matter particle

None of the particles in the Standard model are candidates for dark matter. The neutrinos were once proposed as a candidate since they act so feebly, however, their mass is too small to account for the whole of the dark matter energy density. The neutrino energy density is [22]

$$\Omega_{\nu} = \frac{\sum_i m_{\nu_i}}{93.14 h^2 \text{ eV}}, \quad (2.3)$$

where h is related to the Hubble constant by $H_0 = 100h \text{ s}^{-1} \text{ Mpc}^{-1}$ and given by $h = 0.674$ [19]. For a sum of neutrino masses of $\sum_i m_{\nu_i} \sim 0.1$ this leads to $\Omega_{\nu} \sim 0.002$, far from the dark matter energy density of $\Omega_{\text{DM}} = 0.265$. Additionally, neutrinos are relativistic and will free-stream instead of forming structures. Nevertheless, relic neutrinos do have a large impact on the evolution of the Universe, even if they only make up a tiny fraction of the dark matter energy density [22].

Based on the aforementioned cosmological observations, the properties of a cold dark matter particle can be listed.

- Dark matter should be electrically neutral.
- Dark matter is only known to interact by gravity. Its coupling to the weak or strong force is either very small or does not occur at all. Likewise for self-interactions.
- The dark matter particle must be stable, meaning that it does not decay (at least not within the age of the Universe). This is implied by the fact that it exists today. Theories do exist of unstable dark matter [23] but these are not considered here.

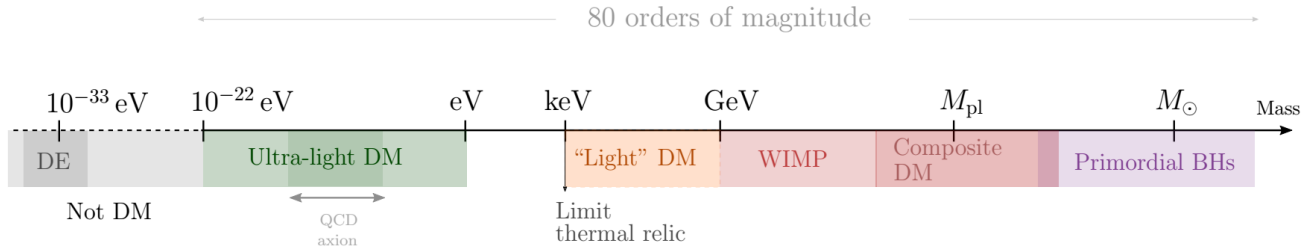


Figure 2.3: Schematic of the different dark matter candidates, covering 80 orders of magnitude in mass. As a comparison, the dark energy (DE) mass range is shown to the left. Reproduced from [26].

- It is expected to be non-relativistic or cold. Hot or warm dark matter may exist, but their contribution to the dark-matter energy density must be sub-dominant to that of cold dark matter [24,25], which can be explained by the lack of clumping for relativistic particles.

Figure 2.3 lists some popular dark matter candidates. It emphasizes the great variety in the mass among the viable dark matter particles of the different models, spanning 80 orders of magnitude. The candidates cover masses from new elementary particles of ultra-light masses to objects of astrophysical scales. Starting with the largest objects, primordial black holes are hypothesized black holes formed in the early Universe, and those with mass of order of a solar mass are dark matter candidates [27]. Composite dark matter include a theory of the existence of dark particles and dark atoms [28] but also cover macro dark matter, potential composite particles formed of quarks and leptons in the early Universe [29]. They could have masses around the Planck mass at $\sim 10^{-5}$ grams.

One of the most well-known of the candidates is the weakly interacting massive particle (WIMP). It interacts weakly and gravitationally and has a GeV-scale mass. The WIMP is also motivated by several different theories, one of them being supersymmetry. In this theory, the WIMP might be a neutralino, predicted to have a mass in the 100 GeV - TeV range [30,31]. The WIMP is an excellent dark matter candidate since if it was produced in the early Universe, its thermal relic density would automatically match the dark matter abundance. This is called the WIMP miracle [5].

The light dark matter category includes the sterile neutrino of $\sim \text{keV}$ mass [32]. This is a hypothetical massive right-handed counterpart to the neutrino. It does not interact weakly but only gravitationally. In principle, the sterile neutrino would also be a WIMP if it had an energy at the GeV scale, however, in that case it is no longer a dark matter candidate. The sterile neutrino is further described in the context of neutrinos masses in Section 3.1.3.

WIMPs have been the primary dark matter candidate in the last decades, with many experiments searching for them. However, there has been no compelling experimental evidence of the existence of WIMPs, which motivates the search for lighter candidates below the GeV mass range [6,7]. One of the more promising ultra-light candidates is the axion. The next section will elaborate on why it is an interesting dark matter candidate to search for.

2.3 Axions and axion-like particles

2.3.1 The strong CP problem

The axion is a hypothetical particle, originally proposed to solve the strong CP problem of the Standard Model. To understand its properties, we have to dive a bit deeper into this problem.

CP stands for charge-conjugation (C) and parity (P). Charge conjugation is a transformation of the charge of a particle, both electromagnetic charge and charge from other forces. It thus transforms the particle into its antiparticle. Parity transformation is the inversion of the spatial coordinates of a particle. This flips the signs of the coordinates, and results in the “mirror” image of the particle. According to the Standard Model, the conservation of CP could be violated in the strong sector. However, no such violation has been observed. CP conservation is violated in the electroweak theory in neutral kaon decay [33], so the question is: why should it not be violated in the strong theory?

CP violation is included in the quantum chromodynamics (QCD) Lagrangian of the strong sector by the so-called θ term. The Lagrangian is given by

$$\mathcal{L}_\theta = \frac{g^2}{32\pi^2} \theta \tilde{G}_{\mu\nu}^a G^{\mu\nu a}, \quad (2.4)$$

where g is the strong coupling, and $G_{\mu\nu}^a$ is the gluon field strength tensor defined by

$$G_{\mu,\nu}^a = \partial_\mu A_\nu^a - \partial_\nu A_\mu^a + g f^{abc} A_\mu^b A_\nu^c, \quad (2.5)$$

where A_μ^a express the eight gluon fields for $a = 1, \dots, 8$, and f^{abc} are the structure constants of SU(3). The dual of the field strength tensor is $\tilde{G}_{\mu\nu}^a \equiv \frac{1}{2} \epsilon_{\mu\nu\rho\sigma} G^{\rho\sigma a}$, where $\epsilon_{\mu\nu\rho\sigma}$ is the Levi-Civita symbol.

The θ term has a value within $-\pi \leq \theta \leq \pi$. If θ is zero, then QCD conserves CP. If θ is non-zero, Eq. (2.4) leads to a neutron electric dipole moment, which is proportional to θ . From observations, the current constraint on this dipole moment is $|d_n| \ll 2.9 \cdot 10^{-26} e \text{ cm}$ [34], where e is the electric charge of the electron, leading to $|\theta| \lesssim 10^{-10}$. There is no motivation within the Standard Model for why the value of θ should be zero, so it is peculiar that it is so close to zero. This is called the strong CP problem.

In 1977, Peccei and Quinn came up with a solution to the strong CP problem by introducing an extension to the Standard Model [8, 9]. Instead of being a constant, they made θ dynamical by introducing a field a , with an associated decay constant f_a . This was done with the introduction of a global $U(1)$ symmetry that was spontaneously broken. Thus the system would seek the lowest energy configuration of the potential, the vacuum state, and be naturally zero. The θ field can now be written as

$$\theta \rightarrow \theta + \frac{a}{f_a} \quad (2.6)$$

such that Eq. (2.4) becomes

$$\mathcal{L}_\theta = \frac{g^2}{32\pi^2} \left(\theta + \frac{a}{f_a} \right) \tilde{G}_{\mu\nu}^a G^{\mu\nu a}. \quad (2.7)$$

The excitation of a dynamic field a gives rise to a new particle, a Nambu-Goldstone boson. These are bosons that appear necessarily in models exhibiting spontaneous breakdown of continuous symmetries [35]. This means that initially the system is invariant under the symmetry, but then a minimum of the potential of the system is reached, and since it could be one of many possible minima, the symmetry is broken “spontaneously”. Since the symmetry is also broken explicitly (there was never an exact symmetry to begin with), the particle will be a pseudo Nambu-Goldstone boson which has a small mass.

The fact that the Peccei-Quinn (PQ) mechanism introduces a new particle — a light boson — was shown independently by Wilczek and Weinberg: [36, 37]. They gave the particle the name *axion*. It is predicted to have no charge and no spin. It should only have weak couplings to other particles, since it would otherwise already have been discovered. The neutral pion gets its mass from the same explicit symmetry breaking as the axion, and thus the axion and pion mix. The axion mass m_a is then related to the pion mass m_π by $f_a m_a \sim f_\pi m_\pi$, where f_a is the axion decay constant, and f_π is the pion decay constant. A full treatment leads to the relation [38]

$$m_a = 5.691(51)\mu\text{eV}(10^{12} \text{ GeV}/f_a). \quad (2.8)$$

2.3.2 Axion-like dark matter

Axions have all the right properties to be dark matter candidates: no direct interaction with photons (except for axion-photon conversions, which we show below), and only very small couplings to the weak force, if any. If axions exist, they could also explain the baryon asymmetry of the Universe. This is the fact that there must have been more baryonic matter than antimatter in the early Universe since the Universe today is dominated by matter. The baryon asymmetry is not explained by the Standard Model. The axion could account for the matter-antimatter asymmetry by its proportionality to a CP-violation parameter [39, 40].

The axion mass is not constrained by its origin in the strong CP problem. It is expected to be ultra-light, which includes any energies from 1 eV and many orders of magnitude below (see Figure 2.3). If axions are to explain the whole dark matter density by themselves, this imposes a trade-off between the axion mass and the axion number density. The lighter the axion mass, the higher their number density should be higher to account for the relic dark matter density observed.

On the other hand, the axion has a strong link between its mass and coupling to the strong force, $g_{a\gamma\gamma}$. This relation is determined by the axion decay constant f_a as seen in Eq. 2.8, with also $g_{a\gamma\gamma} \propto 1/f_a$ [41]. If a certain coupling strength is ruled out by observations, then the corresponding axion mass is ruled out as well. However, one can generalize this by positing the existence of a particle with properties akin to the axion, as light as the axion, but whose mass and decay constant are not related by the PQ-mechanism. E.g., the axion-like particle might have a very small mass but a very high coupling to another particle [42]. This defines the general class of axion-like particles (ALPs). By construction, they have many similarities to the axion: they are light, have no coupling the electromagnetic force, and are thus equally good dark matter candidates. Additionally, ALPs are not associated with the strong CP problem since they do not necessarily couple to the strong force. The particles we search for in this project can equally well be axions and ALPs, since the theory works in both cases.

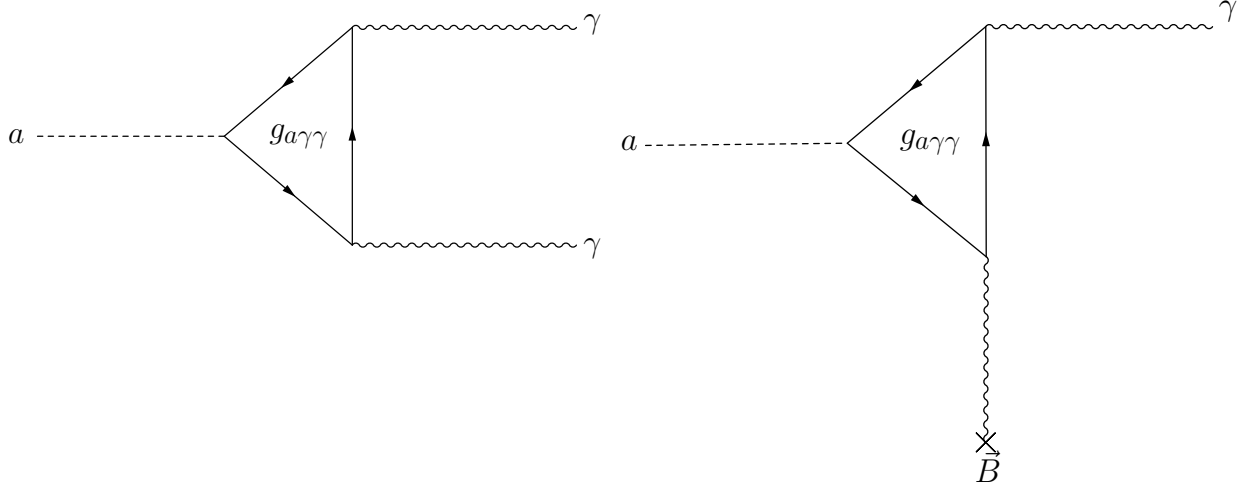


Figure 2.4: Feynman diagrams of axion-photon interactions. a) Axion decay or axion-photon conversion in vacuum. (b) Inverse Primakoff effect. It shows the conversion $a \rightarrow \gamma$ in the presence of a strong magnetic field.

We will thus refer to both types of particles simply as axions.

2.3.3 Searches and constraints

Axions are most commonly searched for via their connection to photons. They could be directly observed using a theoretical effect called the Primakoff effect, which was first discussed in the context of resonant photoproduction of neutral mesons in the presence of an external electromagnetic field [10]. The Primakoff effect was later discussed to also work with axion-photon interactions, where it would occur when photons encounter a strong magnetic field and are converted into axions (or vice versa).

Figure 2.4 (a) shows a Feynman diagram of the axion-photon conversion in vacuum, while Figure 2.4 (b) shows a Feynman diagram of the inverse Primakoff effect. When an axion comes near an electromagnetic field, it may convert into a photon. The Lagrangian of this process is given by

$$\mathcal{L} = g_{a\gamma\gamma} a \vec{E} \cdot \vec{B}, \quad (2.9)$$

where a is the axion field, $g_{a\gamma\gamma}$ is the coupling between the axion and the photons, \vec{E} is the electric field, and \vec{B} is the magnetic field. When searching for axions, a cavity containing a magnetic field can be tuned to match the expected resonant frequency of the axion-photon conversion. If axions exist, the conversion is expected to happen in the magnetic field of the Sun and of other stars [43–45]. This would produce axions that we could later observe here on Earth.

A peculiar way to search for axions directly by the Primakoff effect is the light-shining-through-wall experiment [46, 47]. If photons can convert into axions then a laser pointing towards a wall could be observed on the other side of the wall as well, provided that the photons have converted into axions and back again as they crossed the wall. This could be

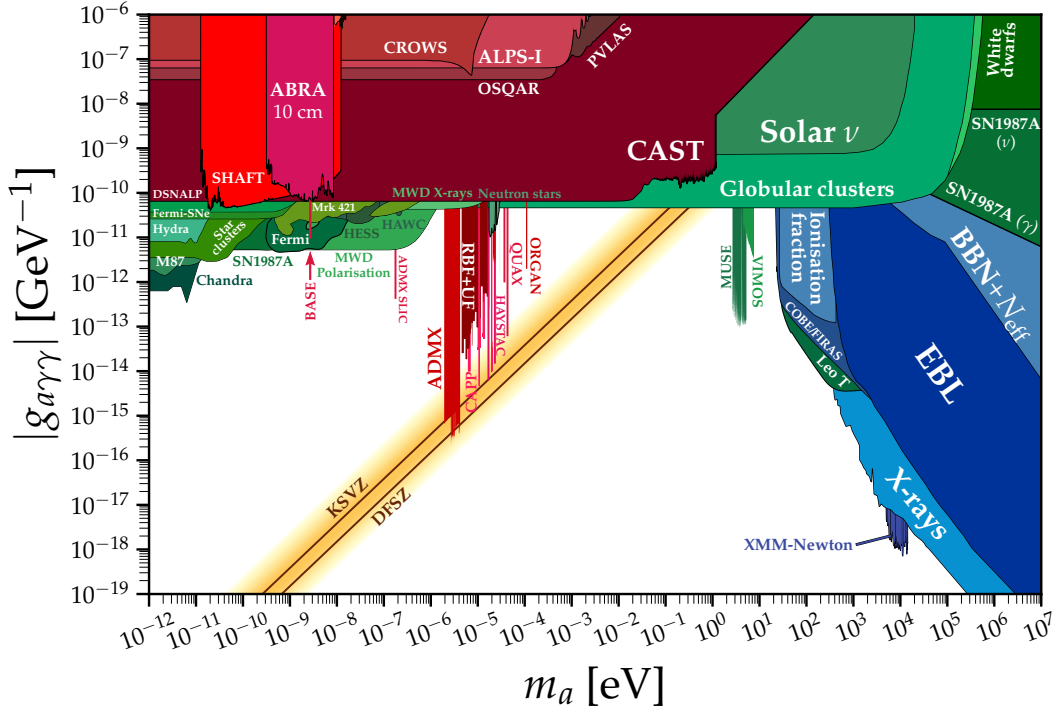


Figure 2.5: Landscape of the axion mass and axion-photon coupling of current experimental and observational limits. Red is haloscopes and helioscopes, green is astrophysical constraints, blue is cosmological constraints, yellow is the QCD band. The QCD axion is a band, since the coupling strength and mass are linked. Figure from [49]. Constraints come from haloscopes [50–76], helioscopes [77–86], astrophysical observations, [87–122], and cosmological observations [123, 124]. The band for KSVZ and DFSZ are from [125–128].

obtained with very strong magnets on either side of the wall. Experiments like the OSQAR experiment at CERN are currently trying to observe axions this way [48].

Figure 2.5 shows the parameter space of axion mass m_a and the axion-photon coupling $g_{a\gamma\gamma}$ currently allowed by a large variety of experiments. The constraints are from haloscopes and helioscopes (red), astrophysics (green), and cosmology (blue). In addition, the figure shows the preferred parameter space of the QCD axion from theory (yellow). One of the helioscopes is the CERN axion solar telescope (CAST), which is trying to detect axions from the Sun using a strong magnet. No axions have been observed, but the experiment has placed some of the strongest constraints on the axion-photon coupling [78, 79]. Haloscope experiments use resonant microwave cavities to observe axions, like HAYSTAC [67, 68] and ADMX [50–53]. They have also placed constraints on the axion properties but have been unsuccessful with detection. The astrophysical constraints come from different astronomical observations. One example is globular clusters where the axion production in stellar cores could affect the number ratio of stars [87, 102]. The cosmological bounds come from, e.g., the expected dark matter decoupling time related to Big Bang nucleosynthesis [123]. The constraints on the QCD axion come from theories of a pseudo Nambu-Goldstone boson arising from a breaking of the Peccei-Quinn symmetry. The two models are the Dine-Fischler-Srednicki-Zhitnitsky

(DFSZ) axion [125, 126] and the Kim-Shifman-Vainshtein-Zakharov (KSVZ) axion [127, 128]. Their implementation and couplings vary, which is why there is a slight difference between the two bands on Figure 2.5.

In general, there are increasingly strong limits being put on the m_a vs. $g_{a\gamma\gamma}$ landscape, narrowing the parameter space where the axion could exist significantly. In this thesis, we instead search for a coupling between axions and neutrinos, since almost no experimental limits on it are found so far in the literature (we go into detail about this in Section 3.4.1). The next chapter introduces the phenomenology of the neutrino and its possible interaction with the axion.

3 | Neutrinos

3.1 In the Standard Model and beyond

Neutrinos are elementary particles and thus part of the Standard Model (see Figure 2.2). The neutrinos have spin $\frac{1}{2}$ which makes them fermions. Specifically, they are part of the lepton sector. As the name suggests, neutrinos are electrically neutral and have a very small mass. Like the charged leptons – electrons e , muons μ and taus τ – the neutrinos come in three generations or flavors, namely electron neutrinos ν_e , mu neutrinos ν_μ , and tau neutrinos ν_τ . In addition, each neutrino flavor comes with an antiparticle. A neutrino of a given flavor is associated to the charged lepton of that flavor and carries the same lepton number, conserved per flavor. The electron neutrino is the neutrino flavor that is emitted together with an electron in the decay of a W boson, and similarly for the muon and tau neutrino.

Neutrinos only interact gravitationally or via the weak force, which is several orders of magnitude weaker in strength than the electromagnetic and strong forces. As a consequence, neutrinos rarely interact and can travel long distances unaffected by their environment. They are thus also very difficult to detect.

3.1.1 Neutrino oscillations

In the 1960s, a neutrino detection experiment was set up in the Homestake mine. The goal was to observe solar neutrinos [129]. The experiment consisted of a large tank of chlorine, where the neutrinos could be detected by the production of a radioactive isotope of argon. According to the standard model of the Sun, only electron neutrinos are produced in the fusion processes, so this was the type of neutrino that they were searching for [130]. However, only about a third of the expected neutrino flux was detected, which was a big mystery. Other experiments such as the Kamiokande detector and the GALLEX experiment found the same discrepancies between prediction and observation [131, 132]. The problem became known as the *solar neutrino problem* and was unsolved for many years.

The solution to the solar neutrino problem was provided by neutrino oscillations: the change of one neutrino flavor into another as the neutrino propagates. To describe neutrino oscillations, we consider that each neutrino flavor is a linear superposition of the mass eigenstates (ν_1, ν_2, ν_3). It is only when it interacts, that it is observed as one of the flavor states (ν_e, ν_μ, ν_τ). A neutrino state can be expressed in either one of these two bases. The mixing between the mass states and the flavor states is described by the unitary 3×3 PMNS

(Pontecorvo-Maki-Nakagawa-Sakata) matrix, given by [133, 134]

$$\begin{pmatrix} \nu_e \\ \nu_\mu \\ \nu_\tau \end{pmatrix} = \begin{pmatrix} U_{e1} & U_{e2} & U_{e3} \\ U_{\mu1} & U_{\mu2} & U_{\mu3} \\ U_{\tau1} & U_{\tau2} & U_{\tau3} \end{pmatrix} \begin{pmatrix} \nu_1 \\ \nu_2 \\ \nu_3 \end{pmatrix}. \quad (3.1)$$

The PMNS matrix can be parameterized by three mixing angles θ_{12} , θ_{13} , θ_{23} , and a complex phase, δ_{CP} . The mixing angles describe the rotations between the mass and flavor states, and the phase factor can account for charge-parity violation.

The probability of transitions between the different neutrino flavors depends on the mixing angles and the squared-mass differences of the mass states, $\Delta m_{ij}^2 = m_i^2 - m_j^2$, where $i, j = 1, 2, 3$ for $i \neq j$. For a two-flavor approximation, the probability of a electron neutrino propagating into a muon neutrino is

$$P(\nu_e \rightarrow \nu_\mu) = \sin^2(2\theta_{12}) \sin^2\left(\frac{\Delta m_{21}^2 L}{4E_\nu}\right), \quad (3.2)$$

where L is the distance traveled by the neutrino and E_ν is the neutrino energy. The probability of the electron neutrino to turn into a muon neutrino thus oscillates over distance with $\sin^2(2\theta_{12})$ being the amplitude of the oscillation.

The solution to the solar neutrino problem was thus that a neutrino emitted with an electron flavor could later be measured to have another flavor. The solar electron neutrinos could be observed at Earth as any one of the three flavors, which is why only a third of the expected flux was observed in the Homestake experiment. This was not confirmed until many years later with observations by the Sudbury Neutrino Observatory [135].

3.1.2 Neutrino mass

From neutrino oscillations we know that neutrinos must have a mass. However, the neutrino masses have not been measured directly. The reason is that the oscillation probability depends on the differences of the squared neutrino masses, Δm_{ij}^2 , and not the individual masses m_{ν_i} of eigenstate ν_i for $i = 1, 2, 3$. The current upper bound on the sum of the neutrino masses is $\sum_{i=1}^3 m_{\nu_i} < 0.12 \text{ eV}$ [19]. Neutrinos are hence the lightest of the massive particles of the Standard Model.

Figure 3.1 shows the two possibilities for the neutrino mass hierarchy. The mass difference Δm_{21}^2 , also called Δm_{sol}^2 , describing the difference between mass states ν_1 and ν_2 , is the smallest of the mass differences with $\Delta m_{21}^2 \approx 7 \cdot 10^{-5} \text{ eV}^2$ [136]. Since the value is positive, we know that $m_{\nu_2} > m_{\nu_1}$. The other squared-mass differences are $\Delta m_{31}^2 \approx \Delta m_{32}^2 \approx \pm 2.5 \cdot 10^{-3}$. It is unknown whether $\Delta m_{31}^2 > \Delta m_{32}^2$ or if $\Delta m_{32}^2 > \Delta m_{31}^2$. There are thus two possible neutrino mass hierarchies: the normal hierarchy where $m_{\nu_3} > m_{\nu_2}$ and the inverted hierarchy where $m_{\nu_2} > m_{\nu_3}$.

3.1.3 Sterile neutrinos

According to the Standard Model, only the left chiral component of the neutrinos interact weakly (and the right chiral component for antineutrinos), since they only interact by the

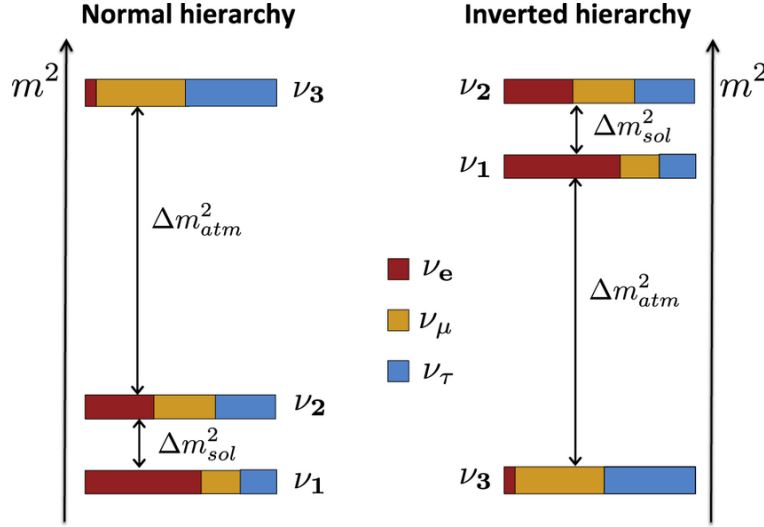


Figure 3.1: The two possible neutrino mass hierarchies. From [137].

weak force, which is parity-violating. This is unlike any of the other fermions. Neutrinos are therefore massless in the Standard Model, since both left and right chirality parts are required for a particle to have a mass.

The non-zero mass of the neutrinos shows us that we need to modify the Standard Model. One possible way for the neutrinos to gain mass is via the seesaw mechanism [138]. Here a right-handed counterpart to the left-handed neutrino is introduced which does not interact by the weak force but only by gravity. It is therefore also called a sterile neutrino, opposite to the “normal” active neutrino. The right-handed neutrino is introduced by a Majorana mass term. It is called a seesaw mechanism since the heavier the mass of the sterile neutrino, the lighter the mass of the active neutrino. It explains why the neutrinos are so light compared to the masses of the other fermions in the Standard Model. The seesaw mechanism gives it a GUT-scale mass of $\sim 10^{12}$ eV. GUT stands for Grand Unified Theory, and the GUT-scale is the energy scale which we believe strong and electroweak interactions are unified in a single interaction [138].

Separately, the existence of a sterile neutrino, with a mass lower than the GUT-scale, is motivated by anomalies found in different neutrino experiments. These experiments include the LSND $\bar{\nu}_e$ appearance in a $\bar{\nu}_\mu$ beam [139], and the MiniBooNE detector which reported an unexplained excess of low-energy neutrinos [140]. Mixing with a fourth, sterile neutrino would explain the discrepancies found.

The sterile neutrino could also be a dark matter candidate of mass order keV [32]. The observation of a 3.5 keV X-ray line from galaxy clusters motivates a sterile neutrino mass of about 7 keV [141, 142].

In the context of the axion-like dark matter and neutrino interactions in this work, the sterile neutrino is an important tool, however we denote it as a heavy neutral lepton in this case. In Section 3.4, we consider interactions between active neutrinos and axions, mediated by a sterile neutrino. Because its mass is unknown, we vary it over many orders of magnitude in our analysis.

3.2 Astrophysical neutrinos

Neutrinos exist over a broad energy range, from 10^{-6} eV for relic neutrinos to possibly 10^{18} eV ultra-high-energy neutrinos. In our investigation of the possible interaction between neutrinos and axion-like dark matter (see Section 3.4), the neutrinos of interest are of astrophysical origin. The astrophysical neutrinos cover the higher-energy part of the energy spectrum. They include:

- Solar neutrinos of keV–MeV (10^3 – 10^6 eV) energies
- Supernova neutrinos of MeV (10^6 eV) energies
- High-energy neutrinos of TeV–PeV (10^{12} – 10^{15} eV) energies
- Ultra-high-energy (UHE) neutrinos of EeV (10^{18} eV) energies

To study the axion-neutrino couplings, we focus on high-energy astrophysical neutrinos. This is because of two reasons. First, they come from extragalactic sources, Mpc–Gpc distances away, so during their long trip to Earth, they have a higher chance to interact with the cosmic axion-like dark matter background. Second, their high energies allow us to probe heavy axion-neutrino mediator masses (more on this in Section 3.4). UHE neutrinos are predicted, but still undiscovered.

The astrophysical sources of neutrinos are also called point-sources since they are observed coming from a specific point in the sky. Generally, point-sources are divided into two categories based on their temporal profiles: transient sources and steady-state sources. The transient sources only emit neutrinos for a limited amount of time. These include supernovae, the more luminous hypernovae, and gamma ray bursts, which are highly energetic jets of gamma rays. Of the transient sources, only one class has been confirmed observed in neutrinos: the supernova SN1987A in the Large Magellanic Cloud. About 25 neutrinos was observed in total by several detectors at Earth: Kamiokande [143], Irvine-Michigan-Brookhaven [144], and Baksan [145]. However, supernovae emit neutrinos at MeV energies [146] and not high-energy neutrinos. The second type of neutrino source is a steady-state source, where a continuous flow of neutrinos is emitted from the source. High-energy candidate sources include active galactic nuclei which are the supermassive black holes in centers of a galaxies that emit neutrinos and other particles in jets from the center [147]. There have been no observations of confirmed steady-state neutrino sources.

Rather than point-source neutrino fluxes, we use the diffuse high-energy neutrino flux, which is the collected neutrino flux from all high-energy neutrino sources. This leads to a continuous all-sky neutrino flux to observe, making it possible to look for effects of the axion-neutrino interactions in the detected neutrino spectra.

3.2.1 High-energy astrophysical neutrino production

High-energy neutrinos are produced by UHE cosmic rays, which are protons and nuclei with energies in excess of 100 PeV. There are two expected neutrino production chains:

proton-proton (pp) interactions and proton-photon ($p\gamma$) interactions. The interactions predominantly produce delta baryons that decay into pions and neutrons, ultimately creating neutrinos. The production chain for a $p\gamma$ interaction looks like the following:

$$p + \gamma_{\text{bg}} \rightarrow \Delta^+ \rightarrow \begin{cases} \pi^+ + n \rightarrow \begin{cases} \pi^+ \rightarrow \mu^+ + \nu_\mu, & \mu^+ \rightarrow e^+ + \nu_e + \bar{\nu}_\mu \\ n \rightarrow p + e^- + \bar{\nu}_e \end{cases} \\ \pi^0 + p \rightarrow \gamma + \gamma + p \end{cases} \quad (3.3)$$

The branching ratio of the charged pion branch is $\frac{1}{3}$ and the neutral pion branch ratio is $\frac{2}{3}$. The photons produced in the neutral pion branch contribute to the gamma-ray emission from the source. The neutrino flavor ratio from the $p\gamma$ interaction is thus $N_{\nu_e} : N_{\nu_\mu} : N_{\nu_\tau} = 1 : 2 : 0$. The anti-electron neutrino produced in the neutron decay has a low energy since the proton mass is close to the neutron mass, so it does not count in the flavor ratio. Due to neutrino oscillations and the fact that we look at the diffuse astrophysical neutrino flux, the flavor ratio evens out, such that at detection it will be $N_{\nu_e} : N_{\nu_\mu} : N_{\nu_\tau} = 1 : 1 : 1$. The produced neutrinos will have about 5% of the parent proton energy.

The production of high-energy neutrinos takes places in astrophysical environments with large magnetic fields, where the cosmic rays are magnetically confined and accelerated to ultra-high energies. A necessary condition to accelerate of charged particles to high energies is confinement. This is known as Hillas' criterion [148]. For the confinement to take place, the Larmor radius of the charged particles should not exceed the size of the accelerator region. It is the radius of the trajectory of a charged particle in a uniform magnetic field, given by $r = mv_\perp/(|q|B)$, where m is the mass of the particle, v_\perp is its velocity perpendicular to the magnetic field, q its charge, and B is the strength of the magnetic field.

Cosmic rays are accelerated by first-order Fermi acceleration, also called diffuse shock acceleration [149, 150]. Charged particles will repeatedly be scattered back and forth between magnetic turbulences and gain energy for every shock by the plasma. An analogy is a game of ping pong, where the ball gains energy every time it is hit by the bat of one the players. The cosmic rays eventually escape when they reach very high energies.

Fermi acceleration leads to a power-law distribution in energy of the cosmic rays: $E^{-\gamma} = E^{-2}$, where γ is an adimensional constant called the spectral index. When the high-energy neutrinos are produced in pp or $p\gamma$ interactions, it will be from the tail-end of the energy of those cosmic rays. This means the power-law energy distribution of neutrinos is expected to be softer than the distribution of cosmic rays, so the spectral index for high-energy neutrinos is assumed to be between 2 and 3. This power-law picture is true for the diffuse neutrino flux. The point sources may individually have other processes, which lead to other energy distributions.

The ultra-high-energy neutrinos can be produced in similar processes as the high-energy neutrinos from cosmic rays of higher energies. Another production mechanism is when UHE cosmic rays interact with background of the interstellar medium, like the CMB or the extragalactic background light (EBL) [151]. These are called cosmogenic neutrinos.

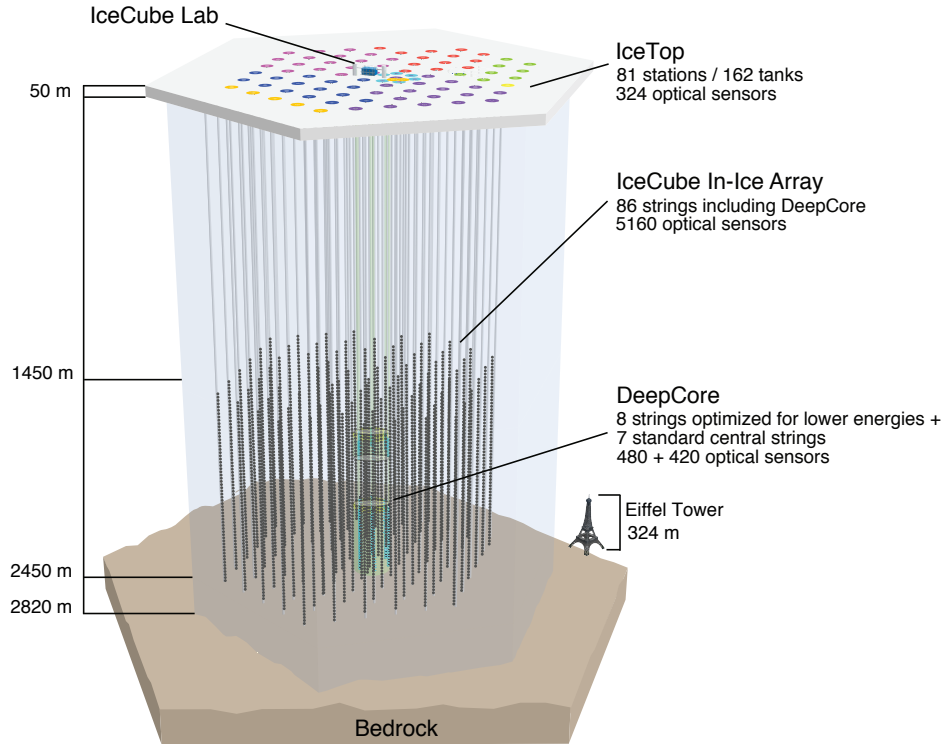


Figure 3.2: Schematic of the IceCube Neutrino Observatory. From [152].

3.3 IceCube telescope and neutrino detection

The largest high-energy neutrino telescope in operation is the IceCube Neutrino Observatory. The detector is located at the South Pole, built into the ice. It consists of 86 strings lowered 1.5–2.5 kilometers into the ice [152]. Each string is composed of 60 digital optical modules (DOMs) where a photomultiplier tube (PMT) is placed, detecting the incoming light from neutrino interactions. In total, the strings span a grid of approximately 1 km^3 .

Figure 3.2 illustrates the setup of the IceCube experiment. The spacing of the DOMs in the In-Ice Array is optimized for the detection of high-energy astrophysical neutrinos, and is thus the array relevant for this thesis. IceTop is an air shower array, detecting secondary particles from cosmic-ray showers in the atmosphere. In the lower middle part of the detector, the strings are placed closer together to optimize the detection of atmospheric neutrinos. This sub-array is called DeepCore.

3.3.1 Neutrino-nucleon interactions

Neutrinos are detected indirectly by their interactions with nucleons in the ice. At high neutrino energies, above about 20 GeV, the dominant neutrino-nucleon interaction is deep inelastic scattering [153]. There are two main processes: charged-current (CC) interactions and neutral-current (NC) interactions. In a CC interaction, the incoming neutrino interacts with a nucleon to create a charged lepton of the same flavor. The nucleon breaks apart and

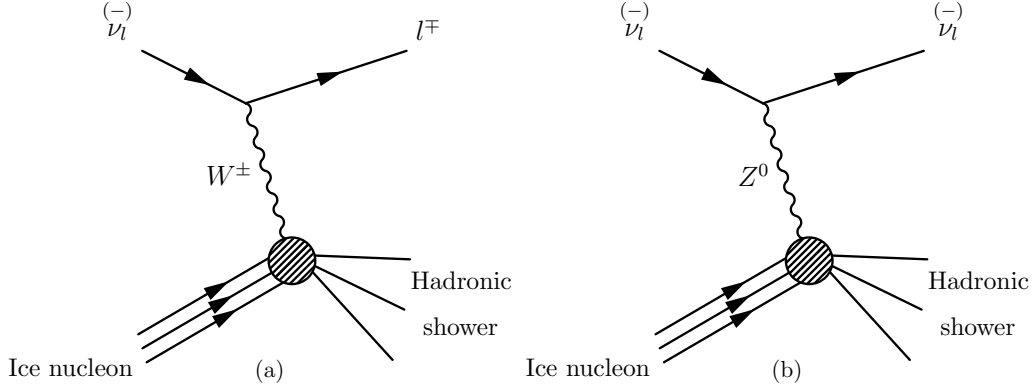


Figure 3.3: Feynman diagrams of the deep inelastic scattering interactions happening when neutrinos interact with the ice of IceCube. (a) Charged current interaction. A neutrino of flavor $l = e, \mu, \tau$ interacts with an ice nucleus, producing a charged lepton of the same flavor by exchange of a W boson. A hadronic shower is also emitted. (b) Neutral current interaction. A neutrino interacts with the ice and exchanges a Z boson, producing a neutrino of the same flavor and a hadronic shower.

produces a hadronic shower. The mediator of this interaction is the W boson. In a NC interaction, the neutrino also interacts with a nucleon, but this time by exchange of a Z boson, producing a neutrino of the same flavor. Again a hadronic shower occurs. Figure 3.3 illustrates the CC and NC interactions.

When charged particles move through a dielectric medium with a speed faster than the speed of light in the medium, they emit Cherenkov radiation of optical and ultraviolet frequencies [154,155]. The effect occurs since the particles excite the surrounding atoms, causing them to consequently emit photons which interfere constructively, creating radiation in a cone shape. If a neutrino interacts in the ice inside the IceCube detector volume, the Cherenkov radiation emitted by the final-state charged particles is detected by the PMTs, which transforms the photon signal into an electric signal that is transferred to the rest of the DOM.

The Cherenkov radiation from a neutrino-nucleon interaction has different topologies inside the detector depending on the final-state particles. In both CC and NC interactions, the hadronic shower leads to a signal that can be seen as a spherical shape across the DOMs called a *cascade*. A neutrino produced in a NC interaction leaves no additional signal, and so the NC interaction is recognized on this cascade. In ν_e and ν_τ CC, the outgoing electron or tauon scatters quickly in an electromagnetic shower which also leads to a cascade. In ν_μ CC, the final-state particle is a muon which has a long lifetime of $\tau_\mu \simeq 2\mu$ s. This is enough time for it to propagate through the detector and make an event type called a *track*, created by the molecules it excites while traveling by. In rare cases, the CC final-state tauon might instead of an electromagnetic shower produce a so-called double bang [156], where two small showers can be seen. It can also decay into an electron or a muon.

Tracks are distinguishable, and thus the muon neutrino is often clearly identified. In addition, the track direction is nearly the same as the incoming neutrino direction. Since the track direction can be reconstructed to within less than 1° [157], tracks are ideal to search for point sources of high-energy neutrinos. However, since the muon often exists the detector before it has deposited all its energy, it is difficult to reconstruct the original energy of the

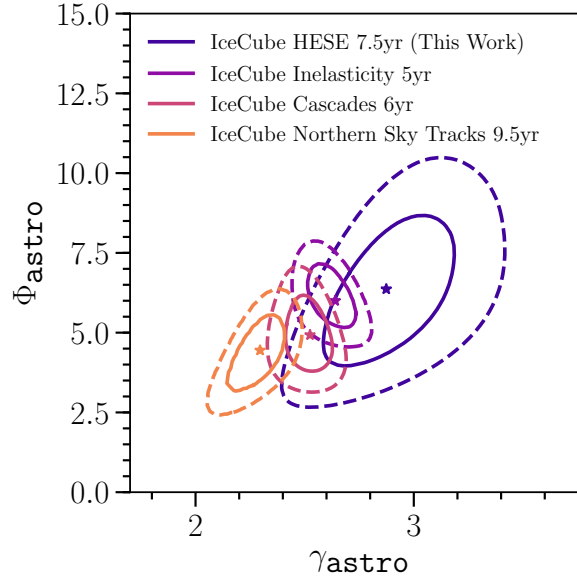


Figure 3.4: The best-fit value of the spectral index in the HESE 7.5 year analysis, compared to best-fit results from different IceCube samples. The solid lines surround the 68% confidence levels, and the dashed lines surround the 95.4% confidence levels. From [11].

neutrino. On the other hand, the cascades from the ν_e and ν_τ CC events and from the NC interaction are contained in IceCube, which makes us able to reconstruct the neutrino energies. However, the angular resolution is bad, so the neutrino event does not point back to the source. Furthermore, it is difficult to tell the incoming neutrino flavors apart. The tauon neutrino can though be identified by the occasional double bang.

This thesis will use data of high-energy neutrinos observed by IceCube. As explained, this data will include information about the energy spectrum, the arrival direction, timing, and flavor composition.

3.3.2 Status in IceCube high-energy astrophysical neutrino observations

IceCube discovered the existence of a diffuse flux of high-energy astrophysical neutrinos in 2013 [1]. The diffuse high-energy neutrino spectrum is well-described by a power law in energy, independent of neutrino flavor. This distribution is as expected from the predicted acceleration processes of cosmic rays in the astrophysical sources. Currently, no neutrinos above 10 PeV have been observed, which means that UHE neutrinos are yet to be confirmed [158]. The diffuse flux that IceCube detects is compatible with being isotropic, since it does not have an excess of neutrinos in any specific direction. Therefore, the diffuse flux is likely predominantly of extragalactic origin.

Figure 3.4 shows a contour plot of the fit of the spectral index from the High Energy Starting Events (HESE) analysis [11]. The best-fit value yields of $\gamma = 2.87^{+0.20}_{-0.19}$.

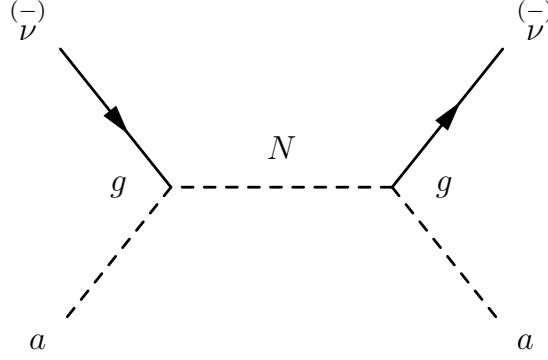


Figure 3.5: Feynman diagram of the s -channel interaction between high-energy (anti)neutrinos $(\bar{\nu})$ and axion dark matter a , mediated by a heavy neutral lepton N . The strength of the interaction is g .

As explained in Section 3.2, different sources of high-energy astrophysical neutrinos have been proposed. However, except the SN1987A, none of them have been fully confirmed in observations. One event to notice is the detection of a neutrino signal in the direction of the blazar TXS 0506+056 made in 2015 by IceCube, which was coincident with a gamma-ray flare [159]. A blazar is a sub-class of active galactic nuclei, which has the jet pointed towards the Earth. Later investigation of archival data also showed an excess of neutrinos in that direction with a 3.5σ significance.

The high-energy neutrinos observed by IceCube are not only important to explain the processes behind the production of the high-energy particles in the sources and identify them, but they are also ideal probes of new physics, since they reach higher energies than particles in any man-made accelerators. This includes secret neutrino interactions with the cosmic neutrino background [160], sterile/active neutrino oscillations [161], and interactions with dark matter, the latter which is investigated in this thesis.

3.4 Neutrinos interacting with axion-like dark matter

The fundamental particle nature of dark matter can be probed with different particle interactions that have Standard Model particles in their final state. Axion-neutrino interactions could thus be proved, in principle, via neutrino production from pair annihilation, neutrino production from axion decay, and elastic scattering between neutrinos and axions. We will focus on the latter. The axion-neutrino scattering could happen as high-energy neutrinos propagate from their astrophysical sources towards the Earth. On their way, they might interact with a cosmic background of axion-like dark matter.

Figure 3.5 shows the Feynman diagram of the axion-neutrino elastic scattering. The interaction happens between active (anti)neutrinos denoted by $(\bar{\nu})$, and axion-like particles denoted by a . The strength of the interaction is given by the adimensional coupling strength g . We assume that the coupling strength is flavor-diagonal and universal, such that $g_l \equiv g$ for $l = e, \mu, \tau$. Consequently, we investigate the propagation of only one species of neutrinos.

The mediator of the axion-neutrino interaction is a heavy neutral lepton N (also called a sterile neutrino, see Section 3.1.3). We assume that the axion dark matter is a boson of spin 0, and since the neutrino is a fermion of spin $\frac{1}{2}$, the heavy neutral lepton is a scalar to conserve the spin of the interaction.

Since the mediator is on-shell, the axion-neutrino scattering is resonant in the s -channel depicted. In this case the t -channel contribution is sub-dominant [162]. The interaction being resonant makes it possible to see a significant effect of an elastic scattering in the neutrino spectra observed by IceCube. That the interaction is resonant means that the probability of axion-neutrino interaction is enhanced. This results in an attenuation of neutrinos with energies near the resonance energy, leading to a dip at resonance energy in the neutrino spectra. The scattering also leads to a regeneration of the outgoing neutrino, which means it will have a lower energy than originally. This is observable as a bump in the neutrino spectra. The dip and the bump are hence characteristic features that we can search for in the IceCube high-energy neutrino data.

Since the cross section of the axion-neutrino interaction is resonant, we have to regularize it to avoid it being divergent. On that account, we use a Breit-Wigner cross section [163], since it models resonances without any divergence. The cross section is given by

$$\sigma_{a\nu N} = \sigma(a + \nu \rightarrow N \rightarrow a + \nu) = \frac{1}{16\pi} \frac{g^4 s}{(s - m_N^2)^2 + m_N^2 \Gamma^2}, \quad (3.4)$$

where $\sqrt{s} = \sqrt{2E_a E_\nu + m_a^2}$ is the center-of-mass energy (CoM-energy), m_N is the mass of the mediator, and Γ is the heavy neutral lepton decay width. The axion energy is denoted E_a and is given by $E_a = (1 - \beta^2)^{-1/2} m_a$, where $\beta_a = v_a/c = 7 \cdot 10^{-4}$ is the average axion-like dark matter velocity [164, 165]. The decay width Γ can be expressed by [162]

$$\Gamma = \frac{g^2 m_N}{4\pi}. \quad (3.5)$$

The cross section is resonant when $s = m_N^2$, corresponding to a neutrino energy of

$$E_{\text{res}} = \frac{m_N^2 - m_a^2}{2E_a}, \quad (3.6)$$

Interactions between axions and neutrinos are more probable to happen when the neutrino energy is close to the resonance energy. The cross section does not depend on the neutrino mass; instead, it depends on the coupling strength, the axion mass, and the heavy neutral lepton mass. The values of these parameters are largely unknown. Hence they are not fixed a priori but are inferred from data. They will be varied over many orders of magnitude when modeling the flux in Chapter 4.

3.4.1 Current axion-neutrino landscape

To the best of our knowledge, the only existing constraint on the axion-neutrino coupling is from Ref. [166]. This work constrains the coupling $g_{a\nu N}$ of a scattering between neutrinos and dark-matter axions using a heavy neutrino mediator, equal to the interaction we use.

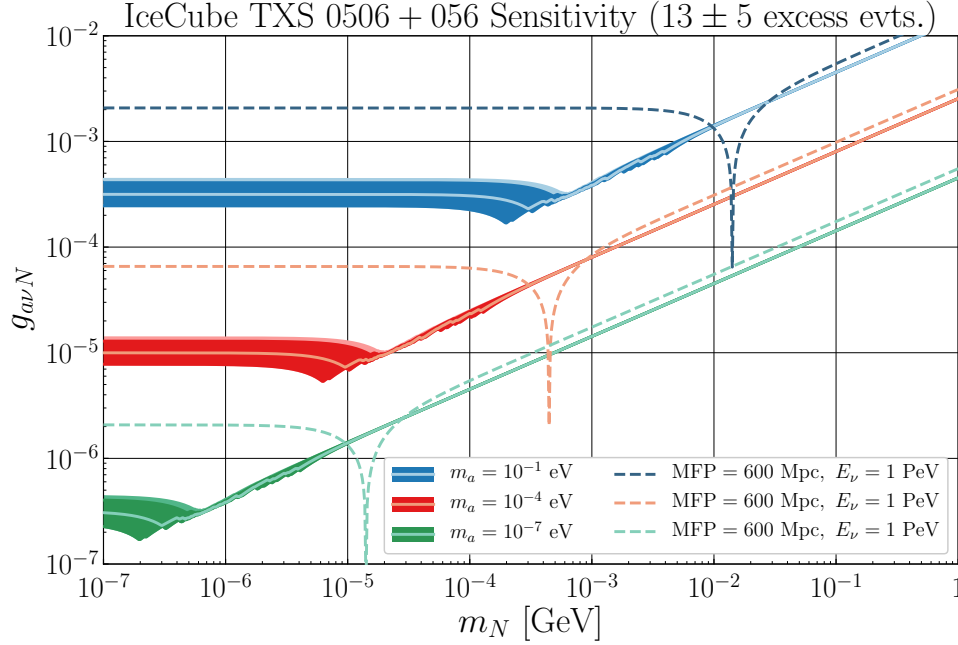


Figure 3.6: Constraints on the axion-neutrino coupling as a function of the mass of the heavy neutral lepton mediator for three different choices of axion mass: 10^{-1} eV, 10^{-4} eV, and 10^{-7} eV. The best fit value for each axion mass is the line at the center of each region, while the darker region shows $\pm 1\sigma$ and the lighter colored region outside this shows $\pm 2\sigma$. The constraints are based on neutrino events from the blazar TXS 0506+056. The dashed lines represent typical neutron star merger neutrinos with a constant mean free path of 600 Mpc and energies of 1 PeV. Figure from [166].

However, it employs a slightly different s -channel cross section. The constraints are based on the observations of a total of 13 neutrinos coming from the blazar TXS 0506+056 (described in Section 3.3.2).

Figure 3.6 shows the results of the analysis in Ref. [166]. They place constraints on $g_{a\nu N}$ as a function of mediator mass m_N , using three different axion masses. To make a comparison to other searches for point-sources of high-energy astrophysical neutrinos, the dashed lines correspond to the typical energy and mean free path of neutrinos expected from neutron star mergers.

With our analysis we aim to explore larger ranges of the coupling strength $g_{a\nu N}$ and the mass of the heavy neutral lepton mediating the axion-neutrino interaction. Additionally, we will place constraints on the axion mass in relation to the coupling strength.

4 | The high-energy neutrino flux at Earth

4.1 Derivation of the propagation equation

The high-energy astrophysical neutrino flux can be modeled by the propagation equation. It describes the propagation of high-energy astrophysical neutrinos from their sources towards the Earth, including the possible coupling between high-energy neutrinos and a cosmic background of axion-like particles. To compute it, we use a diffuse isotropic neutrino flux, i.e., the accumulated emission of the entire population of extragalactic high-energy neutrino sources, integrated across all redshifts.

The time evolution of the neutrino propagation is as follows: neutrinos are emitted at a time $t < 0$ and reach the Earth when $t = 0$. The neutrino energy at time t is E_ν . The comoving number density of the neutrinos is denoted by $n_i(t)$. As the neutrinos propagate, we follow the evolution of \tilde{n} , defined by $\tilde{n}(t, E_\nu) \equiv dn(t, E_\nu)/dE_\nu$. When reaching the Earth, the isotropic diffuse high-energy neutrino flux is

$$\Phi_\oplus(E_\nu) \equiv \frac{dN_\nu}{dE_\nu dA dt d\Omega} = \frac{c}{4\pi} \tilde{n}(0, E_\nu), \quad (4.1)$$

where N_ν is the number of neutrinos, A is the area, Ω is the solid angle, and c is the speed of light and also approximately that of the neutrinos. To compute the evolution of the comoving number density and thereby the diffuse flux, we solve the propagation equation. It is given by

$$\frac{\partial \tilde{n}(t, E_\nu)}{\partial t} = \frac{\partial}{\partial E_\nu} [H(z) E_\nu \tilde{n}(t, E_\nu)] + \mathcal{W}(z) \mathcal{L}_0(E_\nu) - \Sigma(t, E_\nu) \tilde{n}(t, E_\nu) + \mathcal{R}(t, E_\nu), \quad (4.2)$$

inspired by Eq. (2) in Ref. [160]. The propagation equation is recast in terms of redshift instead of time by using the relation $dz/dt = -[(1+z)H(z)]^{-1}$ [167], where $H(z)$ is the Hubble parameter, given by $H(z) \approx H_0 \sqrt{\Omega_\Lambda + \Omega_m(1+z)^3}$. Here the Hubble constant is $H_0 = 100h \text{ s}^{-1} \text{ Mpc}^{-1}$, the vacuum energy density is $\Omega_\Lambda = 0.685$, the matter density is $\Omega_m = 0.315$, and $h = 0.674$ [19]. This yields

$$\begin{aligned} \frac{\partial \tilde{n}(z, E_\nu)}{\partial z} = & -\frac{1}{(1+z)H(z)} \left\{ \frac{\partial}{\partial E_\nu} [H(z) E_\nu \tilde{n}(z, E_\nu)] \right. \\ & \left. + \mathcal{W}(z) \mathcal{L}_0(E_\nu) - \Sigma(z, E_\nu) \tilde{n}(z, E_\nu) + \mathcal{R}(z, E_\nu) \right\}. \end{aligned} \quad (4.3)$$

The first two terms on the right-hand side of Eq. (4.3) describe the standard picture of neutrino propagation, where the neutrinos do not interact with any particles, i.e., they free-stream from the sources to the Earth. The first term is the adiabatic cosmological expansion of the Universe, which causes the neutrinos to experience an energy loss at the rate of $H(z)E_\nu$ as they propagate. The second term accounts for the injection of neutrinos by the astrophysical sources. \mathcal{W} describes the redshift evolution of the number density of the neutrino sources. It follows the star formation rate [168], such that most sources will be at a redshift of $z \approx 1$. The diffuse flux of the injected neutrinos given by $\mathcal{L}_0(E_\nu)$ is expected to follow a power law: $\mathcal{L}_0(E_\nu) \propto E_\nu^\gamma$, where γ is the spectral index.

The last two terms of Eq. (4.3) account for the axion-neutrino interactions. In the third term, the interaction rate is $\Sigma = n_a(z)\sigma_{a\nu N}(E_\nu)$, where $n_a(z)$ is the number density of axions, and $\sigma_{a\nu N}(E_\nu)$ is the axion-neutrino cross section (see Eq. (3.4)). Since we assume that dark matter is made up of axions, we assume the axion density is equal to the canonical local dark matter density: $n_a(z=0) = \rho_{\text{DM}}/m_a = 0.3(\text{GeV}/m_a) \text{ cm}^{-3}$ [169]. At higher redshifts this is $n_a(z) = n_a(z=0)(1+z)^3$.

The fourth term on the right-hand side of Eq. (4.3) accounts for the regeneration of the neutrinos after the interaction. The incoming neutrino has the energy E'_ν and will be regenerated at an energy E_ν . The regeneration is expressed by

$$\mathcal{R}(z, E_\nu) = n_a(z) \int_{E_\nu}^{\infty} dE'_\nu \tilde{n}(z, E'_\nu) \frac{d\sigma_{a\nu N}(E'_\nu)}{dE_\nu}, \quad (4.4)$$

inspired by Eq. (7) of Ref. [170]. Since the axion-neutrino interaction is assumed to happen via the s -channel, we can divide the differential cross section into the total cross section and an energy distribution function: $d\sigma_{a\nu N}(E'_\nu)/dE_\nu = \sigma_{a\nu N}(E'_\nu)f(E'_\nu, E_\nu)$. If N is Majorana, the angular distribution of the daughter particles in the decay $N \rightarrow \nu + a$ is isotropic [171], causing the energy distribution $f(E'_\nu, E_\nu)$ to be flat and we end up with

$$\mathcal{R}(z, E_\nu) = n_a(z) \int_{E_\nu}^{\infty} dE'_\nu \tilde{n}(z, E'_\nu) \sigma_{a\nu N}(E'_\nu) \frac{3}{E'_\nu} \left(\frac{E_\nu}{E'_\nu} \right)^2, \quad (4.5)$$

where the factor 3 accounts for the normalization of the energy distribution function:

$$\int_0^{E'_\nu} dE_\nu f(E'_\nu, E_\nu) = 1. \quad (4.6)$$

4.2 Solution of the propagation equation

The propagation equation of Eq. (4.3) is solved numerically. The equation is evolved in redshift by integrating over the interval $z_{\text{max}} = 4$ to $z_{\text{min}} = 0$. The choice of z_{max} is generous, based on the star formation rate. There may be neutrino sources beyond $z = 4$, but they are so far away that their contribution to the flux that reaches Earth is insignificant. The initial condition is thus $\tilde{n}(z_{\text{max}}, E_\nu) = 0$.

Our goal is to compare the event rate at IceCube expected from a given neutrino flux, computed under axion-neutrino interactions, with the real experimental data of IceCube and

look for effects of the axion-neutrino interaction in the data. We thus need to ensure that the solution of the propagation equation results in a flux with characteristic features inside of the IceCube observational energy range. The high-energy neutrino range that IceCube observes is about 10 TeV to 10 PeV. The lower limit arises due to the background from atmospheric muons and atmospheric neutrinos: below 1 TeV the astrophysical neutrino events become indistinguishable from the atmospheric neutrino events and there is a large background of atmospheric muons. The background will be explained in further detail in Section 5.2. The upper limit is a result of the fact that there have been no observations of neutrinos of higher energies as explained in Section 3.3.2. Sources might accelerate neutrinos to higher energies, but this flux is not observed yet.

We solve the propagation equation over a generous energy range of $10^3 - 10^{12}$ GeV, since the resonance of the axion-neutrino interaction might introduce effects that cover a broader range in energy of the neutrino spectra than the IceCube range. For example, the resonance energy might be at an energy higher than the maximum energy to which IceCube is sensitive, but broad features may be visible far from the resonance and inside the IceCube energy range. If the higher neutrino energy was not included in the simulation, these features would not be taken into account in the analysis. We do not include energies below 1 TeV, even though the features could be observable in IceCube from a resonance energy lower than 1 TeV, simply because the background is too high.

To account for a decrease in neutrinos of higher energies, we introduce an exponential cut-off in energy to the neutrino spectra, E_{cut} , which will be a free parameter of our analysis. Adding this to the neutrino injection term of the propagation equation, we get $\mathcal{W}(z)\mathcal{L}_0(E_\nu) = \mathcal{W}(z)E_\nu^{-\gamma} \exp(-E_\nu/E_{\text{cut}})$. Presently, with 7.5 years of IceCube astrophysical neutrino data [11], there is no evidence for a cut-off yet. Regardless, we include the cut-off in our analysis because the spectral feature that it introduces on the diffuse flux may mimic the features introduced by axion-neutrino interactions. Hence, not including the cut-off could over-represent the sensitivity to axion-neutrino interactions.

We solve Eq. (4.3) numerically for varying values of the following free model parameters: the mass of the axion, m_a , the mass of the heavy neutral lepton mediator, m_N , the coupling strength of the axion-neutrino interaction, g , the spectral index of the neutrino production, γ , the cut-off energy, E_{cut} , and the all-flavor normalization of the flux at 100 TeV, Φ_0 . The latter is not varied in the numerical solution but rather fitted for later, since the normalization is just a re-scaling parameter.

Figure 4.1 shows an example of the neutrino spectrum for a solution to the propagation equation with different terms of the propagation equation turned on. The flux of free-streaming neutrinos is a flat line, except for the cut-off at the end. The axion-neutrino leaves an attenuation dip in the neutrino spectrum, which is the third term of the right-hand side of Eq. (4.3). The characteristic feature to notice is a depletion of neutrinos at the resonance energy. The solid curve includes the regeneration of the neutrinos as well, which results in a small bump just below resonance energy.

The three parameters describing the axion-neutrino interaction are the two masses, m_a and m_N , and the coupling strength g . Their values will determine the placement of the attenuation dip, its width, and its depth. It can be seen from Eq. (3.6) how the resonance energy is determined by the two masses; a large mediator mass leads to a high resonance

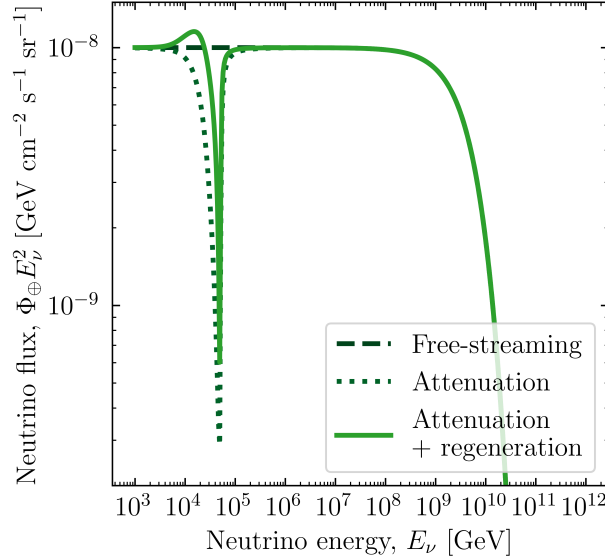


Figure 4.1: Example of the characteristic features from the axion-neutrino interaction on the neutrino flux at Earth. The dashed curve is the free-streaming case of the propagation equation; the dotted curve includes the attenuation of neutrinos from the axion-neutrino interaction; and the solid curve includes both the attenuation and the regeneration from the axion-neutrino interaction. All fluxes are normalized to $10^{-8} \text{ GeV cm}^{-2} \text{ s}^{-1} \text{ sr}^{-1}$ at 1 TeV. In this plot, the high-energy neutrino flux was computed using $m_N = 10^{-3} \text{ GeV}$, $m_a = 10^{-11} \text{ GeV}$, $g = 10^{-4.125}$, $\gamma = 2$, $E_{\text{cut}} = 10^{10} \text{ GeV}$.

energy, while a large axion mass leads to a low resonance energy. The depth and the width of the dip follow the cross section, which is highly dependent on g by $\sigma_{a\nu N} \propto g^4$. The cross section also depends on m_a and m_N (see Eq. 3.4).

Figure 4.2 shows how each of the parameters impacts the flux, except for the flux normalization which we keep fixed for illustration. Figure 4.2 (a) sketches how the shape of the flux is affected by each parameter. The remaining five plots show the impact of each parameter individually. The figures with red fluxes describe the parameters of the axion-neutrino interaction, and the purple fluxes describe the parameters related to the production of neutrinos.

As explained above, the parameters of the axion-neutrino interaction affect the dip in three different ways. The three figures, 4.2 (b), (c), and (d) describe this relation. Firstly in figure (b), five fluxes are shown for five different values of the mediator mass. As the mediator mass increases, it causes a shallower and narrower dip, while the dip occurs at increasingly higher energies. In figure (c), we see that the axion mass has the same impact as the mediator mass, except the dip moves to lower energies as m_a increases. In figure (d), the dip increases both in depth and width as the coupling strength increases.

In practice, since we solve the propagation equation for a fixed grid of values of neutrino energy (Section 4.3), the solver rarely calculates the flux at the resonance energy exactly. Instead, the distance between the resonance energy and the nearest energy point will differ depending on the free parameters. Consequently, the depth of the dip depends not only on

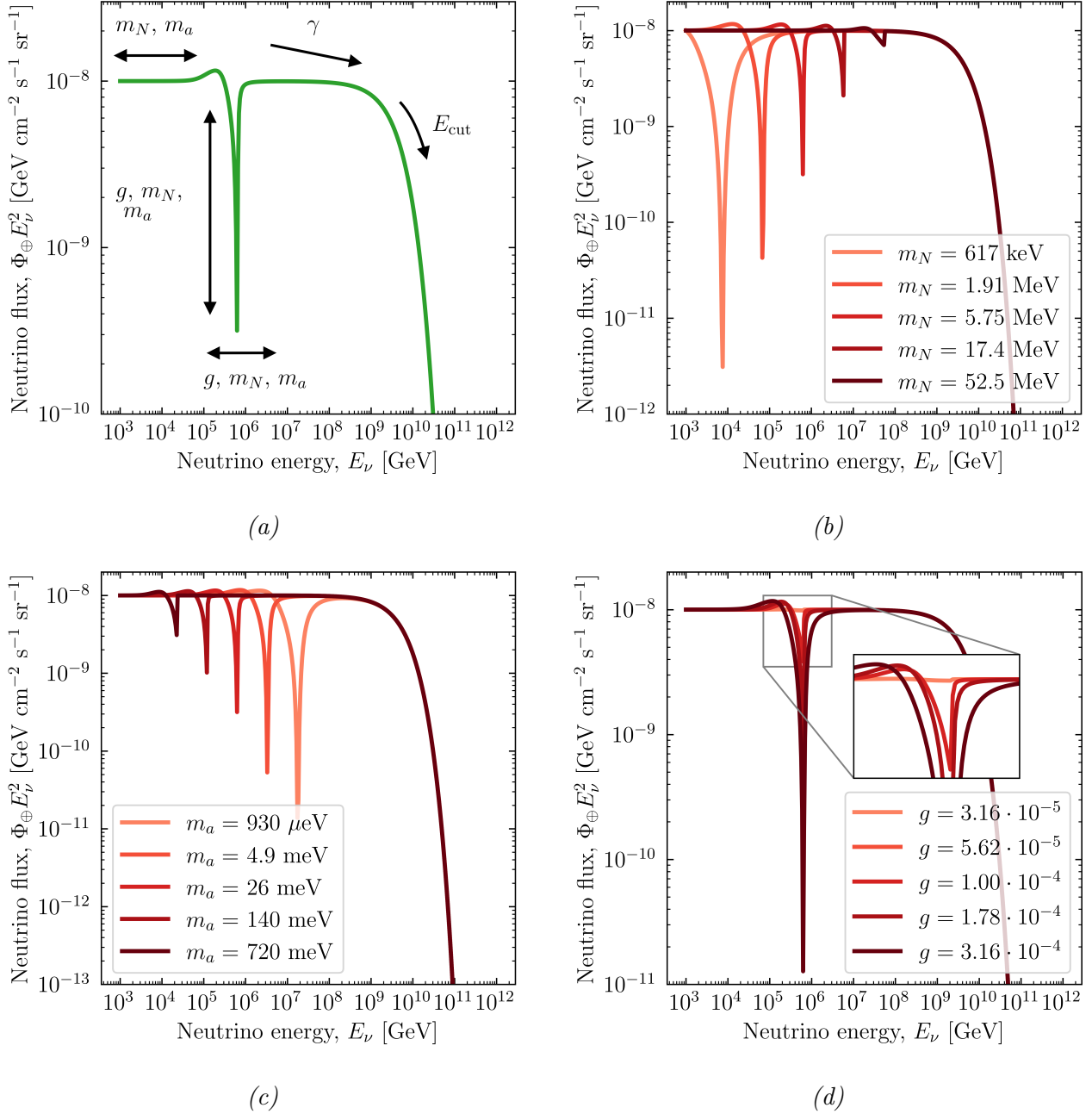


Figure 4.2: Impact of each of the free parameters on the neutrino spectra. (a) This figure shows how each parameter affects the neutrino spectrum. (b) Impact of the mediator mass on the flux. The dip decreases and moves to higher energies with increasing m_N . (c) Impact of the axion mass on the flux. The dip increases and moves to higher energies with increasing m_a . (d) Impact of the coupling strength on the flux. The dip becomes deeper and wider with increasing g . (Continues on next page.)

the parameters but also on how close the resonance energy is to the nearest node of the neutrino-energy grid. Regardless, Figure 4.2 is an accurate representation of the effect of the parameters on the flux.

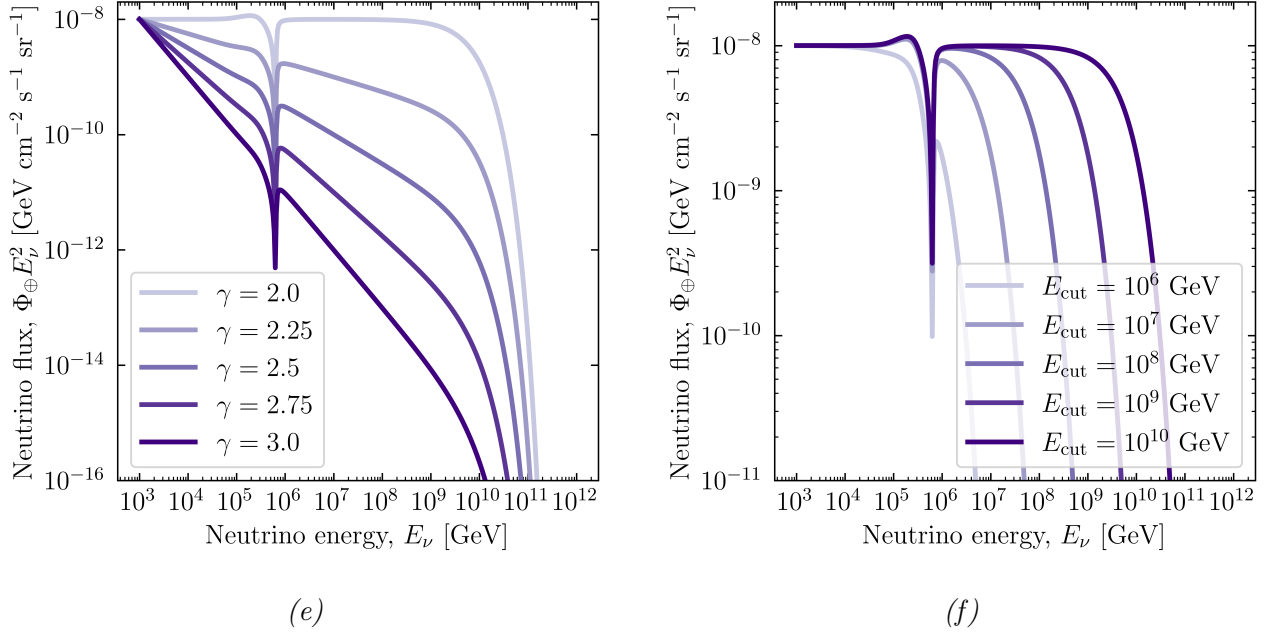


Figure 4.2: (Continued from previous page.) (e) Impact of the spectral index on the flux. The slope increases while the visibility of the dip decreases with increasing γ . (f) Impact of the cut-off energy on the flux. If the cut-off energy is close to the resonance energy, the bump and the dip becomes distorted. In figures (b)-(e), one of the free parameters is varied while the values of the other parameters are kept constant: $m_N = 10^{-2.24}$ GeV, $m_a = 10^{-10.59}$ GeV, $g = 10^{3.75}$, $\gamma = 2$, $E_{\text{cut}} = 10^{10}$ GeV. The fluxes are normalized to 10^{-8} $\text{GeV cm}^{-2} \text{s}^{-1} \text{sr}^{-1}$ at 1 TeV.

The spectral index, γ , and the cut-off energy, E_{cut} , which are related to the production of neutrinos, are varied in figure (e) and (f). In figure (e) it can be seen that as the spectral index increases, the slope of the flux becomes steeper. As a consequence, the bump becomes smaller, since there are fewer neutrinos at higher energies to take from. Figure (f) shows how the energy cut-off affects the flux. The cut-off will distort the spectral features on the flux from the axion-neutrino interactions if its value is lower or close to the resonance energy.

4.3 Numerical implementation

To explore the parameter space of axion-neutrino interactions for a wide range and finely spaced grid of model parameter values, we favored to compute the numerical solution of the propagation equation in C++, where implementation is fast. Our solver is an implicit Gaussian second order Runge-Kutta, as implemented in the GNU Scientific Library (GSL) [172]. (A higher-order Runge-Kutta would give a higher precision in the solution, however testing the solution with different orders showed negligible differences in the flux. Since the second order Runge-Kutta provides a good balance between precision and time, we chose this).

We vary the values of the five model parameters m_N , m_a , g , γ , and E_{cut} over wide

ranges, since their values are largely unknown, and solve the propagation equation for each value assignment. To compute the neutrino flux for a large number of points in this five-dimensional parameter space, we run our solver in parallel on a large number of computer cores on our local high-performance computing cluster.

We solve the propagation equation in redshift steps of $\Delta z = 10^{-3}$. This was tested to be the sweet spot between precision and time. In reality, the step size is only an upper limit, since the GSL solver will vary the step size according to the slope of the flux. To reduce the run time, we computed the integral in the regeneration term of the propagation equation with a Riemann sum instead of using GSL for integration.

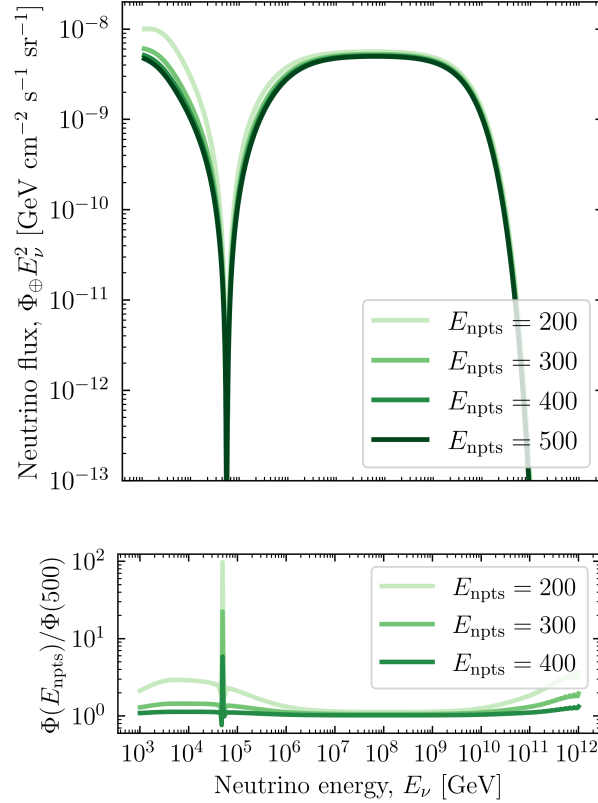


Figure 4.3: Fluxes computed for a different number of energy points. The fluxes converge as the number of energy points increases. We choose 400 energy points for the simulations since this flux is almost the same flux as for 500 energy points, but the computation is a lot faster. The flux is normalized to $10^{-8} \text{ GeV cm}^{-2} \text{s}^{-1} \text{sr}^{-1}$ at 1 TeV for the flux with 200 energy points. The fluxes have the parameter values $m_N = 10^{-3} \text{ GeV}$, $m_a = 10^{-11} \text{ GeV}$, $g = 10^{-3.5}$, $\gamma = 2$, $E_{\text{cut}} = 10^{10} \text{ GeV}$. In the plot below, we calculate the ratios of the fluxes with different number of energy points compared to the flux with 500 energy points. The fluxes are interpolated to span over 500 energy points in the energy range. The ratio with 400 energy points shows no significant differences over most energies, except at the dip and the end of the spectrum. However, it can be seen on the figure above that these differences are insignificant visually.

Figure 4.3 shows how the resolution of localized features in the neutrino energy spectra

changes as the number of energy points increases for a given set of parameter values. The energy points are spaced logarithmically over the $10^3 - 10^{12}$ GeV energy range. We find that the flux converges as the number of energy points increases; the flux of 200 energy points differs a lot more from a flux with 300 energy points than a flux of 300 energy points differs from a flux of 400 energy points. Since 400 and 500 energy points result in almost the same flux, as it can be seen in the bottom plot, we choose to solve the propagation equation for 400 energy points to save run time.

4.3.1 Constraining the parameter space

The model parameters m_N , m_a , g , γ , and E_{cut} of the solution to the propagation equation span a five-dimensional parameter space. The parameters of special interest are m_N , m_a , and g , since they describe the properties of the axion-neutrino interaction, which we want to place constraints on. We want to cover as broad a range as possible of different values of the three parameters, since the order of magnitude of the values are unknown, as explained in previous sections.

In order to be able to place constraints on the values of the model parameters, the characteristic features in the flux should be observable. In other words, the ranges of the parameters will contain, but not be limited to, regions where the features from the axion-neutrino coupling appear within the chosen energy range. The goal is to avoid computing the fluxes outside of these regions to save run time. One way to quantify whether the features will be observable is via the axion-neutrino interaction length. The interaction length is the mean distance traveled by a particle before it undergoes an interaction. For the axion-neutrino interaction it is given by

$$\ell_{\text{int}}(g, m_a, m_N, E_\nu, z) = \frac{1}{n_a(m_a, z)\sigma_{a\nu N}(g, m_a, m_N, E_\nu)} = \frac{1}{\Sigma(g, m_a, m_N, E_\nu, z)}. \quad (4.7)$$

If the interaction length is long, few axion-neutrino interactions will occur, and the dip will not be prominent. On the other hand, if the interaction length is short, many interactions will happen and we will see a prominent dip. For a neutrino flux with a very short interaction length, the numerical solution of the propagation equation can have a very long run time. The reason is that when the solver approaches the energy where the dip is, it takes increasingly small steps in redshift to find the solution. As the dip gets deeper and deeper, the run time will increase exponentially. Hence, it is not a problem to compute a solution with a small dip, but it is extremely slow when the dip is wide and deep.

With this in mind, we set up a number of criteria for determining the regions of the parameter space where we should explicitly solve the propagation equation. The criteria are:

1. **The features of the axion-neutrino interaction should be within the observable energy range of IceCube.** The resonance energy of the axion-neutrino interaction or the spectral features of the interaction should be within the energy range observable by IceCube. As determined in Section 4.2, this leads to an energy range of $1 \text{ TeV} \leq E_{\text{res}} \leq 10 \text{ EeV}$.

2. **The axion-neutrino interaction should be probable.** In some regions of the parameter space, the interaction length is too large for the interaction ever to occur across the chosen redshift range. To avoid computing the fluxes in this region, we place an upper limit on the interaction length: $\ell_{\text{int}} \leq 10$ Gpc, corresponding to approximately the size of the observable Universe [167, 173].
3. **The propagation equation should be solvable within reasonable run time.** In cases where the interaction length is very small, the resonant dip is very steep. As a result, the run time increases exponentially, to a point where the numerical solution of the propagation equation ends up with an unreasonably long run time. The run time optimization implementations described in Section 4.3 are not enough to reduce the run time significantly in the most extreme cases. We therefore place a lower limit on the interaction length: $\ell_{\text{int}} \geq 50$ pc, corresponding to a run time of approximately one hour for one flux, which is fast enough to compute the large number of fluxes of the analysis.

The computed fluxes which do not fulfill the first two criteria will be computed as power-law fluxes, with a high-energy cut-off, corresponding to the case of free-streaming neutrinos in Eq. 4.3. The power-law fluxes are computed for different ranges of the γ and E_{cut} . The fluxes not meeting the third criteria but the first one are extrapolated from the computed solutions that meet all criteria. The lower limit on the interaction length is tested to produce enough fluxes needed for the extrapolation. The extrapolation method is elaborated on in Section 4.3.2.

Figure 4.4 shows how the criteria divide up the parameter space for (a) the first criterion on the energy and (b) the second and third criteria on the interaction length. The resonance energy is determined by the axion mass and the mediator mass, see Eq. (3.6). The values of these parameters that result in the features on the neutrino spectra being within the IceCube range are contained in the blue region in Figure 4.4 (a). The gray region to the left yields fluxes with resonance energy below 1 TeV, while the gray region to the right yields the fluxes with resonance energy above 10 EeV. The white region includes the combination of parameters for which the axion mass is larger than the mediator mass, which will result in a negative resonance energy. Even though a negative energy is unphysical, in this case it just means that the resonant features never appear, so the flux is a power law. Figure 4.4 (b) shows the interaction length criteria based on values of the mediator mass and the coupling strength. The gray region to the left of the band contains fluxes with interaction length less than 50 pc, while the gray region to the right of the band contains fluxes with interaction length greater than 10 Gpc.

Figure 4.5 illustrates all three criteria of the parameter space as a function of the mediator mass and the coupling strength for four different values of the axion mass. The blue lines surround the band where the resonant features on the neutrino spectra fulfill the first criterion from Figure 4.4 (a), and the orange lines surround the band in Figure 4.4 (b) containing the fluxes satisfying the second and third criteria on the interaction length. At the overlap between the blue band and the orange band, all criteria are satisfied and we compute the full solution of the propagation equation. This is marked by the green hatched region. Above this region, where the first criterion is satisfied but the interaction length is below 50 pc, we

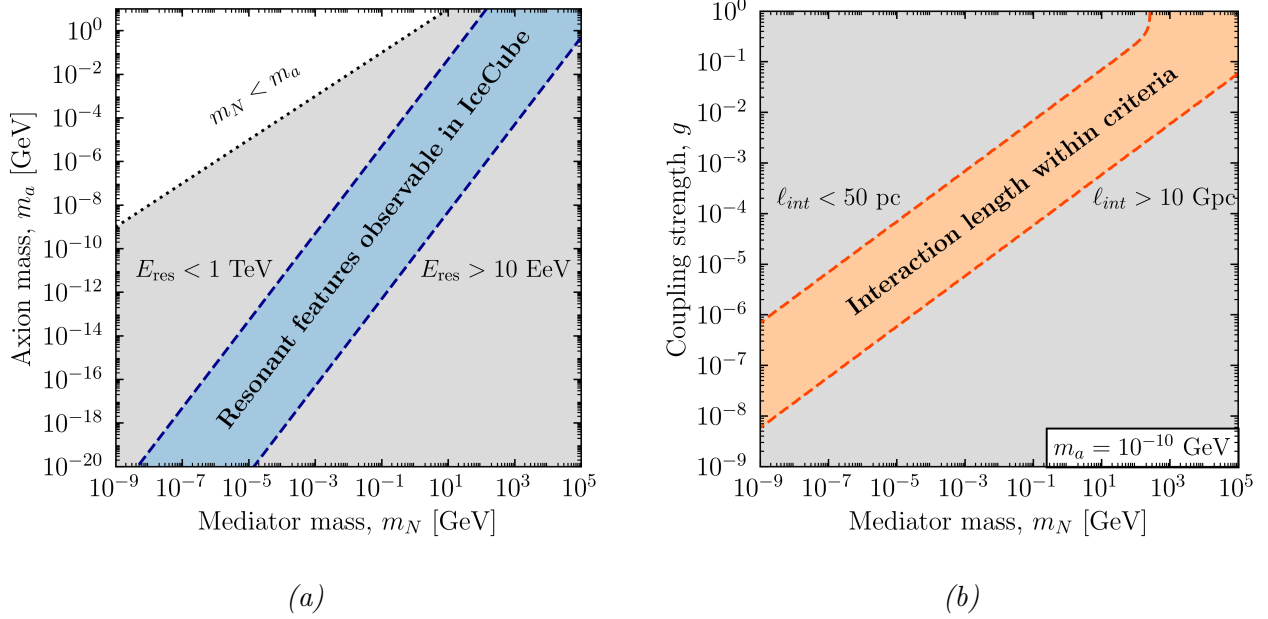


Figure 4.4: (a) Contour plot of the values of the axion mass m_a and heavy neutral lepton mass m_N which will allow for the resonant features of the axion-neutrino interaction to be observable within the IceCube range (in blue). The white region is where the resonance energy is negative, which occurs when $m_N < m_a$. (b) Contour plot of the values of the mediator mass and coupling strength which fulfill the criteria set for the interaction length for a fixed axion mass.

extrapolate the fluxes. This is marked by dark green. Since the light green region constitutes such a small part of the parameter space, it underlines the need for extrapolating the fluxes where possible.

In principle, the interaction length should be calculated at an energy equal to the resonance energy, since here its value will be minimal. However, when the cross section is evaluated at resonance energy, it becomes independent of the coupling strength and the axion mass (see Eq. 3.4):

$$\sigma_{\nu N}(s = m_N^2) = \frac{1}{16\pi} \frac{g^4 s}{m_N^2 \Gamma^2} = \frac{1}{16\pi} \frac{g^4}{\Gamma^2} = \frac{1}{16\pi} \frac{g^4}{(g^2 m_N / 4\pi)^2} = \frac{\pi}{m_N^2}. \quad (4.8)$$

Calculating the interaction length at resonance would thus not make us able to set any constraints on the free parameters. Instead, on Figure 4.5 we set the limits on the interaction length at 99% of the resonance energy, since this gives a good indication of what happens near resonance, and it is nice for illustrative purposes. In reality, the energy grid of the numerical solution does not necessarily include the resonance energy or its value at 99%, so the interaction length is computed at the energy point closest to resonance. In addition, we also calculate it at $z = 4$, corresponding to the neutrino sources furthest away, since this favors the upper limit and we want to solve the propagation equation for as many fluxes as possible.

We now have all the tools for choosing the ranges of the free parameters resulting in the most fluxes being within the region where all criteria are satisfied and we can solve the

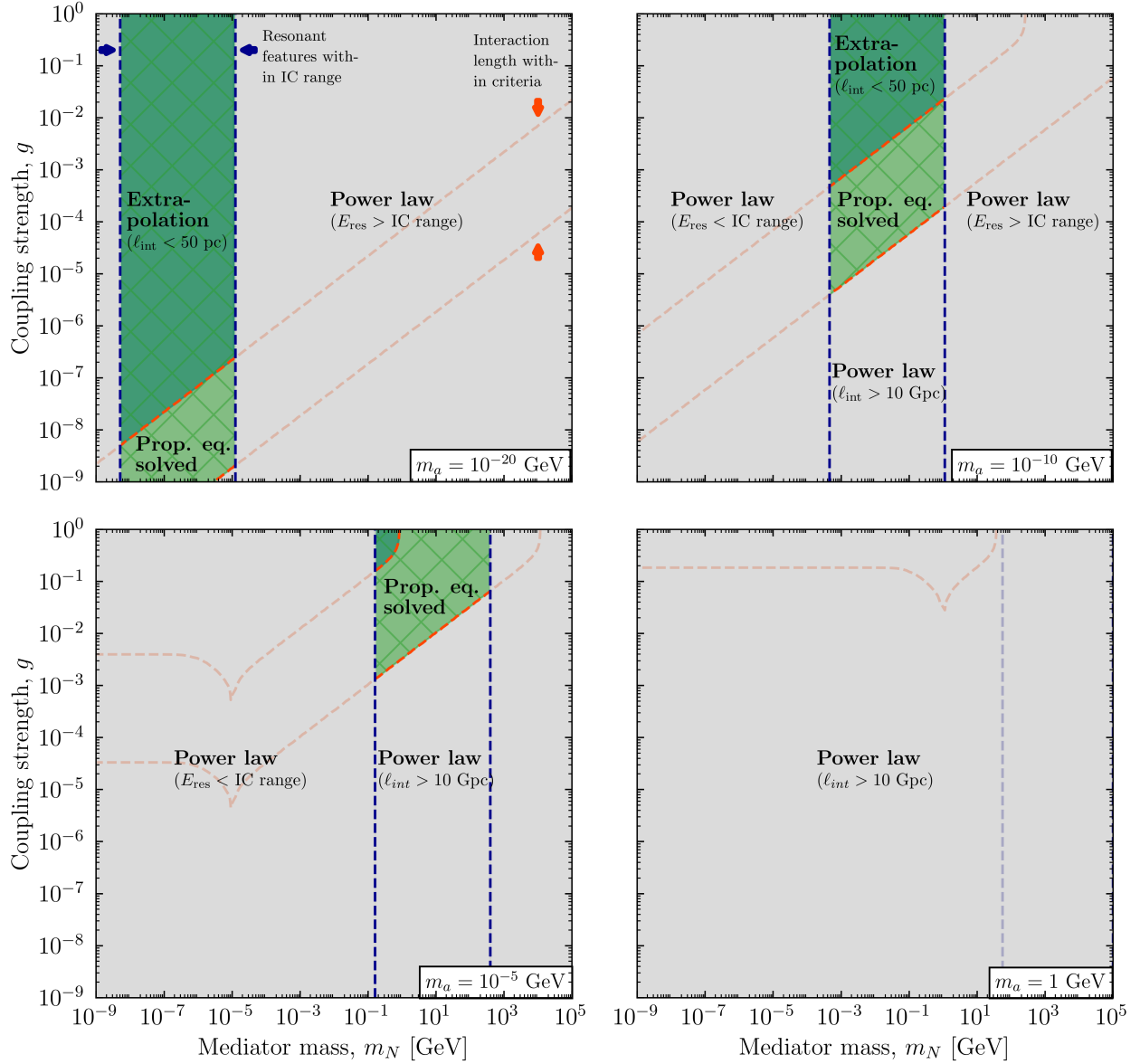


Figure 4.5: Contour plots of the interaction length evaluated at 99% of the resonance energy, based on the ranges of the mediator mass m_N and the coupling strength g for four different values of the axion mass m_a . The orange lines surround the region which is within the criteria for the interaction length: the interaction length should not exceed 10 Gpc, since then the interaction does not occur within the observable Universe; and the interaction length should not be lower than 50 pc, since then the computation time is too large. The blue lines surround the region where the resonant features are observable within IceCube (IC) range. In the green region where the orange and the blue overlap we can solve the propagation equation, since all criteria are met. The region within resonance energy and at an interaction length below 50 pc will be extrapolated. All gray regions have power laws as solutions.

propagation equation. At the same time, we want to cover broad ranges of the mediator mass, the axion mass, and the coupling strength, to be able to place leading constraints on their values. We therefore choose to vary them in a log scale. The axis ranges in Figure 4.5 match the parameter ranges that we choose for these three parameters. The reasoning of each range is elaborated in the following.

First of all, we see that as the axion mass increases, the green regions move to the right in the parameter space. At some point no part of the parameter space will satisfy the criteria. For a value of $m_a = 1$ GeV in the last plot, there will be no fluxes with characteristic features. We use this fact to determine the value of the axion mass to vary in the analysis. To be generous, we include $m_a = 1$ GeV in the axion mass range. The lower limit on the axion mass is partly determined by the contour plots; we see that for $m_a = 10^{-20}$ GeV, the green regions are still present on the plot, if the mediator mass is below 10^{-5} GeV. We could go lower in axion mass still, but we have to stop at some point. Since $m_a = 10^{-20}$ GeV is already an axion mass a lot lower than the present literature has investigated for the axion-neutrino coupling (as explained in Section 3.4.1), we choose to stop there.

Regarding the coupling strength, its value should not exceed 1, since this would make the computation of the cross section non-perturbative. In principle there is no lower limit on its value, since the interaction can be very feeble, so this choice depends on the other parameter ranges. On the other hand, we expect it to be many orders of magnitude below the upper limit, since this would be in nice correlation to the fact the axion-neutrino interaction has not been observed before. Based on Figure 4.5, we choose a lower value of $g = 10^{-9}$, which is plenty to include the green regions fully in the parameter space for almost all values within the chosen axion mass range.

The range of the mediator mass should complement the choice for the two other parameters, such that it comfortably contains the sub-range where the axion-neutrino features are observable within the IceCube energy range. As it can be seen in Figure 4.5, the lower limit should follow from the first plot with $m_a = 10^{-20}$ GeV. We choose $m_N = 10^{-9}$ GeV. The upper limit is based on the highest value of m_a chosen where the green region is still visible. This corresponds to $m_N = 10^5$ GeV.

The choice of the ranges for the remaining two parameters — the spectral index and the energy cut-off — is based on the discussion in the previous sections. The spectral index is expected to be $\gamma = 2-3$ (see Section 3.2), which is the interval we vary it in. Because the value of the cut-off energy is unknown, we vary it in the range $E_{\text{cut}} = 10^6$ GeV– 10^{10} GeV.

Table 4.1 is an overview of the parameter ranges and number of points chosen for each of the five parameters of the analysis. The parameters of the axion-neutrino interaction, m_N , m_a , and g , are varied on a fine grid since we aim to place constraints on them. The coupling strength, g , is varied on an even finer grid than the other parameters, since its value has the largest effect on the neutrino spectra. Here we choose 73 points, such that each step in the log space between each value of g is 0.125. The spectral index and the cut-off in energy both relate to the neutrino production, and although these are unknown to a certain extent, they are not of specific interest in this work. They are therefore only varied with five values each.

Based on all parameter ranges chosen, the total number of fluxes to compute is

$$n_{m_a} \cdot n_{m_N} \cdot n_g \cdot n_{E_{\text{cut}}} \cdot n_\gamma = 30 \cdot 30 \cdot 73 \cdot 5 \cdot 5 = 1,642,500 \text{ fluxes.} \quad (4.9)$$

Parameter	Range	Points
Mediator mass, $\log_{10}(m_N/\text{GeV})$	$[-9, 5]$	30
Axion mass, $\log_{10}(m_a/\text{GeV})$	$[-20, 1]$	30
Coupling strength, $\log_{10} g$	$[-9, 0]$	73
Spectral index, γ	$[2, 3]$	5
Energy cut-off, $\log_{10}(E_{\nu,\text{cut}}/\text{GeV})$	$[6, 10]$	5

Table 4.1: Table of the parameter ranges and number of points of the free parameters of the propagation equation.

4.3.2 Extrapolation

In the region of the five-dimensional parameter space where the features of the axion-neutrino interaction are observable by IceCube but the interaction length is shorter than 50 pc, we extrapolate the neutrino fluxes. This corresponds to the dark green region of Figure 4.5. The extrapolation is based on the already computed fluxes which satisfy criteria 1–3 from Section 4.3.1. The extrapolation is necessary when the run time has increased notably due to a large dip in the neutrino spectrum. This is largely determined by the coupling strength, since the cross section varies as g^4 (see Eq. (3.4)). Consequently, we choose to extrapolate fluxes to large values of g , for which our solver is too slow, based on fluxes computed with our solver for smaller values of g ; we set up a space of fluxes sorted into bundles of different coupling strengths but with the same mediator mass, axion mass, spectral index, and energy cut-off. This space consists of the fluxes for which we could solve the propagation equation. The existing fluxes are used as basis to extrapolate the fluxes with the remaining coupling strength values. As an example, if the last flux to satisfy the computation criteria for a specific set of parameter values has the coupling strength $g = 10^{-3}$, then we extrapolate the fluxes with $10^{-3} < g \leq 1$, which is the upper limit of the coupling strength range.

To extrapolate, we use a one-dimensional linear interpolator. To employ the one-dimensional extrapolation in the two-dimensional space of the neutrino spectra, we make a linear extrapolation in one direction before combining all of the extrapolated points. This means that for each energy point, the flux with a higher g is extrapolated. We use a toy model to compare the extrapolated fluxes to the “true” flux to see which extrapolation method would fit it the best. A comparison of different one-dimensional interpolators tested can be found in Appendix A.1.

Figure 4.6 illustrates the extrapolation method. In figure (a), the fluxes all have the same values of the free parameters except of the coupling strength which increases with increasing depth and width of the dip. The gray and the dark green fluxes are the fluxes that fulfill all computation criteria. The two dark green fluxes are used to extrapolate the next flux which will have a coupling strength of the next point in the coupling strength range. This is given by the light green flux. The extrapolation takes place for one energy point at a time. On the figure we have marked the points of the green fluxes where the energy is $E_\nu = 10^6$ GeV. The linear extrapolation of the fluxes at $E_\nu = 10^6$ GeV is shown in figure (b), which is in a space

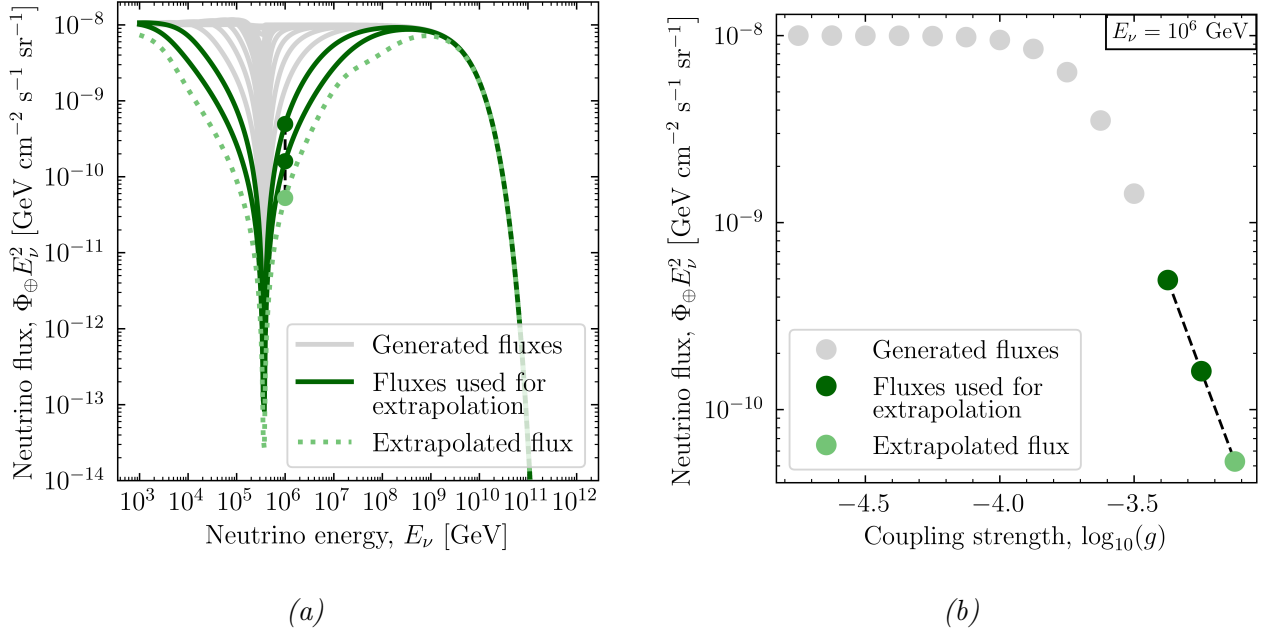


Figure 4.6: (a) An example of how the extrapolation was performed in one direction (of the flux) to create the points of the overall spectra. The fluxes in this plot all have the same values of the free parameters except of g , which is increasing as the dip gets wider. The two fluxes of the largest coupling strength to be computed numerically are used to make the linear extrapolation of the flux with the next coupling strength. The extrapolated flux was calculated one energy point at a time. (b) An example of how the extrapolation was performed in the dimension of the coupling strength for a specific neutrino energy (here $E_{\nu} = 10^6 \text{ GeV}$), corresponding to the points in (a). The flux with the lowest coupling strength is normalized to $10^{-8} \text{ GeV cm}^{-2} \text{s}^{-1} \text{sr}^{-1}$ at 1 TeV. The fluxes have the parameter values $m_N = 10^{-2.72} \text{ GeV}$, $m_a = 10^{-11.31} \text{ GeV}$, $\gamma = 2$ and $E_{\text{cut}} = 10^{10} \text{ GeV}$.

of the coupling strength. The process is repeated for the next flux in the row based on the two previous fluxes. We continue until we reach $g = 1$.

The main problem of linear extrapolation is that the flux as a function of the dimension that it is extrapolated in has to be fairly linear for the extrapolation to work properly. As it turns out, the space in coupling strength of the known solutions is not very linear. To improve the extrapolation, we need to find a way to make the space more linear. We tried many different methods to obtain this, including dividing the known solutions by each other in different ways. None of them were that successful. Ultimately, we found a way which combines the extrapolation with additional information about the flux. This information comes from an analytical solution of the propagation equation. If the regeneration term is excluded, it is possible to solve the propagation equation analytically, independent of the interaction length. This is a good approximation of the full solution since it follows the general form of the flux except of the regeneration bump.

To make the extrapolation space more linear, we divide each computed flux from the light green area of Figure 4.5 from the solution of the propagation equation with its analytical approximation. The extrapolation is performed in this space, and the extrapolated solutions

are then multiplied by their analytical solution to get back to the original space. Since the extrapolation gets worse as it is based on fluxes further and further from the original solutions, the fact that we use the analytical solution also helps with keeping some of the information in the extrapolated fluxes. The method is explained in detail in Appendix A.1. The analytical approximation of the solution of the propagation equation without regeneration is derived in Appendix A.2.

Instead of calculating an analytical approximation, it is also an option to solve the propagation equation numerically without the regeneration term. However, this is only about 10 times faster than the full numerical solution, which is not a large enough reduction in time for all solutions to have a reasonable run time. The analytical solution is very practical in this regards, since its computation time is independent of the size of the attenuation dip and only depends on the redshift step size.

5 | Detecting high-energy neutrinos

5.1 Propagation through the Earth

In Chapter 4, we solved the propagation equation that describes how high-energy neutrinos travel from their sources to the Earth with the possibility of interacting with a cosmic background of axion-like dark matter on their way. At the surface of the Earth, the flux of high-energy neutrinos is isotropic. Upon reaching the Earth, the neutrinos travel underground, from the surface of the Earth to IceCube, interacting with matter along the way. The cross section for neutrino-nucleon interactions increases with the neutrino energy. As a consequence, above ~ 10 TeV, the Earth is opaque to neutrinos [174–177].

The column depth of matter that neutrinos traverse inside the Earth depends on their incoming direction, which is quantified by the incoming zenith angle, $\cos(\theta_z)$. We distinguish between up-going neutrinos with $-1 \leq \cos(\theta_z) \lesssim 0$ and down-going neutrinos with $0 \lesssim \cos(\theta_z) \leq 1$. Up-going neutrinos travel up to the diameter of the Earth before they reach IceCube, while down-going neutrinos reach IceCube after traveling through the atmosphere and a few kilometers of ice. Broadly stated, the more neutrino-matter interactions take place, the stronger the attenuation of the flux will be. Thus, the flux of up-going neutrinos is more strongly attenuated by interactions with matter inside the Earth, compared to the flux of down-going neutrinos. Likewise, the attenuation is also stronger for neutrinos of higher energy, since the neutrino-nucleon cross section grows with energy. The interactions attenuate the flux in an energy-, direction-, and flavor-dependent manner. Below, we describe this in detail.

The neutrinos traveling through the Earth will experience deep inelastic scattering on nucleons. These scatterings are CC interactions, where the neutrino interacts with a nucleon to produce a charged lepton of the same flavor and a hadronic shower, and NC interactions, where the neutrino interacts with a nucleon to produce a neutrino of the same flavor and a hadronic shower. The interactions are described in further detail in Section 3.3.1. The energy of a neutrino after a DIS neutrino-nucleon interaction is determined by the inelasticity. An incoming neutrino of energy E_ν gives, on average, the final-state lepton a fraction $(1 - \langle y \rangle)$ of its energy, and the hadronic shower will receive the energy fraction $\langle y \rangle$, where $\langle y \rangle$ is the average inelasticity of the interaction, which can be $0 \leq y \leq 1$. At astrophysical neutrino energies of TeV-PeV, the average inelasticity is $\langle y \rangle = 0.25 - 0.30$ [174–176, 178]. This means that final-state leptons have about 70-75% of the original neutrino energy.

Generally, NC interactions dampen the flux at high energy and regenerates it at lower energies. CC interactions deplete the flux of ν_e and ν_μ by removing neutrinos. When a tau

neutrino interacts with matter by a CC interaction, the produced tauon decays within the Earth volume to produce a new tau neutrino of lower energy. We call this process *tau neutrino regeneration*. As a result, the observed neutrino spectrum will show a pile-up of tau neutrinos at lower energies compared to the other flavors. At TeV–PeV energies, ν_τ regeneration is a minor effect, but we will still account for it. The effect becomes more important at higher energies.

Another neutrino-matter interaction is the resonant production of W -bosons, also called Glashow resonance [179]. It happens when the anti-neutrino electron scatters on an electron to produce a W^- -boson by $\bar{\nu}_e + e^- \rightarrow W^-$. The interaction is resonant at a neutrino energy of

$$E_\nu = \frac{M_W - (m_e^2 + m_\nu^2)}{2m_e} \approx 6.3 \text{ PeV}, \quad (5.1)$$

where M_W is the W -boson mass, m_e is the electron mass, and m_ν is the neutrino mass. As a result, the anti-electron neutrino flux is highly attenuated near the resonance energy. On resonance, the Glashow resonance cross section is roughly 200 times larger than the neutrino-nucleon cross section. Neutrinos of other flavors also scatter off of electrons, but only elastically, and with a tiny cross section. In 2021, it was confirmed that IceCube had observed the Glashow resonance for the first time [180].

Besides the neutrino-matter interactions, other effects occur when neutrinos propagate in matter compared to vacuum. Modifications of neutrino oscillations in matter, i.e., the Mikheyev-Smirnov-Wolfenstein (MSW) effect [181,182], are due to electron neutrinos experiencing coherent forward scattering from the electrons they encounter in the Earth. Coherent means that the scattering is the same for all neutrinos traveling along the same path – their oscillations evolve identically and they will be in the same state upon detection. In the high-energy regime relevant for axion-neutrino interactions, the matter effects will however not play a significant role [183].

Figure 5.1 shows the effects of Earth attenuation, tau regeneration, and Glashow resonance on the neutrino spectrum of each neutrino flavor for illustrative neutrino fluxes at the detector, computed with and without the neutrino-axion interactions, and for different neutrino arrival directions. Down-going neutrinos have almost no interaction with matter, so this neutrino flux is similar to that on the surface of the Earth. Horizontal neutrinos propagate through a tiny part of the Earth, so there is only a small difference between the neutrino flavors. For downgoing and horizontal neutrinos, the characteristic features induced by neutrino-axion interactions are clearly visible, and undistorted by the propagation inside the Earth.

For up-going neutrinos, the effects of interactions inside Earth are apparent. Firstly, the flux is attenuated at energies above 10 TeV, compared to the down-going and horizontal fluxes. Secondly, the regeneration of tau neutrinos and anti-tau neutrinos appears distinctly above 100 TeV, where the ν_τ flux is higher than the ν_e and ν_μ fluxes.

For a directly up-going flux of $\cos(\theta_z) = -1$, the flux is attenuated the most. The attenuation is so strong at PeV energies that the Glashow resonance is difficult to see unless the flux is measured at a very high precision. The dip from the axion-neutrino interaction becomes more distorted the more of the Earth that the neutrinos pass through. The distortion means that the dip becomes shallower and wider, compared to how it looks pre-attenuation.

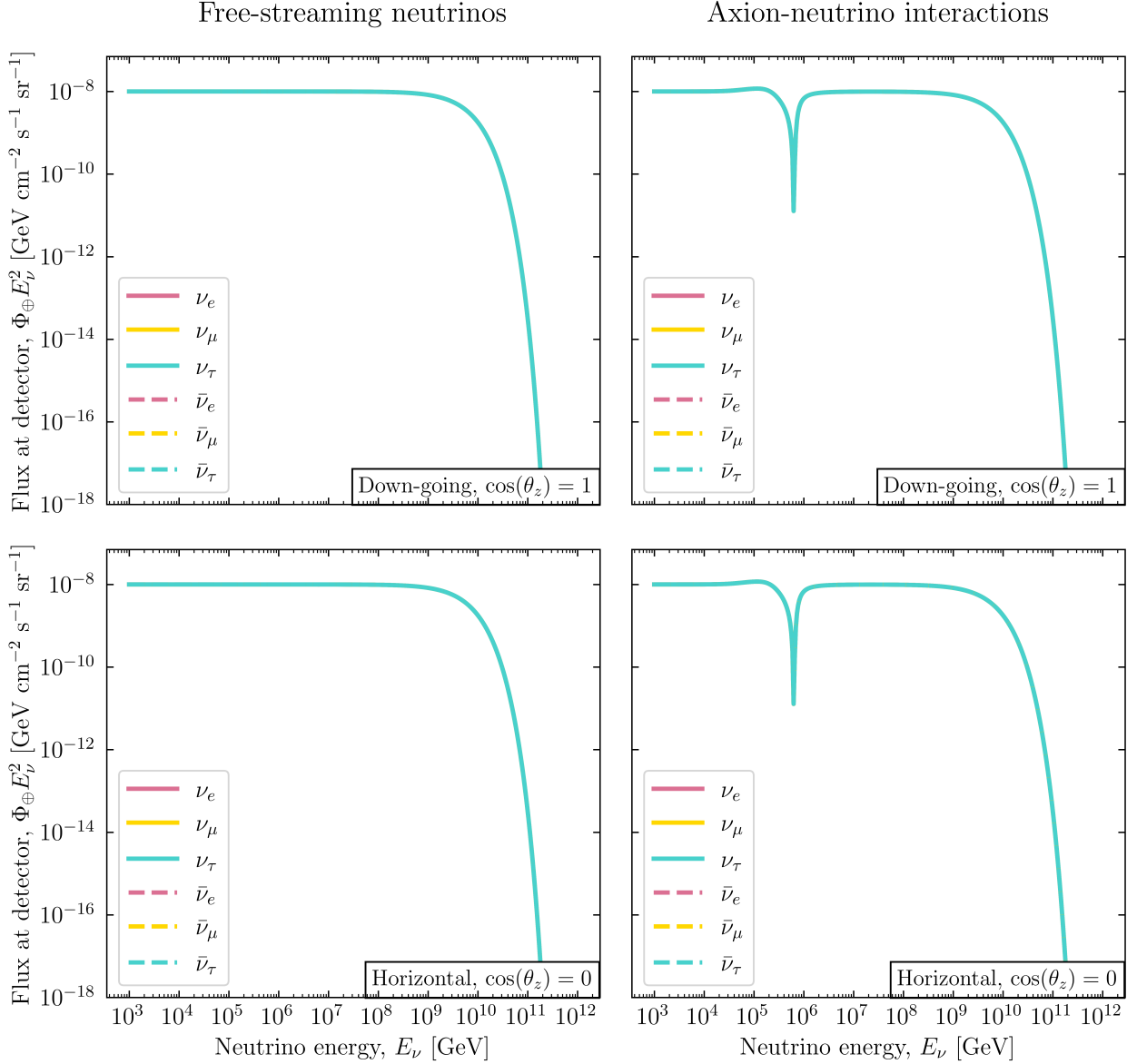


Figure 5.1: Example of the fluxes as neutrinos of each flavor reach the detector for a down-going direction at $\cos(\theta_z) = 1$ (first row) and horizontal direction at $\cos(\theta_z) = 0$ (second row). Left column: an example power-law flux, which is the result of neutrinos free-streaming before they reach the Earth. Right column: a flux with an axion-neutrino interaction. Fluxes are normalized to $10^{-8} \text{ GeV cm}^{-2} \text{ s}^{-1} \text{ sr}^{-1}$ at 1 TeV. The fluxes were computed using the parameter values $m_a = 10^{-2.24} \text{ GeV}$, $m_N = 10^{-10.59} \text{ GeV}$, $\gamma = 2$ and $E_{\text{cut}} = 10^{10} \text{ GeV}$. (Continues on next page.)

The reason is that neutrinos that had energies originally above the dip have been regenerated to energies around the dip, so they “fill up” the deficit. Since the neutrinos become more attenuated the higher their energy, an axion-neutrino interaction with high resonance energy will be more distorted than that with a lower resonance energy.

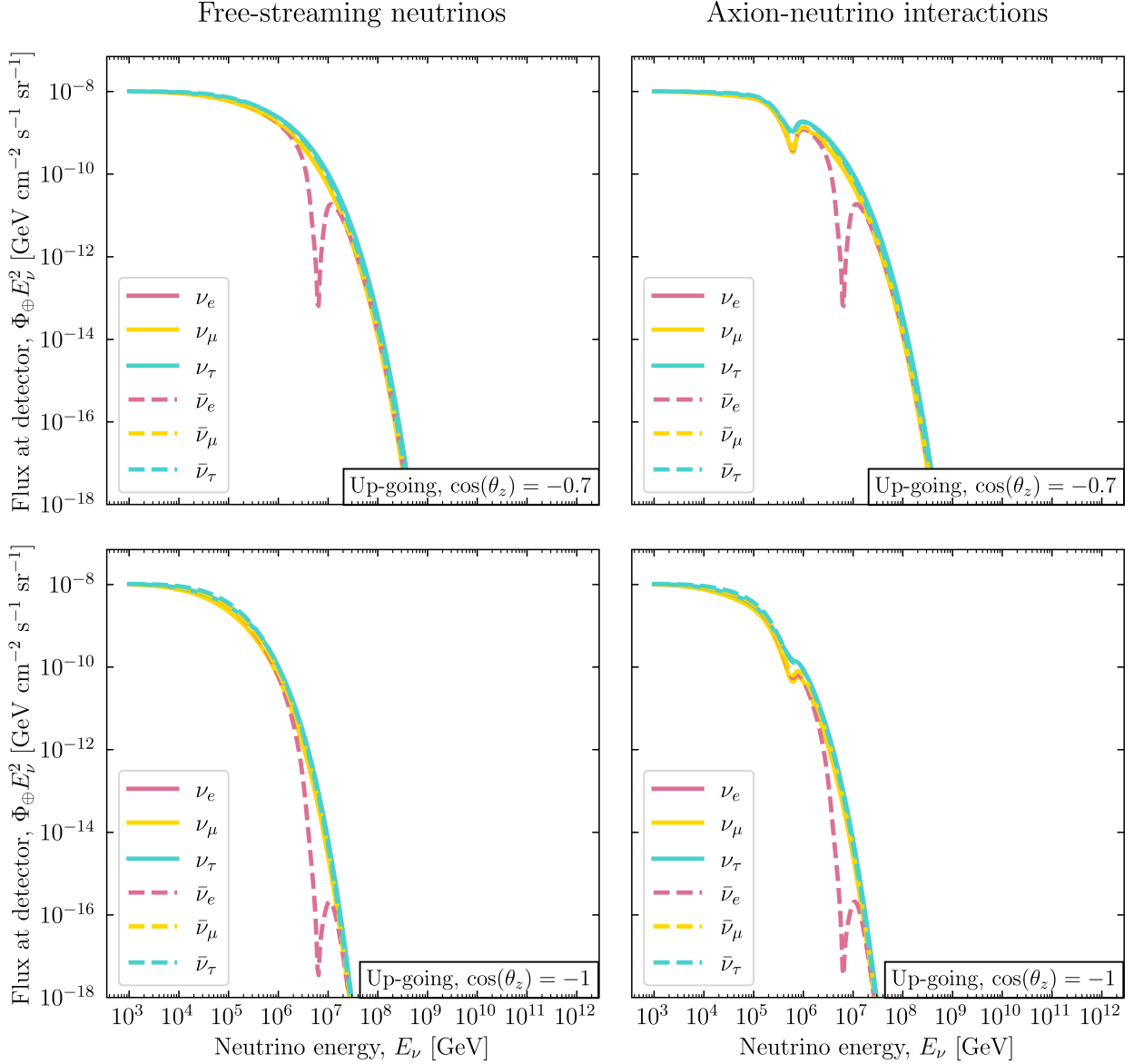


Figure 5.1: (Continued from previous page.) Example of the fluxes as neutrinos of each flavor reach the detector for an up-going direction at $\cos(\theta_z) = -0.7$ (first row) and up-going direction at $\cos(\theta_z) = -1$ (second row). Left column: an example power-law flux, which is the result of neutrinos free-streaming before they reach the Earth. Right column: a flux with an axion-neutrino interaction. Fluxes are normalized to 10^{-8} GeV cm⁻² s⁻¹ sr⁻¹ at 1 TeV. The fluxes were computed using the parameter values $m_a = 10^{-2.24}$ GeV, $m_N = 10^{-10.59}$ GeV, $\gamma = 2$ and $E_{\text{cut}} = 10^{10}$ GeV.

The fluxes shown in Figure 5.1 come from simulations made using nuSQuIDS (Neutrino Simple Quantum Integro-Differential Solver) [184]. nuSQuIDS calculates the impact of high-energy neutrinos interacting with the matter of the Earth by solving their propagation equation, using state-of-the-art oscillation calculations. The computation of neutrino propa-

Category	$E_{\text{dep}} < 60 \text{ TeV}$	$E_{\text{dep}} > 60 \text{ TeV}$	Total
Total Events	42	60	102
Up	19	21	40
Down	23	39	62
Cascade	30	41	71
Track	10	17	27
Double Cascade	2	2	4

Table 5.1: Summary of the High Energy Starting Events (HESE) data set collected by IceCube after 7.5 years of observation. We use the events above 60 TeV in our analysis. From [11].

gation through the Earth is already included in the event rate calculations on which we base our analysis, elaborated in Section 5.3. The plots shown in this section based on nuSQuIDS are thus only used for illustrative purposes. The results based on nuSQuIDS and on the HESE Monte Carlo data assume the Preliminary Reference Earth Model when describing the matter density inside Earth. This is built from seismological data, which models the density of Earth in radial shells that increase in density towards the core [185].

5.2 IceCube High Energy Starting Events and background

The data set that we use is the High Energy Starting Events (HESE) collected during 7.5 years (2635 days) of the live time of the IceCube detector. The HESE data consists of 102 detected astrophysical neutrino events with an energy above 10 TeV. They all come from neutrino-nucleon interactions that took place inside the detector, which is why they are called starting events, as opposed to events where the neutrino interaction happen outside the detector volume.

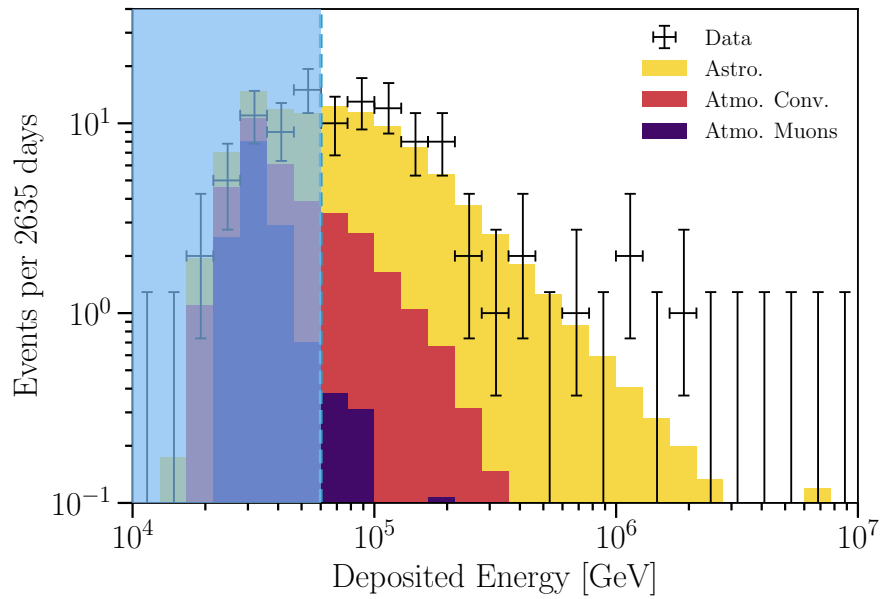
Table 5.1 shows a summary of the HESE data set that we use. The neutrino events are divided into up- and down-going neutrinos and the three event types: cascades, tracks, and double bangs. The events are further differentiated between events with deposited energies below 60 TeV and above 60 TeV due to the atmospheric background. Deposited energy is the energy of the neutrino-induced shower that is reconstructed from the photons collected by the DOMs.

There is an overwhelming flux of atmospheric muons and neutrinos produced by cosmic-ray interactions in the atmosphere, which constitutes a large background for the astrophysical neutrino detection. This background falls steeply with energy [158] and is sub-dominant to astrophysical neutrinos at high energies. Thus, to reduce the atmospheric contamination and enhance the contribution of astrophysical neutrinos, in our analysis we use only HESE events with energies above 60 TeV, the same threshold value used by the IceCube Collaboration. The atmospheric neutrinos come from pion and kaon decay, also called the conventional atmospheric neutrino flux. Another type of atmospheric neutrino flux is the prompt flux

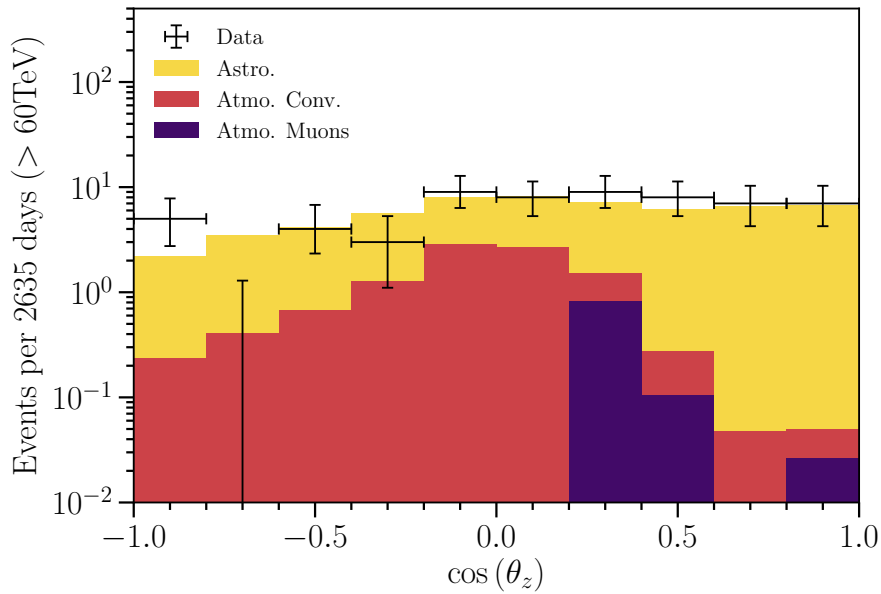
from charmed meson decay [186]. However, this is not yet observed, and we thus ignore it in our analysis.

There are two advantages of using high-energy starting events. Firstly, it makes it possible to do a full energy reconstruction, since showers are contained and tracks deposit a large part of their energy inside the detector. Secondly, it reduces the background of atmospheric neutrinos significantly. To reduce the contamination of atmospheric neutrinos in the HESE sample, the outer layers of the detector are used as veto layers. They include about 90 m of DOMs around the detector sides, 90 m from the top and 10 m from the bottom. For a visual overview of the veto layer placements, we refer to Figure II.1 in Ref. [11]. The atmospheric neutrinos propagate alongside accompanying muons from the air shower where they are produced. The role of DOMs in the veto layer is to flag atmospheric neutrinos by detecting the passage of the atmospheric muons co-created with them, since these leave tracks in the detector. If a neutrino event is detected by triggering DOMs in the fiducial volume, but at the same time DOMs in the veto region along the same incoming direction are triggered, the neutrino event is not categorized as a starting event. The atmospheric muons can not be excluded by the veto layer, since its thickness is insignificant compared to the muon decay time. However, an estimate of the muon background is based on the muon events in the veto region.

Figure 5.2 shows the 7.5-year HESE sample, together with the best-fit contribution of astrophysical neutrinos, atmospheric neutrinos, and atmospheric muons, from Ref. [11]. The events are summed over flavor. Fig. 5.2 (a) is the event rate as a function of deposited energy, summed over direction. The blue region is excluded due to the high background, compared to the astrophysical neutrino signal. The bin with a low number of neutrino events at about 7 PeV is from the Glashow resonance. Even though up-going anti-electron neutrinos have been absorbed at this resonance, the down-going anti-electron neutrinos have only traveled through few kilometers of the ice, so they are not attenuated yet and will interact resonantly in the detector. Fig. 5.2 (b) shows the angular dependence of the event rates for energies above 60 TeV. The background of atmospheric muons is highly dependent on the zenith angle and is only a background for down-going neutrinos because they will not survive to propagate longer distances. The figure also shows that the HESE selection eliminates a significant part of the atmospheric neutrino background for down-going neutrinos.



(a)



(b)

Figure 5.2: Event rates of high-energy neutrino events from the HESE data (crosses) compared to a stacked histogram of the expected MC events from best-fit values divided into astrophysical neutrino flux, conventional neutrino flux and atmospheric muon flux. (a) shows the event rates as a function of deposited energy. The blue region is a cut-off placed at 60 TeV due to the larger background. (b) shows the event rates as a function of the reconstructed neutrino cosine zenith angle. Reproduced from [11].

5.3 Event rates

5.3.1 Event rate derivation

In our analysis, we compare the HESE event rates predicted for high-energy neutrino fluxes computed assuming that there are neutrino-axion interactions, versus the observed 7.5-year HESE data set. We compute the rate of cascades, tracks, and double cascades separately, since they are distinguished from each other in the HESE data set.

In a high-energy starting event, the neutrino-nucleon interaction takes place inside the IceCube detector. This means that the full shower caused by the final-state particles will be contained. In a neutral-current interaction, the shower is initiated by the final-state hadrons; the final-state neutrino escapes without interacting. The deposited energy E_{dep} in the DOMs is thus the shower energy E_{sh} given by $E_{\text{dep}} = E_{\text{sh}} = \langle y \rangle E_\nu$, where $\langle y \rangle$ is the average inelasticity of $\langle y \rangle = 0.25 - 0.30$. In a charged-current interaction where the outgoing lepton produces a shower in addition to the hadronic shower, $E_{\text{dep}} = E_{\text{sh}} = E_\nu$. For a CC ν_μ interaction, the final-state muon creates a track that is mostly contained inside the detector, so we can approximate $E_{\text{dep}} = E_{\text{sh}} + E_{\text{track}} \approx E_\nu$.

To compute HESE event rates, we use the publicly available sample of Monte Carlo events and analysis tools provided by the IceCube Collaboration; we describe it in Section 5.3.2. The diffuse neutrino events initiated by neutrinos with energies between E_ν^{min} and E_ν^{max} , recorded within a detector live time T , is

$$N_\nu = 2\pi T N_N \int_{E_\nu^{\text{min}}}^{E_\nu^{\text{max}}} dE_\nu \int_{-1}^{+1} d\cos\theta_z \Phi_\nu A_{\text{eff}}(E_\nu, \theta_z), \quad (5.2)$$

where N_N is the number of target nucleons in the detector, and the effective area, A_{eff} , represents the energy- and direction-dependent response of the detector. In a first approximation, it can be computed as

$$A_{\text{eff}}(E_\nu, \theta_z) = e^{-L(\theta_z)/L_{\nu N}(E_\nu, \theta_z)} \sigma_{\nu N}(E_\nu), \quad (5.3)$$

where $L(\theta_z)$ is the length traveled by a neutrino coming from direction θ_z , $L_{\nu N} \equiv (\sigma_{\nu N} n_N)^{-1}$ is the attenuation length due to νN interactions, n_N is the number density of nucleons encountered along this direction, and $\sigma_{\nu N}$ is the neutrino-nucleon cross section.

5.3.2 HESE Monte Carlo simulations

In our analysis, we compute HESE event rates for different diffuse high-energy neutrino fluxes by repurposing the large set of Monte Carlo (MC) HESE events made publicly available [187] in association with Ref. [11]. This MC set contains 102 HESE events simulated using a nuanced description of the detector response, including the energy resolution, and of the background of atmospheric neutrinos and muons.

The MC data set, as provided by the IceCube Collaboration, was produced adopting a pure power-law all-flavor flux for the high-energy neutrinos, i.e.,

$$\frac{d\Phi_{\text{ref}}(E_\nu)}{dE_\nu} = \phi_{\text{astro}} \left(\frac{E_\nu}{100 \text{ TeV}} \right)^{-\gamma_{\text{astro}}} \cdot 10^{-18} \text{ GeV}^{-1} \text{ cm}^{-2} \text{ s}^{-1} \text{ sr}^{-1}, \quad (5.4)$$

where $\gamma_{\text{astro}} = 2.87$ is the spectral index of the diffuse astrophysical neutrino flux, E_ν is the neutrino energy, and $\phi_{\text{astro}} = 6.36$ is the all-flavor normalization at 100 TeV. These are the best-fit values obtained in the 7.5-year HESE analysis [11].

Given a different neutrino flux, computed as described in Chapter 4, we can transform the MC data set to compute the corresponding expected HESE event rate. Each of the events in the MC data set is provided together with a statistical weight that, broadly stated, represents its contribution to the data set, and is energy-, direction-, flavor-, and topology-dependency. We transform the MC event rates computed using the reference flux, Eq. (5.4), to the event rates computed with an arbitrary flux Φ , by “reweighing” the events. In practice, this means that, for the i -th MC event, with energy $E_{\nu,i}$ and original weight w_i , we compute a new weight

$$w'_i = w_i \frac{\Phi(E_{\nu,i})}{\Phi_{\text{ref}}(E_{\nu,i})} . \quad (5.5)$$

For details about the weights and reweighing, see Ref. [11, 188].

Figure 5.3 shows the all-flavor contained neutrino event rates summed over angle and flavor for a power-law flux in the background and a flux with an axion-neutrino interaction in front. The event types of cascades, tracks, and double cascades are stacked to give the total event rate. The resonance energy of the axion-neutrino interaction is at $6.3 \cdot 10^5$ GeV, which can be seen on each figure as a slight deficit in events compared to the background. The event rates decrease with energy except at about 5 PeV where the Glashow resonance causes the event rates to slightly increase. Figure 5.3 (a) is for a spectral index of $\gamma = 2$ while (b) is for a spectral index of $\gamma = 3$. A larger value of γ causes the event rates to decrease more with energy. Figure 5.3 (b) is comparable to the HESE event rate in Figure 5.2 where $\gamma = 2.87$.

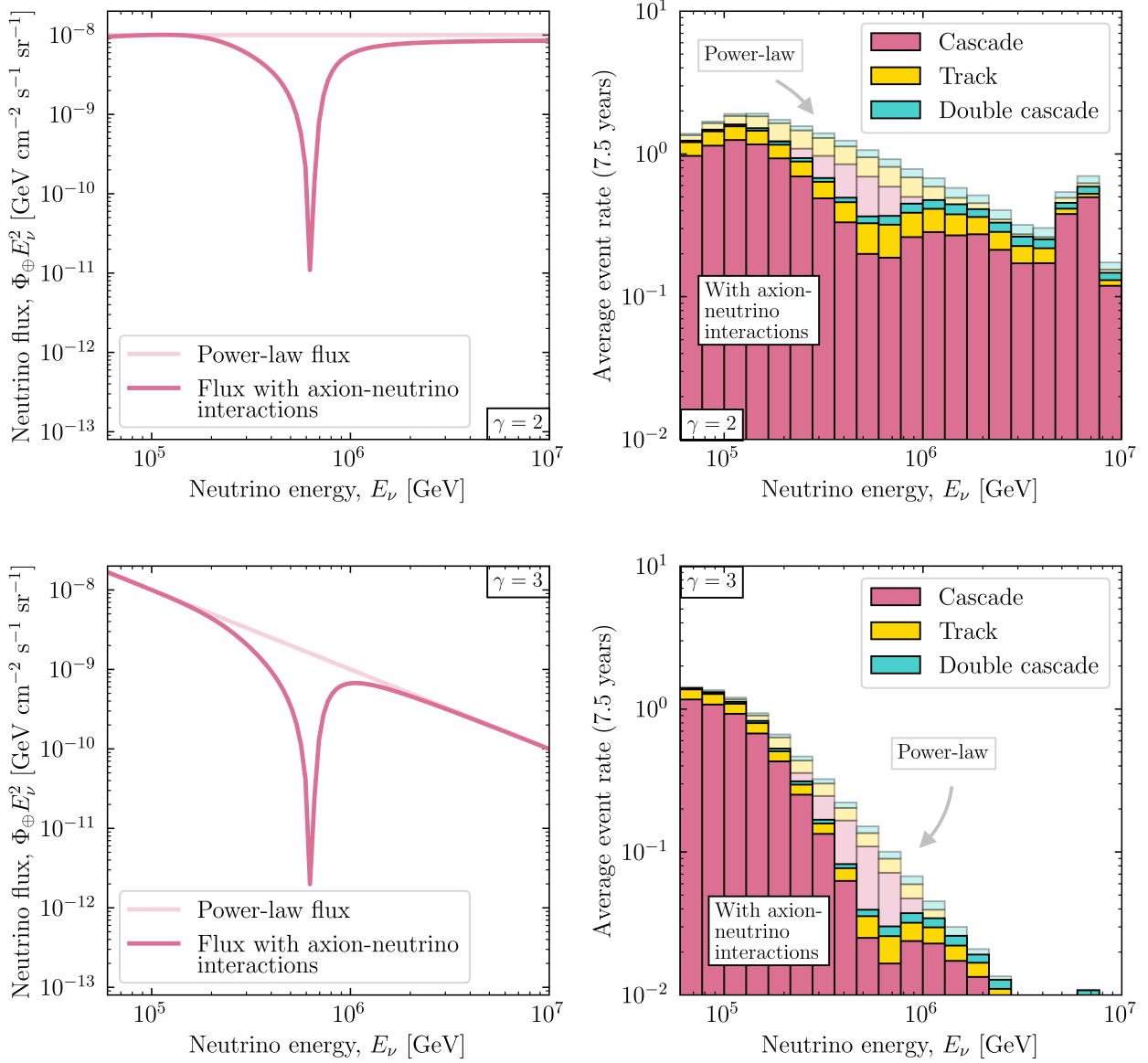


Figure 5.3: Left column: neutrino fluxes at the surface of the Earth for an example power-law flux and a flux with axion-neutrino interactions. The fluxes in the first row have the same parameter values as the flux at the detector in Figure 5.1 with $m_a = 10^{-2.24}$ GeV, $m_N = 10^{-10.59}$ GeV, $\gamma = 2$ and $E_{\text{cut}} = 10^{10}$ GeV. The fluxes in the second row are of the same parameter values except with a spectral index of $\gamma = 3$. Fluxes are normalized to $10^{-8} \text{ GeV cm}^{-2} \text{s}^{-1} \text{sr}^{-1}$ at 1 TeV. Right column: example event rates based on the example fluxes with a detector livetime of 7.5 years (2635 days) showing a stacked histogram of cascades, tracks, and double cascades. The transparent background shows a histogram of event rates based on an example power-law flux of free-streaming neutrinos, and the foreground shows a histogram based on an example flux of an axion-neutrino interaction with resonance energy at $6.3 \cdot 10^5$ GeV (inside the bin range).

6 | Statistical analysis

To compare our event-rate predictions to the 7.5-year HESE data set, we adopt a Bayesian statistical approach. We denote the HESE data as the observed neutrino events, $\{N_{\text{obs}}\}_{i=1}^{N_{\text{obs}}}$, in the i -th bin of deposited energy. This is compared to the theoretically predicted neutrino events from the solution of the propagation equation, $\{N_{\text{th}}\}_{i=1}^{N_{\text{th}}}$. The bin ranges come from the HESE analysis, as shown in Figure 5.2. There are 21 bins in the range above 60 TeV to the upper IceCube range of 10 PeV.

The free parameters that we vary are the all-flavor normalization of the astrophysical neutrino flux at 100 TeV, Φ_0^{ast} , and the background of atmospheric neutrinos and atmospheric muons, $\Phi_0^{\text{atm},\nu}$ and $\Phi_0^{\text{atm},\mu}$; the parameters of the axion-neutrino interaction, the mediator mass m_N , the axion mass m_a , and the coupling strength g ; and the parameters of the astrophysical neutrino production, the spectral index γ , and the energy cut-off E_{cut} . We denote the free parameters by $\bar{\theta} = (\Phi_0^{\text{ast}}, \Phi_0^{\text{atm},\nu}, \Phi_0^{\text{atm},\mu}, m_N, m_a, g, \gamma, E_{\text{cut}})$. In the particular case of free-streaming neutrinos, the flux depends on only a subset of these parameters, $\bar{\eta} = (\Phi_0^{\text{ast}}, \Phi_0^{\text{atm},\nu}, \Phi_0^{\text{atm},\mu}, \gamma, E_{\text{cut}})$.

To compare the observed neutrino events from the IceCube HESE data to the computed simulations of the axion-neutrino interactions, we make use of a test statistic. This compares the number of neutrinos in each bin between the two and quantifies how well they agree. We use a Poisson likelihood to account for random fluctuations in the event rate. The likelihood function for each bin i is

$$\mathcal{L}_i(\bar{\theta}) = \frac{N_{\text{th},i}(\bar{\theta})^{N_{\text{obs},i}} \exp(-N_{\text{th},i}(\bar{\theta}))}{N_{\text{th},i}!}. \quad (6.1)$$

The combined likelihood is the product of the likelihood of the individual bins. For each event topology t , where $t = \{\text{cascade}, \text{track}, \text{doubletrack}\}$, this is

$$\mathcal{L}^t(\bar{\theta}) = \prod_{i=0}^{N_{\text{bins}}} \mathcal{L}_i^t(\bar{\theta}). \quad (6.2)$$

Collectively, for all event types, we get

$$\mathcal{L}(\bar{\theta}) = \mathcal{L}^{\text{cascade}}(\bar{\theta}) \cdot \mathcal{L}^{\text{track}}(\bar{\theta}) \cdot \mathcal{L}^{\text{double}}(\bar{\theta}). \quad (6.3)$$

We use the likelihood to find the posterior \mathcal{P} , which is given by

$$\mathcal{P}(\bar{\theta}) = \frac{\mathcal{L}(\bar{\theta})\pi(\bar{\theta})}{\int \mathcal{L}(\bar{\theta})\pi(\bar{\theta})d\bar{\theta}}, \quad (6.4)$$

where π is the prior for each free parameter, which we describe below. For the case of free-streaming neutrinos, we have equations similar to Eq. (6.2-6.4) where $\bar{\theta}$ is replaced by $\bar{\eta}$.

We account for the background of atmospheric neutrinos and atmospheric muons in the same way as the IceCube HESE analysis in Ref. [11]. In our analysis, we only consider the conventional flux of atmospheric neutrinos, from the decay of pions and kaons, and not the prompt flux of atmospheric neutrinos, from the decay of charmed mesons, which so far remains undetected [11]. The atmospheric neutrino flux is computed using the Hillas-Gaisser H3a model [189–191] for the parent cosmic-rays spectrum and mass composition, and the SYBILL 2.3C hadronic interaction model [192]. The atmospheric muon flux corresponds to the flux of single muons that evade the HESE veto, and is calculated using CORSIKA [193] to simulate cosmic ray-induced air showers, assuming the Hillas-Gaisser H4a [191] model of cosmic-ray spectra and the SYBILL 2.1 hadronic model [194]. The uncertainties in the prediction of the event rates induced by atmospheric neutrinos and muons are represented by the normalization of their respective fluxes, $\Phi_0^{\text{atm},\nu}$, and $\Phi_0^{\text{atm},\mu}$, which we vary around their theoretical predictions of 1, as part of our likelihood analysis.

Thus, in each energy bin, the total number of predicted events is the sum of events induced by astrophysical neutrinos, $N_{\nu,i}^{\text{ast}}$, computed as described in Chapter 2, plus the background of events induced by atmospheric neutrinos, $N_{\nu,i}^{\text{atm}}$, and atmospheric muons, $N_{\mu,i}^{\text{atm}}$. For the free-streaming neutrinos and the neutrinos interacting with axions, we get, respectively

$$N_{\text{th},i}(\bar{\theta}) = N_{\nu,i}^{\text{ast}}(\Phi_0^{\text{ast}}, m_N, m_a, g, \gamma, E_{\text{cut}}) + N_{\nu,i}^{\text{atm}}(\Phi_0^{\text{atm},\nu}) + N_{\mu,i}^{\text{atm}}(\Phi_0^{\text{atm},\mu}) \quad (6.5)$$

$$N_{\text{th},i}(\bar{\eta}) = N_{\nu,i}^{\text{ast}}(\Phi_0^{\text{ast}}, \gamma, E_{\text{cut}}) + N_{\nu,i}^{\text{atm}}(\Phi_0^{\text{atm},\nu}) + N_{\mu,i}^{\text{atm}}(\Phi_0^{\text{atm},\mu}). \quad (6.6)$$

Table 6.1 contains the individual priors of the free parameters. The prior is a sum of all prior knowledge of all of the free parameters:

$$\pi(\bar{\theta}) = \pi(\Phi_0^{\text{ast}})\pi(\Phi_0^{\text{atm},\nu})\pi(\Phi_0^{\text{atm},\mu})\pi(m_N)\pi(m_a)\pi(g)\pi(\gamma)\pi(E_{\text{cut}}) \quad (6.7)$$

$$\pi(\bar{\eta}) = \pi(\Phi_0^{\text{ast}})\pi(\Phi_0^{\text{atm},\nu})\pi(\Phi_0^{\text{atm},\mu})\pi(\gamma)\pi(E_{\text{cut}}). \quad (6.8)$$

The priors on the parameters that are varied in the solution of the propagation equation (parameters of the axion-neutrino interaction and neutrino production) are all flat with a distribution between the chosen parameter ranges. The priors on the normalization are equal to those in the HESE analysis.

We maximize the posterior of Eq. (6.4) using **UltraNest**, an efficient Bayesian nested-importance sampler [195–197]. It computes the best-fit values and the marginal likelihood. The posterior probability distributions of both the SM and BSM fluxes are shown in Appendix B. Without axion-neutrino interaction, the spectral index best-fit value is $\gamma = 2.85_{-0.11}^{+0.18}$, compatible with the spectral index of the IceCube analysis of $\gamma = 2.87_{-0.19}^{+0.20}$ [11].

The marginal likelihood or evidence is given in the denominator of Eq. (6.4). We find its value in the case for the beyond the Standard Model physics (BSM) of axion-neutrino interactions and for the standard (std) free-streaming case with just a power-law flux:

$$\mathcal{Z}_{\text{BSM}} = \int \mathcal{L}(\bar{\theta})\pi(\bar{\theta})d\bar{\theta}, \quad (6.9)$$

Parameter	Prior
Mediator mass, $\log_{10}(m_N/\text{GeV})$	Flat in $[-9, 5]$
Axion mass, $\log_{10}(m_a/\text{GeV})$	Flat in $[-20, 1]$
Coupling strength, $\log_{10} g$	Flat in $[-9, 0]$
Spectral index, γ	Flat in $[2, 3]$
Energy cut-off, $\log_{10}(E_{\nu,\text{cut}}/\text{GeV})$	Flat in $[6, 10]$
Astrophysical norm., Φ_0^{ast}	Flat in $[0, 1000]$
Atm. neutrino norm., $\Phi_0^{\text{atm},\nu}$	Gaussian centered at 1, with width 0.5
Atm. muon norm., $\Phi_0^{\text{atm},\mu}$	Gaussian centered at 1, with width 0.4

Table 6.1: Priors of the free parameters of the propagation equation and the normalization.

Bayes factor, \mathcal{B}	Strength of evidence
$\mathcal{B} < 1$	Null hypothesis accepted
$1 < \mathcal{B} < 10^{1/2}$	Barely worth mentioning
$10^{1/2} < \mathcal{B} < 10^1$	Evidence substantial
$10^1 < \mathcal{B} < 10^{3/2}$	Evidence strong
$10^{3/2} < \mathcal{B} < 10^2$	Evidence very strong
$10^2 < \mathcal{B}$	Evidence decisive

Table 6.2: Jeffreys' table. From [198].

$$\mathcal{Z}_{\text{std}} = \int \mathcal{L}(\bar{\eta}) \pi(\bar{\eta}) d\bar{\eta}. \quad (6.10)$$

The evidence of the standard case and the BSM physics are compared using the Bayes factor, given by

$$\mathcal{B} = \frac{\mathcal{Z}_{\text{BSM}}}{\mathcal{Z}_{\text{std}}}. \quad (6.11)$$

The higher the value of \mathcal{B} , the stronger the preference for an explanation of the HESE data that involves new physics over one that does not.

Table 6.2 shows Jeffreys' table which quantifies the preference between the null hypothesis of the free-streaming neutrinos and the alternative hypothesis of axion-neutrino interactions [198]. If $\mathcal{B} \gg 1$, the new physics are preferred.

7 | Results

Table 7.1 shows the best-fit values of the free parameters for a flux of high-energy astrophysical neutrinos computed with axion-neutrino interactions, and their allowed ranges at a 68% confidence level (C.L.) and a 95% C.L. The coupling strength is hardly constrained: at a 1σ level, values down to $g = 10^{-7.2}$ are allowed; for such small values, there is no observable axion-neutrino features on the high-energy neutrino flux. Hence, there is no statistical significance for axion-neutrino interactions in the HESE data.

Figure 7.1 shows the flux of free-streaming high-energy neutrinos and of high-energy neutrinos computed with axion-neutrino interactions, calculated with the best-fit parameters from Table 7.1. The latter shows no evidence for features like dips and bumps.

Figure 7.2 shows the two-dimensional marginalized contours of the axion-neutrino parameters. For all of them, the 1σ contour level spans most of the landscape. This underlines that the evidence for axion-neutrino interactions is non-existent.

The fit in the BSM case yields an evidence of $\ln(\mathcal{Z}_{\text{BSM}}) = 5.7010$. The fit in the SM case yields an evidence of $\ln(\mathcal{Z}_{\text{std}}) = 5.7406$. The Bayes factor is thus

$$\mathcal{B} = 0.9611, \tag{7.1}$$

which, according to Jeffreys' scale (Table 6.2), means that the null hypothesis is accepted, and there is no evidence of axion-neutrino interactions.

Parameter	68% C.L.	95% C.L.
Mediator mass, $\log_{10}(m_N/\text{GeV})$	$-1.8^{+4.8}_{-4.1}$	$-1.8^{+6.1}_{-6.5}$
Axion mass, $\log_{10}(m_a/\text{GeV})$	-9.2 ± 6.0	$-9.2^{+9.2}_{-9.7}$
Coupling strength, $\log_{10} g$	-4.6 ± 2.6	$-4.6^{+4.1}_{-4.0}$
Spectral index, γ	$2.77^{+0.26}_{-0.11}$	$2.77^{+0.32}_{-0.29}$
Energy cut-off, $\log_{10}(E_{\text{cut}}/\text{GeV})$	$8.0^{+1.1}_{-1.3}$	$8.0^{+1.8}_{-1.7}$
Astrophysical norm., Φ_0^{ast}	$5.4^{+1.0}_{-1.2}$	$5.4^{+1.8}_{-1.8}$
Atm. neutrino norm., $\Phi_0^{\text{atm},\nu}$	0.99 ± 0.45	$0.99^{+0.74}_{-0.74}$
Atm. muon norm., $\Phi_0^{\text{atm},\mu}$	1.02 ± 0.38	$1.02^{+0.63}_{-0.62}$

Table 7.1: Best-fit values and allowed parameter ranges of the free parameters.

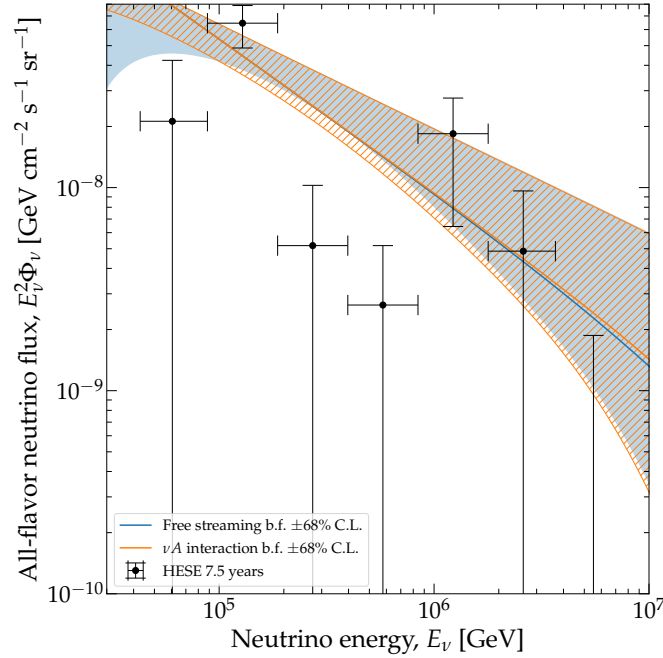


Figure 7.1: The best-fit flux of free-streaming neutrinos (blue) and the best-fit flux of neutrinos interacting with axions. The shaded regions show the 68% C.L.

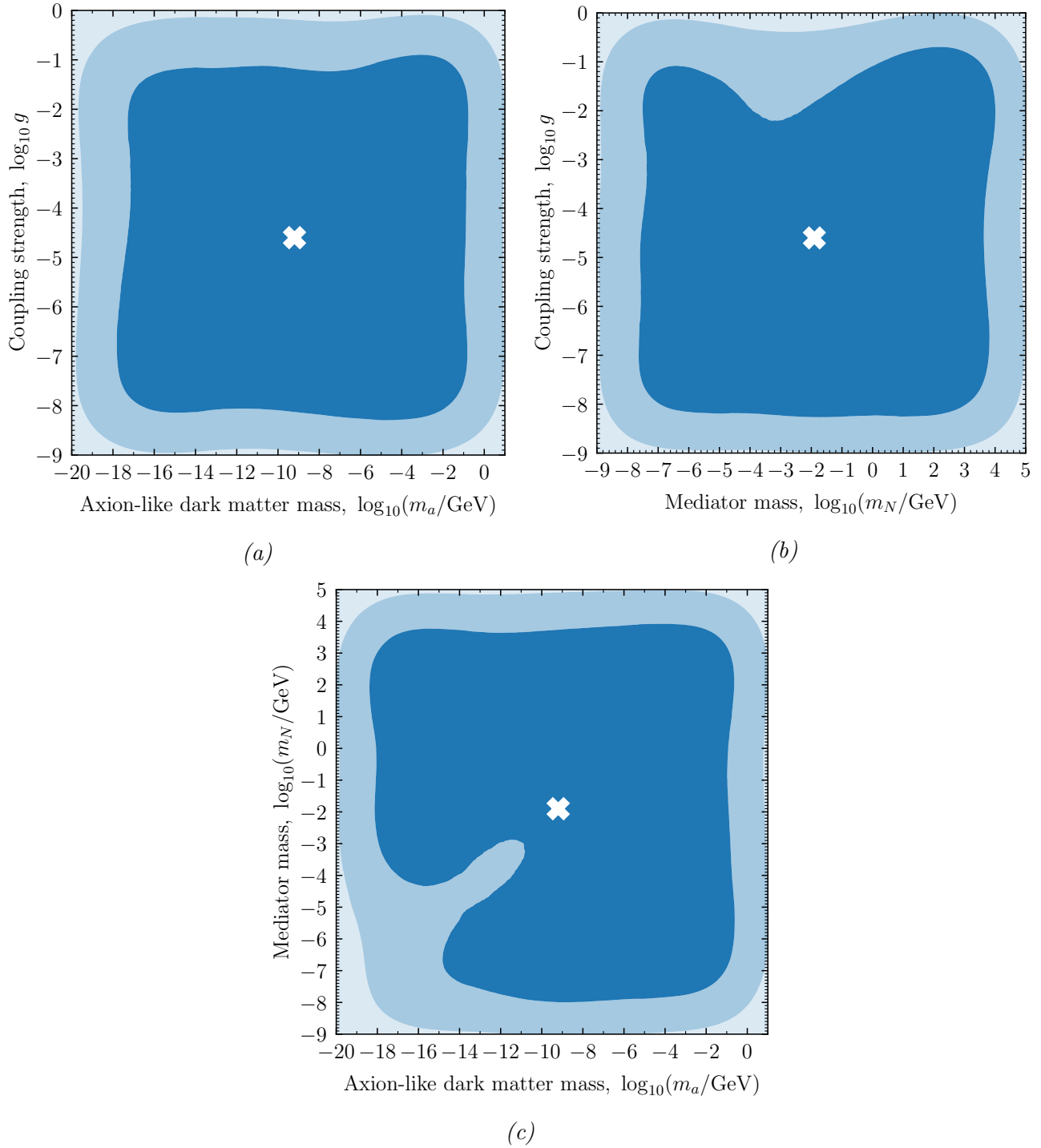


Figure 7.2: Two-dimensional marginalized contours of (a) the axion-like dark matter mass and the coupling strength, (b) the mediator mass and the coupling strength, and (c) the axion-like dark matter mass and the mediator mass. Best-fit values are marked by white crosses. Darkest blue regions are of 68% C.L., medium blue regions are of 95% C.L., and light blue regions are of 99.7% C.L.

8 | Conclusion and outlook

In this thesis, we have considered axion-like particles as an ultra-light dark matter candidate that couples to neutrinos. We have studied a scenario where axion-like dark matter interacts with high-energy neutrinos, via a heavy neutral lepton, and searched for evidence of its existence in 7.5 years of High Energy Neutrino Events (HESE) collected by the IceCube neutrino telescope.

We have computed the diffuse flux of high-energy neutrinos from a population of astrophysical sources, allowing them to interact with a cosmological background of axion-like dark matter as they propagate from their sources to Earth. These interactions imprint characteristic features on the high-energy neutrino spectrum. We computed the fluxes for a wide range of values of the parameters that control axion-neutrino interactions and of the parameters that describe the spectrum with which high-energy astrophysical neutrinos are produced. In addition, we computed the corresponding expected rate of HESE events in IceCube, by adapting the same Monte Carlo simulation that is used by the IceCube Collaboration, which is built on a detailed description of the detector. Finally, we used a Bayesian statistical analysis to compare the predicted event rates to the observed HESE data. In doing so, we took into account the irreducible background of atmospheric neutrinos and muons using the same predictions as the IceCube Collaboration.

Our analysis found no statistically significant evidence for the existence of axion-neutrino interactions in 7.5 years of HESE data. Therefore, we set bounds on the parameters involved in the interactions: the mass of the axion-like dark matter particle, the mass of the heavy neutral lepton mediator, and the coupling strength of the interaction. These are the first bounds set on the neutrino-axion coupling set using a diffuse flux of high-energy astrophysical neutrinos.

On the experimental side, future observations may extend our analysis to higher energies. The planned upgrade to IceCube, IceCube-Gen2 [199], will have an energy range up to ultra-high energies, where it will search for the long-predicted flux of ultra-high energy neutrinos, with EeV-scale energies. The fluxes that we have computed in Chapter 4 already extend to these energies. Using higher neutrino energies would allow us to test higher resonance energies and, consequently, heavier mediators. Additionally, IceCube-Gen2 will be about 10 times larger than the current detector and increase the number of observations at TeV–PeV energies with an order of magnitude in the same time span. Other neutrino Cherenkov experiments that will provide more statistics in the IceCube energy range include KM3NeT, Baikal-GVD and P-ONE [200].

On the theory side, the model that we have explored only used flavor-universal cou-

plings. However, in the future, when more data is available, we may be able to explore flavor-dependent couplings, and how they possibly affect the flux of different neutrino flavors separately. Furthermore, we only explored ultra-light scalar dark matter, but dark matter may have other spins (vector, pseudo-vector etc.), which may lead to different features in the neutrino spectrum.

Bibliography

- [1] M.G. Aartsen et al. (IceCube). Evidence for High-Energy Extraterrestrial Neutrinos at the IceCube Detector. *Science*, 342(6161), 2013.
- [2] F. Zwicky. Die Rotverschiebung von extragalaktischen Nebeln. *Helv. Phys. Acta*, 6:110–127, 1933.
- [3] V. C. Rubin, W. K. Ford, Jr., and N. Thonnard. Extended rotation curves of high-luminosity spiral galaxies. IV. Systematic dynamical properties, Sa through Sc. *Astrophys. J. Lett.*, 225:L107–L111, 1978.
- [4] V. C. Rubin, W. K. Ford, Jr., and N. Thonnard. Rotational properties of 21 SC galaxies with a large range of luminosities and radii, from NGC 4605 ($R = 4$ kpc) to UGC 2885 ($R = 122$ kpc). *The Astrophysical Journal*, 238:471–487, 1980.
- [5] S. Profumo. Astrophysical Probes of Dark Matter. In *Theoretical Advanced Study Institute in Elementary Particle Physics: Searching for New Physics at Small and Large Scales*, pages 143–189, 2013.
- [6] Giorgio Arcadi, Maíra Dutra, Pradipta Ghosh, Manfred Lindner, Yann Mambrini, Mathias Pierre, Stefano Profumo, and Farinaldo S. Queiroz. The waning of the WIMP? A review of models, searches, and constraints. *Eur. Phys. J. C*, 78(3):203, 2018.
- [7] G. Bertone. The moment of truth for WIMP Dark Matter. *Nature*, 468:389–393, 2010.
- [8] R. D. Peccei and H. R. Quinn. CP Conservation in the Presence of Instantons. *Phys. Rev. Lett.*, 38:1440–1443, 1977.
- [9] R. D. Peccei and H. R. Quinn. Constraints Imposed by CP Conservation in the Presence of Instantons. *Phys. Rev. D*, 16:1791–1797, 1977.
- [10] H. Primakoff. Photoproduction of neutral mesons in nuclear electric fields and the mean life of the neutral meson. *Phys. Rev.*, 81:899, 1951.
- [11] R. Abbasi et al. (IceCube). IceCube high-energy starting event sample: Description and flux characterization with 7.5 years of data. *Phys. Rev. D*, 104:022002, Jul 2021.
- [12] R. Massey, T. Kitching, and J. Richard. The dark matter of gravitational lensing. *Rept. Prog. Phys.*, 73:086901, 2010.

- [13] K. G. Begeman, A. H. Broeils, and R. H. Sanders. Extended rotation curves of spiral galaxies: Dark haloes and modified dynamics. *Mon. Not. Roy. Astron. Soc.*, 249:523, 1991.
- [14] G. F. Smoot and others (COBE). Structure in the COBE differential microwave radiometer first year maps. *Astrophys. J. Lett.*, 396:L1–L5, 1992.
- [15] Olga Mena, Irina Mocioiu, and Soebur Razzaque. Oscillation effects on high-energy neutrino fluxes from astrophysical hidden sources. *Phys. Rev. D*, 75:063003, 2007.
- [16] J. F. Navarro, C. S. Frenk, and S. D. M. White. A Universal density profile from hierarchical clustering. *Astrophys. J.*, 490:493–508, 1997.
- [17] A. Burkert. The Structure of dark matter halos in dwarf galaxies. *Astrophys. J. Lett.*, 447:L25, 1995.
- [18] L. Anderson and others (BOSS). The clustering of galaxies in the SDSS-III Baryon Oscillation Spectroscopic Survey: baryon acoustic oscillations in the Data Releases 10 and 11 Galaxy samples. *Mon. Not. Roy. Astron. Soc.*, 441(1):24–62, 2014.
- [19] N. Aghanim et al. (Planck Collaboration). Planck 2018 results. VI. Cosmological parameters. *Astronomy & Astrophysics*, 641:A6, 2020.
- [20] Barry R. Holstein. Graviton Physics. *Am. J. Phys.*, 74:1002–1011, 2006.
- [21] Standard Model, <https://www.physik.uzh.ch/en/researcharea/lhcb/outreach/StandardModel.html>, Last visited Dec 13, 2019.
- [22] R. L. Workman and Others (Particle Data Group). Review of Particle Physics. *PTEP*, 2022:083C01, 2022.
- [23] A. H. G. Peter. Mapping the allowed parameter space for decaying dark matter models. *Phys. Rev. D*, 81:083511, 2010.
- [24] D. N. Spergel and others (WMAP). First year Wilkinson Microwave Anisotropy Probe (WMAP) observations: Determination of cosmological parameters. *Astrophys. J. Suppl.*, 148:175–194, 2003.
- [25] Jonathan L. Feng. Dark Matter Candidates from Particle Physics and Methods of Detection. *Ann. Rev. Astron. Astrophys.*, 48:495–545, 2010.
- [26] E. G. M. Ferreira. Ultra-light dark matter. *Astron. Astrophys. Rev.*, 29(1):7, 2021.
- [27] B. Carr and F. Kühnel. Primordial black holes as dark matter candidates. *SciPost Phys. Lect. Notes*, 48:1, 2022.
- [28] M. Y. Khlopov. Direct and Indirect Probes for Composite Dark Matter. *Front. in Phys.*, 7:4, 2019.

- [29] D. M. Jacobs, G. D. Starkman, and B. W. Lynn. Macro Dark Matter. *Mon. Not. Roy. Astron. Soc.*, 450(4):3418–3430, 2015.
- [30] G. Jungman, M. Kamionkowski, and K. Griest. Supersymmetric dark matter. *Phys. Rept.*, 267:195–373, 1996.
- [31] G. Bertone, D. Hooper, and J. Silk. Particle dark matter: Evidence, candidates and constraints. *Phys. Rept.*, 405:279–390, 2005.
- [32] B. Dasgupta and J. Kopp. Sterile neutrinos. *Physics Reports*, 928:1–63, 2021.
- [33] M. Thomson. *Modern Particle Physics*. Cambridge University Press, 2013.
- [34] C. A. Baker et al. An Improved experimental limit on the electric dipole moment of the neutron. *Phys. Rev. Lett.*, 97:131801, 2006.
- [35] M. Schwartz. *Modern Particle Physics*. Cambridge University Press, 2014.
- [36] F. Wilczek. Problem of Strong P and T Invariance in the Presence of Instantons. *Phys. Rev. Lett.*, 40:279–282, 1978.
- [37] S. Weinberg. A New Light Boson? *Phys. Rev. Lett.*, 40:223–226, 1978.
- [38] M. Gorghetto and G. Villadoro. Topological Susceptibility and QCD Axion Mass: QED and NNLO corrections. *JHEP*, 03:033, 2019.
- [39] M. Dine, P. Huet, R. L. Singleton, Jr, and L. Susskind. Creating the baryon asymmetry at the electroweak phase transition. *Phys. Lett. B*, 257:351–356, 1991.
- [40] E. I. Guendelman and D. A. Owen. Axion driven baryogenesis. *Phys. Lett. B*, 276:108–114, 1992.
- [41] I. P. Stern. Axion Dark Matter Searches. *AIP Conf. Proc.*, 1604(1):456–461, 2015.
- [42] J. Jaeckel et al. Snowmass 2021 White Paper: Axion Dark Matter. In *2022 Snowmass Summer Study*, 2022.
- [43] S. J. Asztalos, L. J. Rosenberg, K. van Bibber, P. Sikivie, and K. Zioutas. Searches for astrophysical and cosmological axions. *Ann. Rev. Nucl. Part. Sci.*, 56:293–326, 2006.
- [44] M. S. Pshirkov and S. B. Popov. Conversion of Dark matter axions to photons in magnetospheres of neutron stars. *J. Exp. Theor. Phys.*, 108:384–388, 2009.
- [45] E. Guarini, P. Carenza, J. Galan, M. Giannotti, and A. Mirizzi. Production of axionlike particles from photon conversions in large-scale solar magnetic fields. *Phys. Rev. D*, 102(12):123024, 2020.
- [46] K. Van Bibber, N. R. Dagdeviren, S. E. Koonin, A. K. Kerman, and H. N. Nelson. Proposed experiment to produce and detect light pseudoscalars. *Phys. Rev. Lett.*, 59:759–762, 1987.

- [47] S. L. Adler, J. Gamboa, F. Mendez, and J. Lopez-Sarrion. Axions and 'Light Shining Through a Wall': A Detailed Theoretical Analysis. *Annals Phys.*, 323:2851–2872, 2008.
- [48] Pugnât, P. and others (OSQAR). Search for weakly interacting sub-eV particles with the OSQAR laser-based experiment: results and perspectives. *Eur. Phys. J. C*, 74(8):3027, 2014.
- [49] Ciaran O'Hare. cajohare/axionlimits: Axionlimits. <https://cajohare.github.io/AxionLimits/>, July 2020.
- [50] N. Du and others (ADMX). A Search for Invisible Axion Dark Matter with the Axion Dark Matter Experiment. *Phys. Rev. Lett.*, 120(15):151301, 2018.
- [51] C. Boutan and others (ADMX). Piezoelectrically Tuned Multimode Cavity Search for Axion Dark Matter. *Phys. Rev. Lett.*, 121(26):261302, 2018.
- [52] T. Braine and others (ADMX). Extended Search for the Invisible Axion with the Axion Dark Matter Experiment. *Phys. Rev. Lett.*, 124(10):101303, 2020.
- [53] C. Bartram and others (ADMX). Search for Invisible Axion Dark Matter in the 3.3–4.2 μeV Mass Range. *Phys. Rev. Lett.*, 127(26):261803, 2021.
- [54] D. Alesini et al. Galactic axions search with a superconducting resonant cavity. *Phys. Rev. D*, 99(10):101101, 2019.
- [55] D. Alesini et al. Search for invisible axion dark matter of mass $m_a = 43 \mu\text{eV}$ with the QUAX- $a\gamma$ experiment. *Phys. Rev. D*, 103(10):102004, 2021.
- [56] A. Arza, M. A. Fedderke, P. W. Graham, D. F. Jackson Kimball, and S. Kalia. Earth as a transducer for axion dark-matter detection. 12 2021.
- [57] S. J. Asztalos, G. Carosi, C. Hagmann, D. Kinion, K. van Bibber, M. Hotz, L. J. Rosenberg, G. Rybka, J. Hoskins, J. Hwang, P. Sikivie, D. B. Tanner, R. Bradley, J. Clarke, and ADMX Collaboration. SQUID-Based Microwave Cavity Search for Dark-Matter Axions. *Phys. Rev. Lett.*, 104(4):041301, January 2010.
- [58] C. Bartram et al. Dark Matter Axion Search Using a Josephson Traveling Wave Parametric Amplifier. 10 2021.
- [59] O. Kwon and others (CAPP). First Results from an Axion Haloscope at CAPP around 10.7 μeV . *Phys. Rev. Lett.*, 126(19):191802, 2021.
- [60] A. Álvarez Melcón and others (CAST). First results of the CAST-RADES haloscope search for axions at 34.67 μeV . *JHEP*, 21:075, 2020.
- [61] H. Chang et al. First Results from the Taiwan Axion Search Experiment with Haloscope at 19.6 μeV . 5 2022.

- [62] N. Crisosto, P. Sikivie, N. S. Sullivan, D. B. Tanner, J. Yang, and G. Rybka. ADMX SLIC: Results from a Superconducting LC Circuit Investigating Cold Axions. *Phys. Rev. Lett.*, 124(24):241101, 2020.
- [63] S. DePanfilis, A. C. Melissinos, B. E. Moskowitz, J. T. Rogers, Y. K. Semertzidis, W. U. Wuensch, H. J. Halama, A. G. Prodel, W. B. Fowler, and F. A. Nezrick. Limits on the abundance and coupling of cosmic axions at $4.5 < m_a < 5.0 \mu\text{ev}$. *Phys. Rev. Lett.*, 59:839–842, Aug 1987.
- [64] J. A. Devlin et al. Constraints on the Coupling between Axionlike Dark Matter and Photons Using an Antiproton Superconducting Tuned Detection Circuit in a Cryogenic Penning Trap. *Phys. Rev. Lett.*, 126(4):041301, 2021.
- [65] A. V. Gramolin, D. Aybas, D. Johnson, J. Adam, and A. O. Sushkov. Search for axion-like dark matter with ferromagnets. *Nature Phys.*, 17(1):79–84, 2021.
- [66] T. Grenet, R. Ballou, Q. Basto, K. Martineau, P. Perrier, P. Pagnat, J. Quevillon, N. Roch, and C. Smith. The Grenoble Axion Haloscope platform (GrAHal): development plan and first results. 10 2021.
- [67] L. Zhong and others (HAYSTAC). Results from phase 1 of the HAYSTAC microwave cavity axion experiment. *Phys. Rev. D*, 97(9):092001, 2018.
- [68] K. M. Backes and others (HAYSTAC). A quantum-enhanced search for dark matter axions. *Nature*, 590(7845):238–242, 2021.
- [69] C. Hagmann, P. Sikivie, N. S. Sullivan, and D. B. Tanner. Results from a search for cosmic axions. *Phys. Rev. D*, 42:1297–1300, Aug 1990.
- [70] J. Jeong, S. Youn, S. Bae, J. Kim, T Seong, J. E. Kim, and Y. K. Semertzidis. Search for Invisible Axion Dark Matter with a Multiple-Cell Haloscope. *Phys. Rev. Lett.*, 125(22):221302, 2020.
- [71] S. Lee, S. Ahn, J. Choi, B. R. Ko, and Y. K. Semertzidis. Axion Dark Matter Search around $6.7 \mu\text{eV}$. *Phys. Rev. Lett.*, 124(10):101802, 2020.
- [72] Y. Lee, B. Yang, H. Yoon, M. Ahn, H. Park, B. Min, D. Kim, and J. Yoo. Searching for Invisible Axion Dark Matter with an 18 T Magnet Haloscope. *Phys. Rev. Lett.*, 128(24):241805, 2022.
- [73] B. T. McAllister, G. Flower, E. N. Ivanov, M. Goryachev, J. Bourhill, and M. E. Tobar. The ORGAN Experiment: An axion haloscope above 15 GHz. *Phys. Dark Univ.*, 18:67–72, 2017.
- [74] J. L. Ouellet et al. First Results from ABRACADABRA-10 cm: A Search for Sub- μeV Axion Dark Matter. *Phys. Rev. Lett.*, 122(12):121802, 2019.
- [75] C. P. Salemi et al. Search for Low-Mass Axion Dark Matter with ABRACADABRA-10 cm. *Phys. Rev. Lett.*, 127(8):081801, 2021.

- [76] C. A. Thomson, B. T. McAllister, M. Goryachev, E. N. Ivanov, and M. E. Tobar. Upconversion Loop Oscillator Axion Detection Experiment: A Precision Frequency Interferometric Axion Dark Matter Search with a Cylindrical Microwave Cavity. *Phys. Rev. Lett.*, 126(8):081803, 2021. [Erratum: *Phys.Rev.Lett.* 127, 019901 (2021)].
- [77] M. Betz, F. Caspers, M. Gasior, M. Thumm, and S. W. Rieger. First results of the CERN Resonant Weakly Interacting sub-eV Particle Search (CROWS). *Phys. Rev. D*, 88(7):075014, 2013.
- [78] S. Andriamonje and others (CAST). An Improved limit on the axion-photon coupling from the CAST experiment. *JCAP*, 04:010, 2007.
- [79] V. Anastassopoulos and others (CAST). New CAST Limit on the Axion-Photon Interaction. *Nature Phys.*, 13:584–590, 2017.
- [80] F. Della Valle, A. Ejlli, U. Gastaldi, G. Messineo, E. Milotti, R. Pengo, G. Ruoso, and G. Zavattini. The PVLAS experiment: measuring vacuum magnetic birefringence and dichroism with a birefringent Fabry–Perot cavity. *Eur. Phys. J. C*, 76(1):24, 2016.
- [81] K. Ehret et al. New ALPS Results on Hidden-Sector Lightweights. *Phys. Lett. B*, 689:149–155, 2010.
- [82] S.-F. Ge, K. Hamaguchi, K. Ichimura, K. Ishidoshiro, Y. Kanazawa, Y. Kishimoto, N. Nagata, and J. Zheng. Supernova-scope for the Direct Search of Supernova Axions. *JCAP*, 11:059, 2020.
- [83] R. Ballou and others (OSQAR). New exclusion limits on scalar and pseudoscalar axionlike particles from light shining through a wall. *Phys. Rev. D*, 92(9):092002, 2015.
- [84] M. D. Ortiz et al. Design of the ALPS II Optical System. 9 2020.
- [85] K. Homma and others (SAPPHIRES). Search for sub-eV axion-like resonance states via stimulated quasi-parallel laser collisions with the parameterization including fully asymmetric collisional geometry. 5 2021.
- [86] I. Shilon, A. Dudarev, H. Silva, U. Wagner, and H. H. J. ten Kate. The Superconducting Toroid for the New International AXion Observatory (IAXO). *IEEE Trans. Appl. Supercond.*, 24(3):4500104, 2014.
- [87] A. Ayala, I. Domínguez, M. Giannotti, A. Mirizzi, and O. Straniero. Revisiting the bound on axion-photon coupling from Globular Clusters. *Phys. Rev. Lett.*, 113(19):191302, 2014.
- [88] R. A. Battye, J. Darling, J. McDonald, and S. Srinivasan. Towards Robust Constraints on Axion Dark Matter using PSR J1745-2900. 7 2021.
- [89] B. D. Blout, E. J. Daw, M. P. Decowski, Paul T. P. Ho, L. J. Rosenberg, and D. B. Yu. A Radio telescope search for axions. *Astrophys. J.*, 546:825–828, 2001.

- [90] B. Bolliet, J. Chluba, and R. Battye. Spectral distortion constraints on photon injection from low-mass decaying particles. *Mon. Not. Roy. Astron. Soc.*, 507(3):3148–3178, 2021.
- [91] M. A. Buen-Abad, J. Fan, and C. Sun. Constraints on Axions from Cosmic Distance Measurements. 11 2020.
- [92] F. Calore, P. Carenza, M. Giannotti, J. Jaeckel, and A. Mirizzi. Bounds on axionlike particles from the diffuse supernova flux. *Phys. Rev. D*, 102(12):123005, 2020.
- [93] F. Calore, P. Carenza, C. Eckner, T. Fischer, M. Giannotti, J. Jaeckel, K. Kotake, T. Kuroda, A. Mirizzi, and F. Sivo. 3D template-based *Fermi*-LAT constraints on axion-like particles. 10 2021.
- [94] A. Caputo, G. Raffelt, and E. Vitagliano. Muonic boson limits: Supernova redux. *Phys. Rev. D*, 105(3):035022, 2022.
- [95] A. Caputo, H.-T. Janka, G. Raffelt, and E. Vitagliano. Low-Energy Supernovae Severely Constrain Radiative Particle Decays. *Phys. Rev. Lett.*, 128(22):221103, 2022.
- [96] M. H. Chan. Constraining the axion-photon coupling using radio data of the Bullet Cluster. *Sci. Rep.*, 11:20087, 2021.
- [97] J. Darling. New Limits on Axionic Dark Matter from the Magnetar PSR J1745-2900. *Astrophys. J. Lett.*, 900(2):L28, 2020.
- [98] C. Dessert, J. W. Foster, and B. R. Safdi. X-ray Searches for Axions from Super Star Clusters. *Phys. Rev. Lett.*, 125(26):261102, 2020.
- [99] C. Dessert, A. J. Long, and B. R. Safdi. No evidence for axions from Chandra observation of magnetic white dwarf. 4 2021.
- [100] C. Dessert, D. Dunskey, and B. R. Safdi. Upper limit on the axion-photon coupling from magnetic white dwarf polarization. 3 2022.
- [101] M. J. Dolan, F. J. Hiskens, and R. R. Volkas. Constraining axion-like particles using the white dwarf initial-final mass relation. *JCAP*, 09:010, 2021.
- [102] M. J. Dolan, F. J. Hiskens, and R. R. Volkas. Advancing Globular Cluster Constraints on the Axion-Photon Coupling. 7 2022.
- [103] M. Ajello and others (Fermi-LAT). Search for Spectral Irregularities due to Photon–Axionlike-Particle Oscillations with the Fermi Large Area Telescope. *Phys. Rev. Lett.*, 116(16):161101, 2016.
- [104] J. W. Foster, Y. Kahn, O. Macias, Z. Sun, R. P. Eatough, V. I. Kondratiev, W. M. Peters, C. Weniger, and B. R. Safdi. Green Bank and Effelsberg Radio Telescope Searches for Axion Dark Matter Conversion in Neutron Star Magnetospheres. *Phys. Rev. Lett.*, 125(17):171301, 2020.

- [105] J. W. Foster, M. Kongsore, C. Dessert, Y. Park, N. L. Rodd, K. Cranmer, and B. R. Safdi. Deep Search for Decaying Dark Matter with XMM-Newton Blank-Sky Observations. *Phys. Rev. Lett.*, 127(5):051101, 2021.
- [106] J. W. Foster, S. J. Witte, M. Lawson, T. Linden, V. Gajjar, C. Weniger, and B. R. Safdi. Extragalactic Axion Search with the Breakthrough Listen Galactic Center Survey. 2 2022.
- [107] D. Grin, G. Covone, J.-P. Kneib, M. Kamionkowski, A. Blain, and E. Jullo. A Telescope Search for Decaying Relic Axions. *Phys. Rev. D*, 75:105018, 2007.
- [108] A. Abramowski and others (H.E.S.S.). Constraints on axionlike particles with H.E.S.S. from the irregularity of the PKS 2155-304 energy spectrum. *Phys. Rev. D*, 88(10):102003, 2013.
- [109] S. Jacobsen, T. Linden, and K. Freese. Constraining Axion-Like Particles with HAWC Observations of TeV Blazars. 3 2022.
- [110] J. Jaeckel, P. C. Malta, and J. Redondo. Decay photons from the axionlike particles burst of type II supernovae. *Phys. Rev. D*, 98(5):055032, 2018.
- [111] A. Keller, S. O’Brien, A. Kamdar, N. Rapidis, A. Leder, and K. van Bibber. A Model-Independent Radio Telescope Dark Matter Search. 12 2021.
- [112] H.-J. Li, J.-G. Guo, X.-J. Bi, S.-J. Lin, and P.-F. Yin. Limits on axionlike particles from Mrk 421 with 4.5-year period observations by ARGO-YBJ and Fermi-LAT. *Phys. Rev. D*, 103(8):083003, 2021.
- [113] M. C. D. Marsh, H. R. Russell, A. C. Fabian, B. P. McNamara, P. Nulsen, and C. S. Reynolds. A New Bound on Axion-Like Particles. *JCAP*, 12:036, 2017.
- [114] M. Meyer and T. Petrushevska. Search for Axionlike-Particle-Induced Prompt γ -Ray Emission from Extragalactic Core-Collapse Supernovae with the *Fermi* Large Area Telescope. *Phys. Rev. Lett.*, 124(23):231101, 2020. [Erratum: *Phys.Rev.Lett.* 125, 119901 (2020)].
- [115] A. Payez, C. Evoli, T. Fischer, M. Giannotti, A. Mirizzi, and A. Ringwald. Revisiting the SN1987A gamma-ray limit on ultralight axion-like particles. *JCAP*, 02:006, 2015.
- [116] M. Regis, M. Taoso, D. Vaz, J. Brinchmann, S. L. Zoutendijk, N. F. Bouché, and M. Steinmetz. Searching for light in the darkness: Bounds on ALP dark matter with the optical MUSE-faint survey. *Phys. Lett. B*, 814:136075, 2021.
- [117] J. Sisk Reynés, J. H. Matthews, C. S. Reynolds, H. R. Russell, R. N. Smith, and M. C. D. Marsh. New constraints on light Axion-Like Particles using Chandra Transmission Grating Spectroscopy of the powerful cluster-hosted quasar H1821+643. 9 2021.

- [118] C. S. Reynolds, M. C. D. Marsh, H. R. Russell, A. C. Fabian, R. Smith, F. Tombesi, and S. Veilleux. Astrophysical Limits on Very Light Axion-like Particles from Chandra Grating Spectroscopy of NGC 1275. *Astrophys. J.*, 890(1):59, February 2020.
- [119] N. Vinyoles, A. Serenelli, F. L. Villante, S. Basu, J. Redondo, and J. Isern. New axion and hidden photon constraints from a solar data global fit. *JCAP*, 2015(10):015, October 2015.
- [120] D. Wadekar and Z. Wang. Strong constraints on decay and annihilation of dark matter from heating of gas-rich dwarf galaxies. 11 2021.
- [121] D. Wouters and P. Brun. Constraints on Axion-like Particles from X-Ray Observations of the Hydra Galaxy Cluster. *Astrophys. J.*, 772:44, 2013.
- [122] M. Xiao, K. M. Perez, M. Giannotti, O. Straniero, A. Mirizzi, B. W. Grefenstette, B. M. Roach, and M. Nynka. Constraints on Axionlike Particles from a Hard X-Ray Observation of Betelgeuse. *Phys. Rev. Lett.*, 126(3):031101, 2021.
- [123] D. Cadamuro and J. Redondo. Cosmological bounds on pseudo Nambu-Goldstone bosons. *JCAP*, 02:032, 2012.
- [124] P. F. Depta, M. Hufnagel, and K. Schmidt-Hoberg. Robust cosmological constraints on axion-like particles. *JCAP*, 05:009, 2020.
- [125] M. Dine, W. Fischler, and M. Srednicki. A Simple Solution to the Strong CP Problem with a Harmless Axion. *Phys. Lett. B*, 104:199–202, 1981.
- [126] A. R. Zhitnitsky. On Possible Suppression of the Axion Hadron Interactions. (In Russian). *Sov. J. Nucl. Phys.*, 31:260, 1980.
- [127] J. E. Kim. Weak Interaction Singlet and Strong CP Invariance. *Phys. Rev. Lett.*, 43:103, 1979.
- [128] M. A. Shifman, A. I. Vainshtein, and V. I. Zakharov. Can Confinement Ensure Natural CP Invariance of Strong Interactions? *Nucl. Phys. B*, 166:493–506, 1980.
- [129] R. Davis, D. S. Harmer, and K. C. Hoffman. Search for Neutrinos from the Sun. *Phys. Rev. Lett.*, 20:1205–1209, 1968.
- [130] John N. Bahcall. *NEUTRINO ASTROPHYSICS*. Cambridge University Press, 1989.
- [131] Y. Fukuda and others (Kamiokande). Solar neutrino data covering solar cycle 22. *Phys. Rev. Lett.*, 77:1683–1686, 1996.
- [132] W. Hampel and others (GALLEX). GALLEX solar neutrino observations: Results for GALLEX IV. *Phys. Lett. B*, 447:127–133, 1999.
- [133] B. Pontecorvo. Inverse beta processes and nonconservation of lepton charge. *Zh. Eksp. Teor. Fiz.*, 34:247, 1957.

- [134] Z. Maki, M. Nakagawa, and S. Sakata. Remarks on the unified model of elementary particles. *Prog. Theor. Phys.*, 28:870–880, 1962.
- [135] Q. R. Ahmad and others (SNO). Direct evidence for neutrino flavor transformation from neutral current interactions in the Sudbury Neutrino Observatory. *Phys. Rev. Lett.*, 89:011301, 2002.
- [136] I. Esteban, M. C. Gonzalez-Garcia, M. Maltoni, T. Schwetz, and A. Zhou. The fate of hints: updated global analysis of three-flavor neutrino oscillations. *JHEP*, 09:178, 2020.
- [137] S. Adrian-Martinez and others (KM3Net). Letter of intent for KM3NeT 2.0. *J. Phys. G*, 43(8):084001, 2016.
- [138] C. Giunti and C. W. Kim. *Fundamentals of Neutrino Physics and Astrophysics*. Oxford University Press, 2007.
- [139] LSND Collaboration. Evidence for Neutrino Oscillations from the Observation of Electron Anti-neutrinos in a Muon Anti-Neutrino Beam. *Physical Review D*, 64(11), 2001.
- [140] MiniBooNE Collaboration. Significant Excess of Electronlike Events in the MiniBooNE Short-Baseline Neutrino Experiment. *Physical Review Letters*, 121(22), 2018.
- [141] Alexey Boyarsky, Jeroen Franse, Dmytro Iakubovskiy, and Oleg Ruchayskiy. Checking the Dark Matter Origin of a 3.53 keV Line with the Milky Way Center. *Phys. Rev. Lett.*, 115:161301, 2015.
- [142] Alexander Merle and Aurel Schneider. Production of Sterile Neutrino Dark Matter and the 3.5 keV line. *Phys. Lett. B*, 749:283–288, 2015.
- [143] K. et al. Hirata. Observation of a neutrino burst from the supernova SN1987A. *Phys. Rev. Lett.*, 58:1490–1493, Apr 1987.
- [144] R. M. et al. Bionta. Observation of a neutrino burst in coincidence with supernova 1987A in the Large Magellanic Cloud. *Phys. Rev. Lett.*, 58:1494–1496, Apr 1987.
- [145] E. N. Alekseev, L. N. Alekseeva, I. V. Krivosheina, and V. I. Volchenko. Detection of the Neutrino Signal From SN1987A in the LMC Using the Inr Baksan Underground Scintillation Telescope. *Phys. Lett. B*, 205:209–214, 1988.
- [146] Mirizzi et al. Supernova Neutrinos: Production, Oscillations and Detection. *La Rivista del Nuovo Cimento*, 39(102):1–112, 2016.
- [147] R. Abbasi et al. (IceCube). A search for neutrino emission from cores of Active Galactic Nuclei. 2021.
- [148] A. M. Hillas. The Origin of Ultrahigh-Energy Cosmic Rays. *Ann. Rev. Astron. Astrophys.*, 22:425–444, 1984.

- [149] Enrico Fermi. On the Origin of the Cosmic Radiation. *Phys. Rev.*, 75:1169–1174, 1949.
- [150] Dejan Urošević, Bojan Arbutina, and Dušan Onić. Particle acceleration in interstellar shocks. *Astrophys. Space Sci.*, 364(10):185, 2019.
- [151] M. et al. Ackermann. High-energy and ultra-high-energy neutrinos. 2022.
- [152] M.G. Aartsen et al. (IceCube). The IceCube Neutrino Observatory: instrumentation and online systems. *Journal of Instrumentation*, 12(03):P03012–P03012, 2017.
- [153] J. A. Formaggio and G. P. Zeller. From eV to EeV: Neutrino Cross Sections Across Energy Scales. *Rev. Mod. Phys.*, 84:1307–1341, 2012.
- [154] P. A. Čerenkov. Visible Radiation Produced by Electrons Moving in a Medium with Velocities Exceeding that of Light. *Phys. Rev.*, 52:378–379, 1937.
- [155] I. M. Frank and I. E. Tamm. Coherent visible radiation of fast electrons passing through matter. *Compt. Rend. Acad. Sci. URSS*, 14(3):109–114, 1937.
- [156] John G. Learned and Sandip Pakvasa. Detecting tau-neutrino oscillations at PeV energies. *Astropart. Phys.*, 3:267–274, 1995.
- [157] R. Abbasi et al. A muon-track reconstruction exploiting stochastic losses for large-scale Cherenkov detectors. *JINST*, 16(08):P08034, 2021.
- [158] M. Ahlers and F. Halzen. Opening a new window onto the universe with IceCube. *Progress in Particle and Nuclear Physics*, 102:73–88, 2018.
- [159] M.G. Aartsen et al. (IceCube). Neutrino emission from the direction of the blazar TXS 0506+056 prior to the IceCube-170922A alert. *Science*, 361(6398):147–151, 2018.
- [160] M. Bustamante, C. Rosenstrøm, S. Shalgar, and I. Tamborra. Bounds on secret neutrino interactions from high-energy astrophysical neutrinos. *Physical Review D*, 101(12), 2020.
- [161] M.G. Aartsen et al. (IceCube). An eV-Scale Sterile Neutrino Search Using Eight Years of Atmospheric Muon Neutrino Data from the IceCube Neutrino Observatory. *Physical Review Letters*, 125(14), 2020.
- [162] K. C. Y. Ng and J. F. Beacom. Cosmic neutrino cascades from secret neutrino interactions. *Phys. Rev. D*, 90(6):065035, 2014.
- [163] G. Breit and E. Wigner. Capture of slow neutrons. *Phys. Rev.*, 49:519–531, 1936.
- [164] A. K. Drukier, Katherine Freese, and D. N. Spergel. Detecting Cold Dark Matter Candidates. *Phys. Rev. D*, 33:3495–3508, 1986.
- [165] Katherine Freese, Joshua A. Frieman, and Andrew Gould. Signal Modulation in Cold Dark Matter Detection. *Phys. Rev. D*, 37:3388–3405, 1988.

- [166] K. J. Kelly and P. A. N. Machado. Multimessenger Astronomy and New Neutrino Physics. *JCAP*, 10:048, 2018.
- [167] D. W. Hogg. Distance measures in cosmology, 1999.
- [168] H. Yüksel, M. D. Kistler, J. F. Beacom, and A. M. Hopkins. Revealing the High-Redshift Star Formation Rate with Gamma-Ray Bursts. *The Astrophysical Journal*, 683(1):L5–L8, 2008.
- [169] J. I. Read. The Local Dark Matter Density. *J. Phys. G*, 41:063101, 2014.
- [170] A. DiFranzo and D. Hooper. Searching for MeV-scale gauge bosons with IceCube. *Physical Review D*, 92(9), 2015.
- [171] A. B. Balantekin, A. de Gouvêa, and B. Kayser. Addressing the Majorana vs. Dirac question with neutrino decays. *Physics Letters B*, 789:488–495, 2019.
- [172] M. et al. Galassi. GNU Scientific Library Reference Manual (3rd Ed.), 2009.
- [173] Steven Weinberg. *Cosmology*. Oxford University Press, 2008.
- [174] R. Gandhi, C. Quigg, M. H. Reno, and I. Sarcevic. Ultrahigh-energy neutrino interactions. *Astropart. Phys.*, 5:81–110, 1996.
- [175] A. Connolly, R. S. Thorne, and D. Waters. Calculation of High Energy Neutrino-Nucleon Cross Sections and Uncertainties Using the MSTW Parton Distribution Functions and Implications for Future Experiments. *Phys. Rev. D*, 83:113009, 2011.
- [176] A. Cooper-Sarkar, P. Mertsch, and S. Sarkar. The high energy neutrino cross-section in the Standard Model and its uncertainty. *JHEP*, 08:042, 2011.
- [177] M. G. Aartsen et al. Measurement of the multi-TeV neutrino cross section with IceCube using Earth absorption. *Nature*, 551:596–600, 2017.
- [178] M. G. Aartsen and others (IceCube). Measurements using the inelasticity distribution of multi-TeV neutrino interactions in IceCube. *Phys. Rev. D*, 99(3):032004, 2019.
- [179] S. L. Glashow. Resonant Scattering of Antineutrinos. *Phys. Rev.*, 118:316–317, Apr 1960.
- [180] IceCube Collaboration. Detection of a particle shower at the Glashow resonance with IceCube. *Nature*, 591(7849):220–224, 2021.
- [181] L. Wolfenstein. Neutrino Oscillations in Matter. *Phys. Rev. D*, 17:2369–2374, 1978.
- [182] S. P. Mikheyev and A. Yu. Smirnov. Resonance Amplification of Oscillations in Matter and Spectroscopy of Solar Neutrinos. *Sov. J. Nucl. Phys.*, 42:913–917, 1985.
- [183] Soebur Razzaque and A. Yu. Smirnov. Flavor conversion of cosmic neutrinos from hidden jets. *JHEP*, 03:031, 2010.

- [184] C. A. Argüelles, J. Salvado, and C. N. Weaver. nuSQuIDS: A toolbox for neutrino propagation. *Comput. Phys. Commun.*, 277:108346, 2022.
- [185] A. M. Dziewonski and D. L. Anderson. Preliminary reference earth model. *Phys. Earth Planet. Interiors*, 25:297–356, 1981.
- [186] A. Bhattacharya, R. Enberg, M. H. Reno, I. Sarcevic, and A. Stasto. Perturbative charm production and the prompt atmospheric neutrino flux in light of RHIC and LHC. *Journal of High Energy Physics*, 2015(6), 2015.
- [187] IceCube Collaboration. <https://github.com/icecube/HESE-7-year-data-release>, 2020. HESE GitHub repository.
- [188] Carlos A. Argüelles, Austin Schneider, and Tianlu Yuan. A binned likelihood for stochastic models. *JHEP*, 06:030, 2019.
- [189] Anthony M. Hillas. Cosmic Rays: Recent Progress and some Current Questions. In *Conference on Cosmology, Galaxy Formation and Astro-Particle Physics on the Pathway to the SKA*, 7 2006.
- [190] Thomas K. Gaisser. Spectrum of cosmic-ray nucleons, kaon production, and the atmospheric muon charge ratio. *Astropart. Phys.*, 35:801–806, 2012.
- [191] Thomas K. Gaisser, Todor Stanev, and Serap Tilav. Cosmic Ray Energy Spectrum from Measurements of Air Showers. *Front. Phys. (Beijing)*, 8:748–758, 2013.
- [192] Felix Riehn, Hans P. Dembinski, Ralph Engel, Anatoli Fedynitch, Thomas K. Gaisser, and Todor Stanev. The hadronic interaction model SIBYLL 2.3c and Feynman scaling. *PoS, ICRC2017*:301, 2018.
- [193] D. Heck, J. Knapp, J. N. Capdevielle, G. Schatz, and T. Thouw. CORSIKA: A Monte Carlo code to simulate extensive air showers. 2 1998.
- [194] Eun-Joo Ahn, Ralph Engel, Thomas K. Gaisser, Paolo Lipari, and Todor Stanev. Cosmic ray interaction event generator SIBYLL 2.1. *Phys. Rev. D*, 80:094003, 2009.
- [195] Johannes Buchner. A statistical test for Nested Sampling algorithms. *Statistics and Computing*, 26(1-2):383–392, 2016.
- [196] Johannes Buchner. Collaborative Nested Sampling: Big Data versus Complex Physical Models. *Publications of the Astronomical Society of the Pacific*, 131(1004):108005, October 2019.
- [197] Johannes Buchner. UltraNest - a robust, general purpose Bayesian inference engine. *The Journal of Open Source Software*, 6(60):3001, 2021.
- [198] Harold Jeffreys. *The Theory of Probability*. Oxford University Press, 1939.

- [199] M. G. Aartsen et al. IceCube-Gen2: the window to the extreme Universe. *J. Phys. G*, 48(6):060501, 2021.
- [200] Roshan Mammen Abraham et al. Tau Neutrinos in the Next Decade: from GeV to EeV. 3 2022.
- [201] D. Fiorillo, G. Miele, S. Morisi, and N. Saviano. Cosmogenic neutrino fluxes under the effect of active-sterile secret interactions. *Physical Review D*, 101(8), 2020.

A | Extrapolation

A.1 Extrapolation models

Figure A.1 shows a comparison between several different extrapolation methods. The extrapolation is based on the last couple of full solutions to the propagation equation in the parameter range where it can be solved in a reasonable time. Specifically, the extrapolation happens along the coupling strength (g) direction. Three different one-dimensional interpolation methods were tested: linear extrapolation, second degree polynomial fit, and a univariate spline (with $k = 3$). The zoom-in on the bottom of the dip in the figure shows that the linear extrapolation gives the best result.

Figure A.2 shows the extrapolation procedure in two different spaces. We found that transforming the calculated fluxes to a different space could improve the performance of the extrapolation. The fluxes in Figure A.2 (a) are extrapolated in the normal flux space, which is not very linear, as can be seen in (b). This is a problem since we use a linear extrapolation. A more linear extrapolation space is achieved when dividing the flux for a given value of g with an approximate calculation of the flux, which does not take regeneration into account (described in Section A.2). By extrapolating in this space and then transforming back to the original space (by multiplying by the approximate solution again), the extrapolation improved.

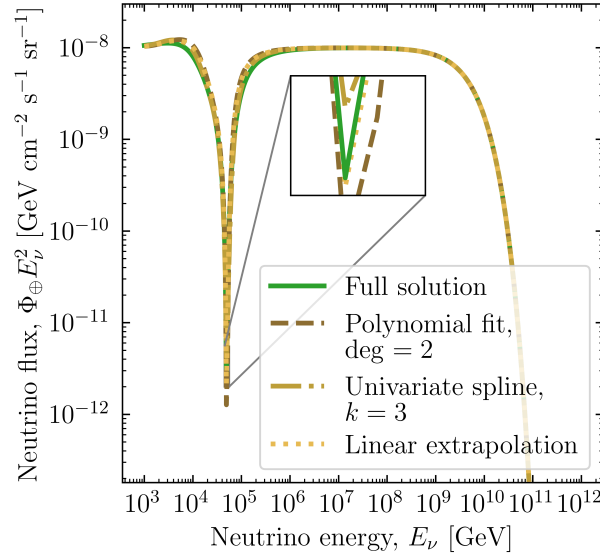


Figure A.1: An example of how the different one-dimensional extrapolations performed compared to the full solution. Here for $m_N = 10^{-3}$ GeV, $m_a = 10^{-11}$ GeV, $g = 10^{-3.75}$, $\gamma = 2$, $E_{\text{cut}} = 10^{10}$ GeV.

A.2 Analytical solution of the propagation equation

We will here solve the propagation equation of the journey of a high-energy astrophysical neutrino from its source to Earth, with the chance of interaction with axion-like dark matter (Eq. 4.3). The analytical solution of the propagation equation is inspired by Ref. [201].

The propagation equation without regeneration is expressed by the following in terms of redshift:

$$\begin{aligned}
 \frac{\partial \tilde{n}(z, E_{\nu})}{\partial z} &= -\frac{1}{(1+z)H(z)} \left\{ \frac{\partial}{\partial E_{\nu}} [H(z)E_{\nu}\tilde{n}(z, E_{\nu})] \right. \\
 &\quad \left. + \mathcal{W}(z)\mathcal{L}_0(E_{\nu}) - n_a(z)\sigma(E_{\nu})\tilde{n}(z, E_{\nu}) \right\} \\
 &= -\frac{1}{(1+z)H(z)} \left\{ H(z)\tilde{n}(z, E_{\nu}) + H(z)\frac{\partial \tilde{n}(z, E_{\nu})}{\partial E_{\nu}} E_{\nu} \right. \\
 &\quad \left. + \mathcal{W}(z)\mathcal{L}_0(E_{\nu}) - n_a(z)\sigma(E_{\nu})\tilde{n}(z, E_{\nu}) \right\}
 \end{aligned} \tag{A.1}$$

Rearranging the equation to be comparable with Eq. (22) in Ref. [201], this looks like

$$\begin{aligned}
 H(z) \left[\frac{\partial \tilde{n}(z, E_{\nu})}{\partial z} + \frac{E_{\nu}}{1+z} \frac{\partial \tilde{n}(z, E_{\nu})}{\partial E_{\nu}} \right] &= \\
 \frac{1}{1+z} \{ [n_a(z)\sigma(E_{\nu}) - H(z)]\tilde{n}(z, E_{\nu}) - \mathcal{W}(z)\mathcal{L}_0(E_{\nu}) \}.
 \end{aligned} \tag{A.2}$$

Based on Eq. (23) in Ref. [201], the analytical solution will be

$$\begin{aligned} \tilde{n}(z, E_\nu) = & \int_0^\infty \frac{dz}{H(z)(1+z)} \mathcal{W}(z) \mathcal{L}_0(E_\nu(1+z)) \\ & \cdot \exp \left[- \int_0^z \frac{dz'}{H(z')(1+z')} n_a(z') \sigma(E_\nu(1+z')) \right] \cdot \exp \left[\int_0^z \frac{dz'}{H(z')} \frac{H(z')}{1+z'} \right], \end{aligned} \quad (\text{A.3})$$

where

$$\exp \left[\int_0^z \frac{dz'}{H(z')} \frac{H(z')}{1+z'} \right] = \exp[\ln(1+z)] = 1+z. \quad (\text{A.4})$$

This will cancel the factor $1/(1+z)$ of the first term on the RHS of Eq. A.3. This yields

$$\begin{aligned} \tilde{n}(z=0, E_\nu) = & \int_0^\infty \frac{dz}{H(z)} \mathcal{W}(z) \mathcal{L}_0(E_\nu(1+z)) \\ & \cdot \exp \left[- \int_0^z \frac{dz'}{H(z')(1+z')} n_a(z') \sigma(E_\nu(1+z')) \right], \end{aligned} \quad (\text{A.5})$$

which is the analytical solution for the high-energy neutrino flux at Earth. Since we choose an upper limit of redshift of $z_{\text{max}} = 4$, the outer integral will go from 0 to 4.

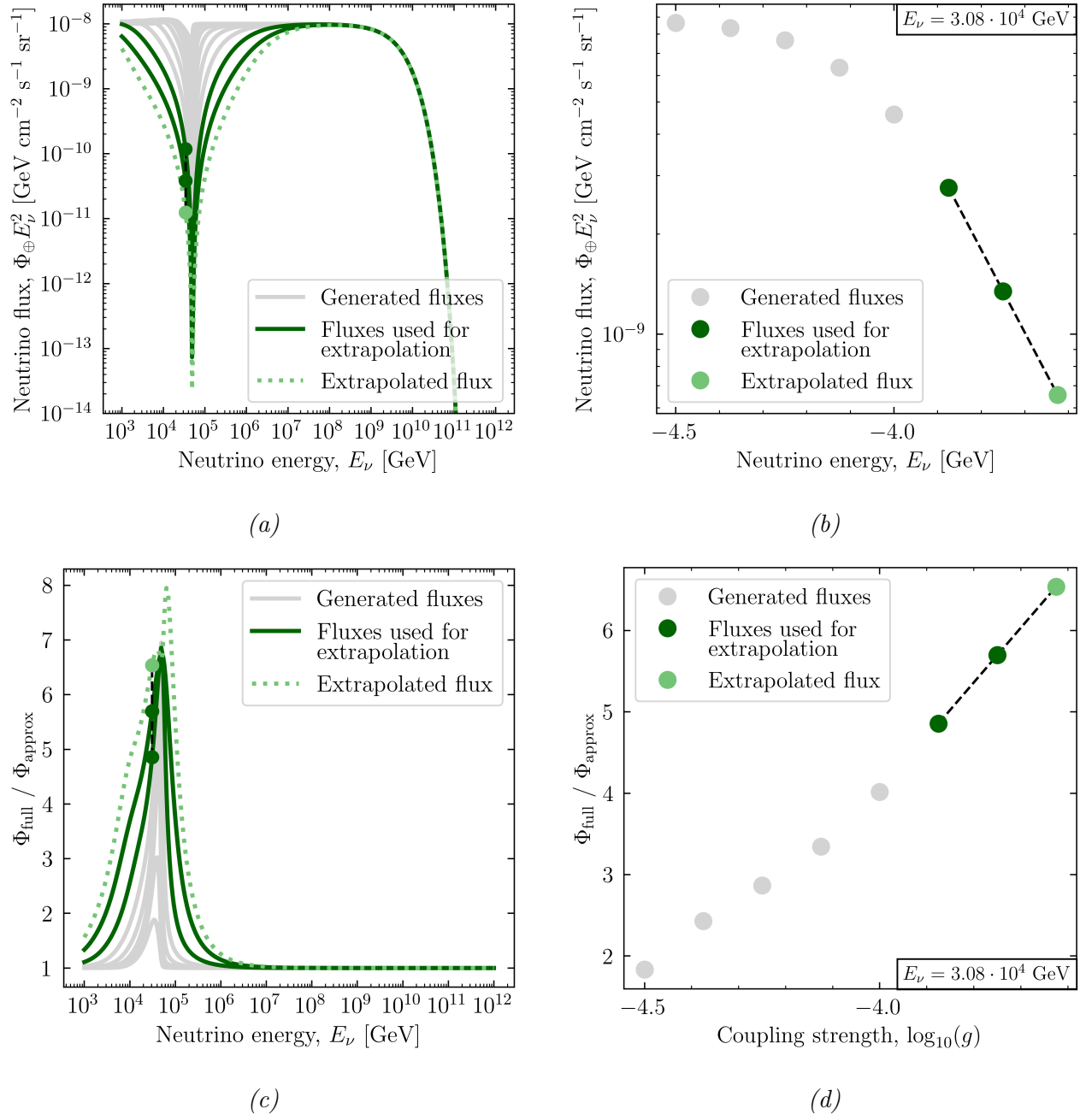


Figure A.2: Comparison of the extrapolation in the normal flux space in figure (a) and (b) versus the space where the fluxes from the solution of the propagation equation have been divided by their analytical approximation in (c) and (d). The latter space is more linear, and thus results in a better extrapolation. The difference in linearity is clear when comparing (c) and (d). The flux with the lowest coupling strength is normalized to $10^{-8} \text{ GeV cm}^{-2} \text{s}^{-1} \text{sr}^{-1}$. Here for the parameter values $m_N = 10^{-3} \text{ GeV}$, $m_a = 10^{-11} \text{ GeV}$, $\gamma = 2$ and $E_{\text{cut}} = 10^{10} \text{ GeV}$.

B | Posterior probability distributions

Figures B.1–B.3 show the posterior probability distributions for the parameters equivalent to the IceCube analysis, the parameters of free-streaming neutrinos, and the parameters of a flux with axion-neutrino interactions. Posterior probability distributions are the correlations between the different parameters. In each panel, we show the marginalized allowed regions of the two parameters on the respective axes. Figure B.1 is used to reproduce the results from the IceCube HESE analysis [11] and validate that our analysis works. This is true since the spectral index is $\gamma = 2.85^{+0.18}_{-0.11}$, compatible with the spectral index of the IceCube analysis of $\gamma = 2.87^{+0.20}_{-0.19}$.

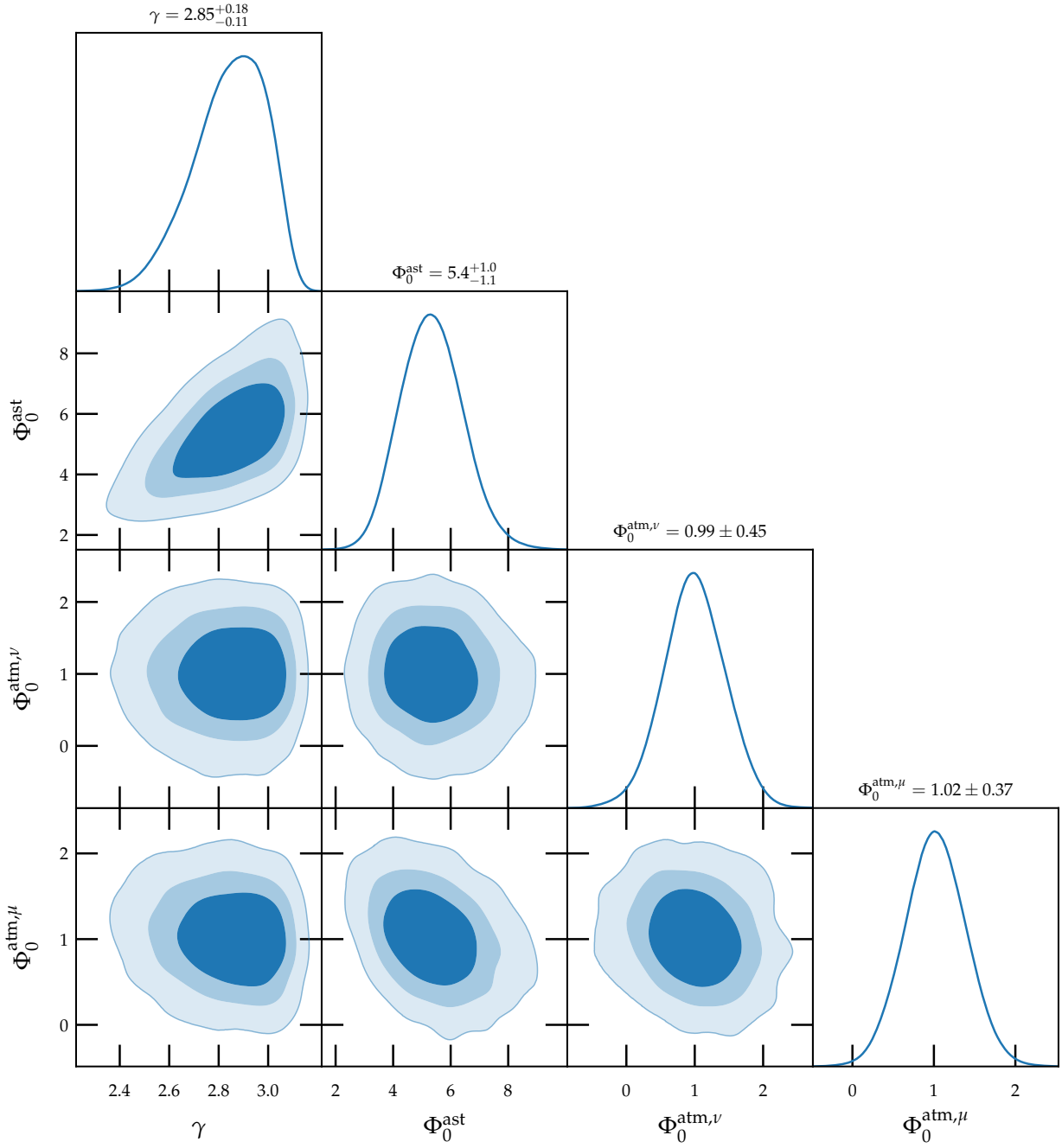


Figure B.1: Posterior probability distributions of the three normalization parameters and the spectral index, equivalent to the parameters of the IceCube HESE analysis. Darkest blue regions are of 68% C.L., medium blue regions are of 95% C.L., and light blue regions are of 99.7% C.L.

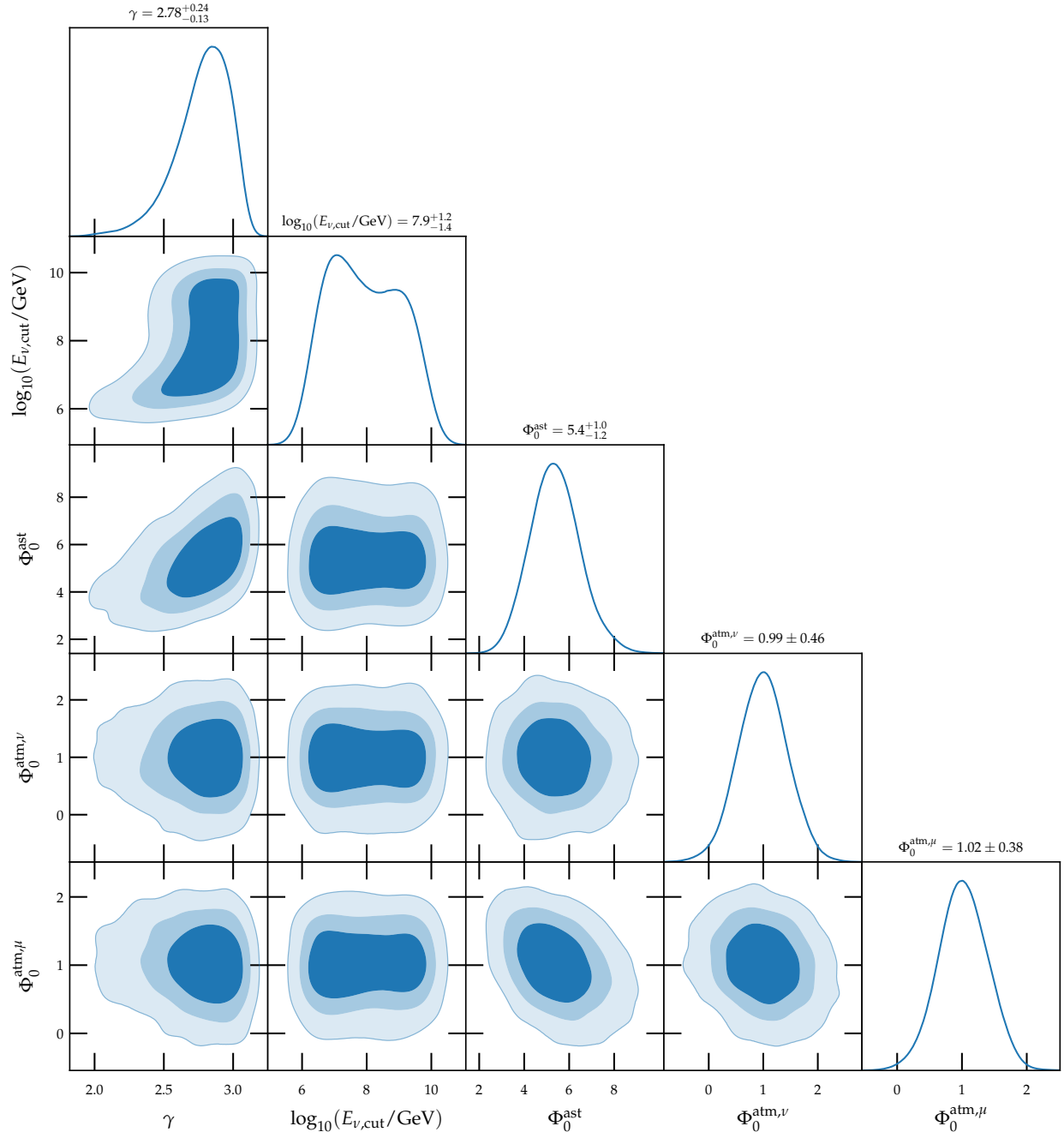


Figure B.2: Posterior probability distributions of Standard Model free-streaming neutrinos. Darkest blue regions are of 68% C.L., medium blue regions are of 95% C.L., and light blue regions are of 99.7% C.L.

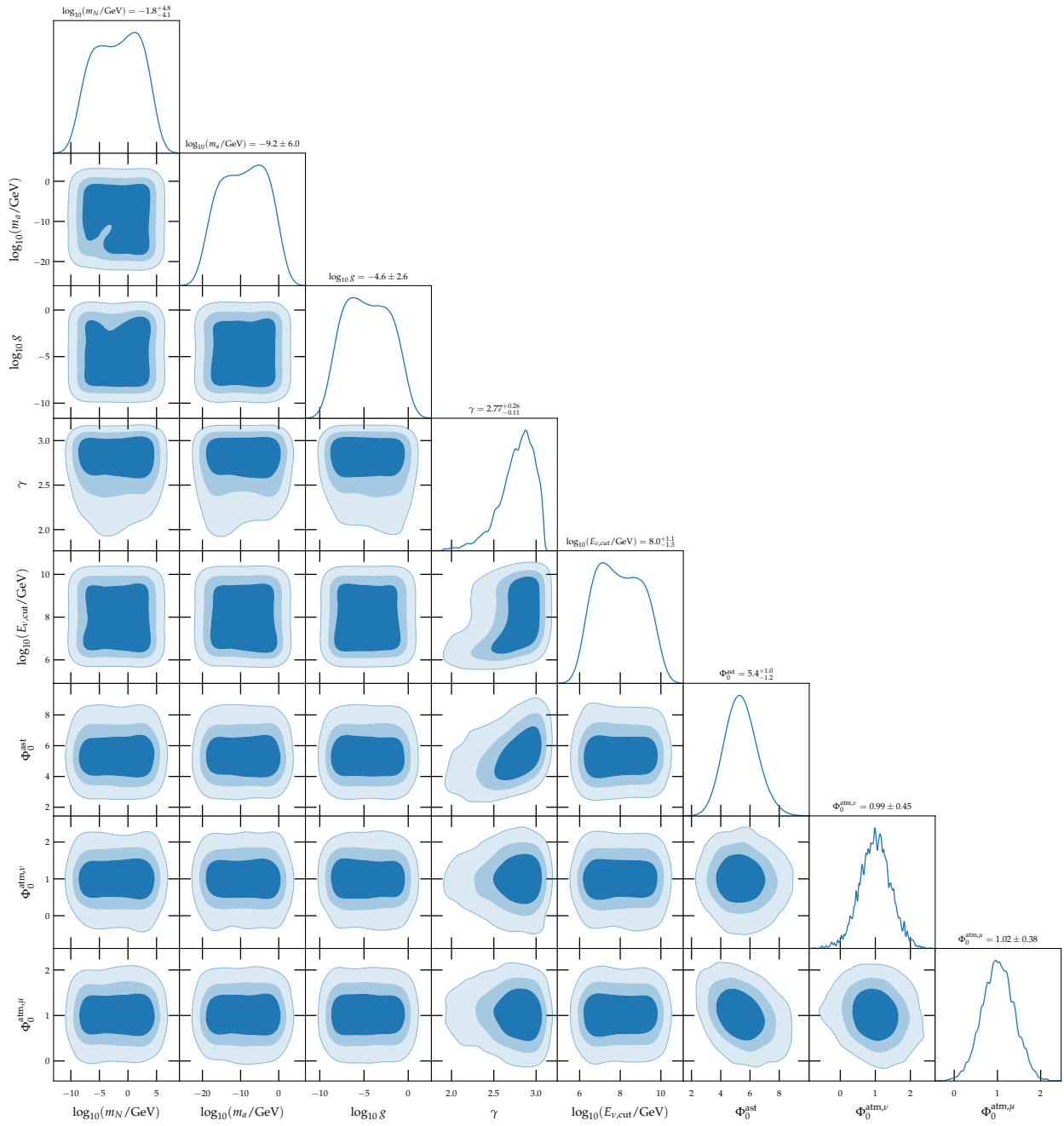


Figure B.3: Posterior probability distributions of neutrinos of beyond the Standard Model physics where axion-neutrino interaction take place. Darkest blue regions are of 68% C.L., medium blue regions are of 95% C.L., and light blue regions are of 99.7% C.L.